Copyright

by

Jonathan Steven Slowik

2015

The Dissertation Committee for Jonathan Steven Slowik Certifies that this is the approved version of the following dissertation:

The Relationships between Muscle Weakness, Wheelchair Propulsion Technique and Upper Extremity Demand

Committee:

Richard R. Neptune, Supervisor

Ronald E. Barr

Ashish D. Deshpande

Sara J. Mulroy

Philip S. Requejo

The Relationships between Muscle Weakness, Wheelchair Propulsion Technique and Upper Extremity Demand

by

Jonathan Steven Slowik, B.S.M.E.; M.S.E.

Dissertation

Presented to the Faculty of the Graduate School of
The University of Texas at Austin
in Partial Fulfillment
of the Requirements
for the Degree of

Doctor of Philosophy

The University of Texas at Austin
August 2015

Dedication

This dissertation is dedicated to my loving wife, Nicole, and our growing family.

Acknowledgements

I would like to thank my advisor, Dr. Richard Neptune, for all of his guidance and support throughout my graduate studies, which have been instrumental to my growth as both a researcher and a person. I feel well-prepared for the next step in my career, thanks to the opportunities, challenges and constructive feedback that he has provided during my time at the University of Texas at Austin. I am also extremely grateful for the rich and collaborative research environment that he has created in the Neuromuscular Biomechanics Laboratory.

This exceptional research environment is also cultivated by the lab members, both past and present. I would like to thank them for their constant encouragement and support. I have developed many great friendships during my time in the lab, and I know that these relationships will last long after I leave Austin.

I am very grateful to Dr. Sara Mulroy and Dr. Philip Requejo for providing their assistance and expertise. My Ph.D. research has been greatly strengthened by their contributions. I would also like to thank the members of their research groups at Rancho Los Amigos National Rehabilitation Center for their hard work collecting the experimental data that made my Ph.D. work possible. I feel extremely fortunate to have been part of this collaboration.

I would also like to thank Dr. Ronald Barr and Dr. Ashish Deshpande for serving on my dissertation committee. The feedback that they have provided throughout this process, from the initial research proposal to final dissertation submission is much appreciated.

Thank you to my parents and sister for being wonderful examples of how to succeed in both an engineering career and family life. My family and close friends have always inspired and motivated me, and I am extremely thankful for these important relationships.

Above all, I would like to thank my amazing wife, Nicole, for her tremendous love and encouragement during both challenging moments and joyous ones. None of this work would have been possible without her enduring support. I am thankful for every second that we have together (and with the rest of our growing family).

Finally, I would also like to acknowledge the following sources of financial support: the National Science Foundation Graduate Research Fellowship Program, the Electrical Engineering Class of 1946 Endowed Graduate Fellowship in Engineering and the Graduate Dean's Prestigious Fellowship Supplement.

The Relationships between Muscle Weakness, Wheelchair Propulsion Technique and Upper Extremity Demand

Jonathan Steven Slowik, Ph.D.
The University of Texas at Austin, 2015

Supervisor: Richard R. Neptune

There are millions of individuals throughout the world that rely on manual wheelchair propulsion as their primary method of mobility. Due to the considerable physical demand of wheelchair propulsion, these individuals are at an increased risk of developing upper extremity pain and injuries that can lead to a progressive decline in independence and quality of life. The overall goal of this research was to use a combination of experimental analyses and forward dynamics simulation techniques to gain an increased understanding of the relationships between muscle weakness, wheelchair propulsion technique and upper extremity demand.

In the first study, a set of simulations was used to investigate the compensatory mechanisms that result from weakness in specific muscle groups. The simulation results suggested that the upper extremity musculature is robust to weakness in individual muscle groups as other muscles were able to compensate and restore normal propulsion mechanics. However, high stress levels and potentially harmful shifts in power generated by the rotator cuff muscles were observed. Such overuse could lead to the development of pain and injury in these muscles, suggesting that rehabilitation programs should target strengthening these muscles.

In the second study, a set of objective quantitative parameters was developed to characterize kinematic hand patterns and assess the influence of propulsion speed and grade of incline on the patterns preferred by a group of 170 experienced manual wheelchair users. Increased propulsion speed resulted in a shift away from under-rim hand patterns while increased grade resulted in the hand remaining near the handrim throughout the propulsion cycle. These results identified how individuals modify their hand patterns in response to different propulsion conditions encountered in daily activities.

In the third study, simulations of four commonly observed hand pattern types were generated. The simulations revealed the double loop and semi-circular patterns had the lowest overall muscle stress and total muscle power, suggesting that these hand patterns may reduce upper extremity demand. Together, the results of these studies have provided a scientific basis for designing rehabilitation and training programs aimed at reducing the prevalence of upper extremity injury and pain among individuals who use manual wheelchairs.

Table of Contents

List of Tables xii

List of Figures xiv

Chapter 1: Introduction 1

Chapter 2: Compensatory Mechanisms during Manual Wheelchair Propulsion in Response to Weakness in Individual Muscle Groups 7

- Introduction 7
- Methods 10
  - Musculoskeletal model 10
  - Simulation and optimization framework 11
  - Experimental data 12
  - Analysis 14
- Results 15
  - Muscle power 18
  - Muscle stress 18
- Discussion 24
  - Muscle power 24
  - Muscle stress 26
  - Clinical implications 27
  - Study limitations 27
- Conclusions 28

Chapter 3: The Influence of Speed and Grade on Wheelchair Propulsion Hand Pattern 30

- Introduction 30
- Methods 32
  - Subjects 32
  - Data collection 32
  - Data processing 33
  - Pattern characterization 33

        Statistical analyses 36
    Results 36
    Discussion 40
    Conclusions 45

Chapter 4: The Influence of Wheelchair Propulsion Hand Pattern on Upper Extremity Demand 46
    Introduction 46
    Methods 48
        Musculoskeletal model 48
        Simulation and optimization framework 49
        Experimental data 50
        Analysis 51
    Results 54
        Experimental data tracking 54
        Overall muscle power 54
        Individual muscle power 56
        Overall muscle stress 59
        Individual muscle stress 60
    Discussion 62
        Propulsion characteristics 63
        AR 63
        SL 64
        DL 64
        SC 65
        Study limitations 65
    Conclusions 66

Chapter 5: Conclusions 67

Chapter 6: Future Work 70

Appendix A: Supplementary Material for Chapter 2 73

Appendix B: Supplementary Material for Chapter 3 86

Appendix C: Supplementary Material for Chapter 4 88

References 92

Vita 99

List of Tables

Table 2.1: Upper extremity muscle and group definitions. 13

Table 2.2: Individual and group-averaged subject and propulsion characteristics. 14

Table 2.3: Root-mean-square differences between the simulated mechanics and group-averaged experimental mechanics. For comparison, one standard deviation (SD) of the experimental data is provided to indicate the inter-subject variability. 17

Table 2.4: Total muscle power shifts between muscle groups. Color gradient from red (increase) to green (decrease) represents the change in total muscle power. (For interpretation of the references to color, the reader is referred to the web version of this article). Italics denote a shift greater than 1.50 W. 19

Table 2.5: Muscle group power compensations. Key compensations were defined to be those that accounted for at least ten percent of the total magnitude of power shifts that resulted from a muscle group being weakened. 20

Table 2.6: Average stress values over the full cycle for the individual muscle groups. Columns correspond to the different simulations (i.e., the weakened muscle groups). Color gradient from light (low) to dark (high) represents the average stress levels. 22

Table 2.7: Maximum stress values over the full cycle for the individual muscle groups. Columns correspond to the different simulations (i.e., the weakened muscle groups). Color gradient from light (low) to dark (high) represents the maximum stress levels. 23

Table 3.1: Mean (SD) values of the propulsion variables for each condition....38

Table 3.2: Number of wheelchair users (percentage) using each hand pattern type across conditions using the objective classification method............40

Table 4.1: Mean values of subject and propulsion characteristics for the four hand pattern types: arcing (AR), single loop (SL), double loop (DL) and semi-circular (SC)..51

Table 4.2: Upper extremity muscle and group definitions................................53

Table 4.3: Root-mean-square differences between simulated and experimental joint kinematics and handrim forces for the four hand pattern types: arcing (AR), single loop (SL), double loop (DL) and semi-circular (SC). For comparison, one standard deviation of the experimental data is provided in parentheses to indicate inter-subject variability...........................54

List of Figures

Figure 1.1: Hand pattern definitions. The four common hand pattern types are arcing (AR), single loop (SL), double loop (DL) and semi-circular (SC). The solid line denotes the contact phase, while the dashed line denotes the recovery phase. The arrows indicate the direction of hand motion and the direction of propulsion is to the right. 4

Figure 2.1: Comparison between the baseline simulation and group-averaged experimental mechanics. Experimental and simulation values are represented by solid and dashed lines, respectively. Shaded regions represent ± 1 SD of the experimental data. The joint angle plots depict the full cycle, with the end of the contact phase indicated with a vertical line. The handrim force plots only depict the contact phase, as values are approximately zero throughout the recovery phase. 16

Figure 2.2: Baseline simulation average and maximum stress values over the full cycle for the individual muscles. The thick black boxes correspond to the average value for the muscle group. 21

Figure 2.3: Moment (M) created by the forces generated by supraspinatus (SUPSP) and anterior deltoid (DELT1). While both muscles can produce an abduction moment, the supraspinatus force draws the humeral head towards the glenoid fossa while the anterior deltoid provides a more superiorly directed force. 25

Figure 3.1: Hand pattern and variable definitions. The four hand pattern types are arcing (AR), single loop (SL), double loop (DL) and semi-circular (SC). The solid line denotes the contact phase, while the dashed line denotes the recovery phase. Also depicted is the radius of the handrim (r) and angle of handrim contact (θ). The mathematical signs denote whether the signed area enclosed by each loop is positive (+) or negative (-). 34

Figure 3.2: Comparison of objective and subjective hand pattern classification results. The vertical axis corresponds to TRT and the horizontal axis corresponds to the ratio NRT/TRT. Thresholds for the objective classification are depicted with the dashed lines at TRT = 0.03m, NRT/TRT = -0.95 and NRT/TRT = 0.95. Regions corresponding to each pattern type are labeled with the objective classification. Subjective classification is indicated with the following symbols: AR (◆), DL (×), SC (●) and SL (■). For figure clarity, NRT/TRT was selected as the horizontal axis variable instead of NRT. 37

Figure 3.3: Hand pattern parameter values across conditions. The vertical axis corresponds to TRT and the horizontal axis corresponds to NRT. Thresholds for the objective classification are depicted with the dashed lines at TRT = 0.03m, NRT/TRT = -0.95 and NRT/TRT = 0.95. Regions corresponding with each pattern type are labeled with the objective classification. Propulsion condition is indicated as follows: free (○), fast (□) and graded (△). The across-subject mean values are indicated with a larger version of the same symbols. For comparisons across conditions, NRT was selected as the horizontal axis variable instead of NRT/TRT. 39

Figure 4.1: Hand pattern definitions. The four hand pattern types are arcing (AR), single loop (SL), double loop (DL) and semi-circular (SC). The solid line denotes the contact phase, while the dashed line denotes the recovery phase. The arrows indicate the direction of hand motion and the direction of wheelchair propulsion is to the right. 46

Figure 4.2: Overall levels of time-averaged negative, positive, total and net power (summed across all muscles) for the four hand pattern types: arcing (AR), single loop (SL), double loop (DL) and semi-circular (SC). The top, middle and bottom rows correspond to the contact phase, recovery phase and full cycle respectively. Contact and recovery-phase contributions are colored blue and orange respectively...................56

Figure 4.3: Time-averaged positive and negative power generated by each muscle group for the four hand pattern types: arcing (AR), single loop (SL), double loop (DL) and semi-circular (SC). The left, center and right plots correspond to the contact phase, recovery phase and full cycle respectively. Contact and recovery-phase contributions are colored blue and orange respectively...58

Figure 4.4: Overall levels of time-averaged muscle stress (averaged across all muscles) for the four hand pattern types: arcing (AR), single loop (SL), double loop (DL) and semi-circular (SC). The top, middle and bottom rows correspond to the contact phase, recovery phase and full cycle respectively. Contact and recovery-phase contributions are colored blue and orange respectively...60

Figure 4.5: Time-averaged individual muscle stress values for the four hand pattern types: arcing (AR), single loop (SL), double loop (DL) and semi-circular (SC). The left, center and right plots correspond to the contact phase, recovery phase and full cycle respectively. Contact and recovery-phase contributions are colored blue and orange respectively....................62

Figure A.1: Comparison between the ADelt-weakened simulation and group-averaged experimental mechanics. Experimental and simulation values are represented by solid and dashed lines, respectively. Shaded regions represent ± 1 SD of the experimental data. The joint angle plots depict the full cycle, with the end of the contact phase indicated with a vertical line. The handrim force plots only depict the contact phase, as values are approximately zero throughout the recovery phase. 73

Figure A.2: Comparison between the MDelt-weakened simulation and group-averaged experimental mechanics. Experimental and simulation values are represented by solid and dashed lines, respectively. Shaded regions represent ± 1 SD of the experimental data. The joint angle plots depict the full cycle, with the end of the contact phase indicated with a vertical line. The handrim force plots only depict the contact phase, as values are approximately zero throughout the recovery phase. 74

Figure A.3: Comparison between the Subsc-weakened simulation and group-averaged experimental mechanics. Experimental and simulation values are represented by solid and dashed lines, respectively. Shaded regions represent ± 1 SD of the experimental data. The joint angle plots depict the full cycle, with the end of the contact phase indicated with a vertical line. The handrim force plots only depict the contact phase, as values are approximately zero throughout the recovery phase. 75

Figure A.4: Comparison between the Supra-weakened simulation and group-averaged experimental mechanics. Experimental and simulation values are represented by solid and dashed lines, respectively. Shaded regions represent ± 1 SD of the experimental data. The joint angle plots depict the full cycle, with the end of the contact phase indicated with a vertical line. The handrim force plots only depict the contact phase, as values are approximately zero throughout the recovery phase. 76

Figure A.5: Comparison between the Infra-weakened simulation and group-averaged experimental mechanics. Experimental and simulation values are represented by solid and dashed lines, respectively. Shaded regions represent ± 1 SD of the experimental data. The joint angle plots depict the full cycle, with the end of the contact phase indicated with a vertical line. The handrim force plots only depict the contact phase, as values are approximately zero throughout the recovery phase. 77

Figure A.6: Comparison between the PecMaj-weakened simulation and group-averaged experimental mechanics. Experimental and simulation values are represented by solid and dashed lines, respectively. Shaded regions represent ± 1 SD of the experimental data. The joint angle plots depict the full cycle, with the end of the contact phase indicated with a vertical line. The handrim force plots only depict the contact phase, as values are approximately zero throughout the recovery phase. 78

Figure A.7: Comparison between the Lat-weakened simulation and group-averaged experimental mechanics. Experimental and simulation values are represented by solid and dashed lines, respectively. Shaded regions represent ± 1 SD of the experimental data. The joint angle plots depict the full cycle, with the end of the contact phase indicated with a vertical line. The handrim force plots only depict the contact phase, as values are approximately zero throughout the recovery phase. 79

Figure A.8: Comparison between the Tri-weakened simulation and group-averaged experimental mechanics. Experimental and simulation values are represented by solid and dashed lines, respectively. Shaded regions represent ± 1 SD of the experimental data. The joint angle plots depict the full cycle, with the end of the contact phase indicated with a vertical line. The handrim force plots only depict the contact phase, as values are approximately zero throughout the recovery phase. 80

Figure A.9: Comparison between the Bra-weakened simulation and group-averaged experimental mechanics. Experimental and simulation values are represented by solid and dashed lines, respectively. Shaded regions represent ± 1 SD of the experimental data. The joint angle plots depict the full cycle, with the end of the contact phase indicated with a vertical line. The handrim force plots only depict the contact phase, as values are approximately zero throughout the recovery phase. 81

Figure A.10: Comparison between the Bic-weakened simulation and group-averaged experimental mechanics. Experimental and simulation values are represented by solid and dashed lines, respectively. Shaded regions represent ± 1 SD of the experimental data. The joint angle plots depict the full cycle, with the end of the contact phase indicated with a vertical line. The handrim force plots only depict the contact phase, as values are approximately zero throughout the recovery phase. 82

Figure A.11: Comparison between the Sup-weakened simulation and group-averaged experimental mechanics. Experimental and simulation values are represented by solid and dashed lines, respectively. Shaded regions represent ± 1 SD of the experimental data. The joint angle plots depict the full cycle, with the end of the contact phase indicated with a vertical line. The handrim force plots only depict the contact phase, as values are approximately zero throughout the recovery phase. 83

Figure A.12: Comparison between the Pro-weakened simulation and group-averaged experimental mechanics. Experimental and simulation values are represented by solid and dashed lines, respectively. Shaded regions represent ± 1 SD of the experimental data. The joint angle plots depict the full cycle, with the end of the contact phase indicated with a vertical line. The handrim force plots only depict the contact phase, as values are approximately zero throughout the recovery phase. 84

Figure A.13: Comparison between muscle excitation timing data from the baseline simulation and values found in the literature (Dubowsky et al., 2009; Mulroy et al., 2004; Mulroy et al., 1996; Qi et al., 2013; Rodgers et al., 1994). 85

Figure B.1: Comparison of objective and subjective hand pattern classification results. The vertical axis corresponds to TRT and the horizontal axis corresponds to the ratio NRT. Thresholds for the objective classification are depicted with the dashed lines at TRT = 0.03m, NRT/TRT = -0.95 and NRT/TRT = 0.95. Regions corresponding to each pattern type are labeled with the objective classification. Subjective classification is indicated with the following symbols: AR (◆), DL (×), SC (●) and SL (■)..86

Figure B.2: Hand pattern parameter values across conditions. The vertical axis corresponds to TRT and the horizontal axis corresponds to NRT/NRT. Thresholds for the objective classification are depicted with the dashed lines at TRT = 0.03m, NRT/TRT = -0.95 and NRT/TRT = 0.95. Regions corresponding with each pattern type are labeled with the objective classification. Propulsion condition is indicated as follows: free (○), fast (□) and graded (△). The across-subject mean values are indicated with a larger version of the same symbol. 87

Figure C.1: Comparison between the simulation and group-averaged experimental mechanics for the arcing pattern (AR). Experimental and simulation values are represented by solid and dashed lines, respectively. Shaded regions represent ± 1 SD of the experimental data. The joint angle plots depict the full cycle, with the end of the contact phase indicated with a vertical line. The handrim force plots only depict the contact phase, as values are approximately zero throughout the recovery phase.........88

Figure C.2: Comparison between the simulation and group-averaged experimental mechanics for the single loop pattern (SL). Experimental and simulation values are represented by solid and dashed lines, respectively. Shaded regions represent ± 1 SD of the experimental data. The joint angle plots depict the full cycle, with the end of the contact phase indicated with a vertical line. The handrim force plots only depict the contact phase, as values are approximately zero throughout the recovery phase.........89

Figure C.3: Comparison between the simulation and group-averaged experimental mechanics for the double loop pattern (DL). Experimental and simulation values are represented by solid and dashed lines, respectively. Shaded regions represent ± 1 SD of the experimental data. The joint angle plots depict the full cycle, with the end of the contact phase indicated with a vertical line. The handrim force plots only depict the contact phase, as values are approximately zero throughout the recovery phase. 90

Figure C.4: Comparison between the simulation and group-averaged experimental mechanics for the semi-circular pattern (SC). Experimental and simulation values are represented by solid and dashed lines, respectively. Shaded regions represent ± 1 SD of the experimental data. The joint angle plots depict the full cycle, with the end of the contact phase indicated with a vertical line. The handrim force plots only depict the contact phase, as values are approximately zero throughout the recovery phase. 91

Chapter 1: Introduction

In 2010, there were approximately 3.7 million individuals using wheelchairs in the United States (Brault, 2012). This number represents a 66% increase since 1997 (Brault, 2008; Brault, 2012; McNeil, 2001; Steinmetz, 2006), and this rapid growth is expected to continue (e.g., Cooper et al., 2008). A large majority (~90%) of these individuals rely on manual wheelchair propulsion as their primary method of mobility (Kaye et al., 2000). While advancements in medical care and emerging assistive technologies have greatly improved life expectancy, activity levels and community involvement of these individuals (e.g., Cooper et al., 2008), the considerable physical demand placed on the upper extremity during manual wheelchair use can lead to upper extremity pain and injury (e.g., Requejo et al., 2008).

It is estimated that over half of all manual wheelchair users will experience upper extremity pain and injury (e.g., PVACSCM, 2005), which can be highly debilitating and lead to a decrease in independence and quality of life (e.g., Gutierrez et al., 2007). The high prevalence of upper extremity pain and injury among this population is likely influenced by the high physical demands of manual wheelchair propulsion (e.g., Requejo et al., 2008), as significant intermuscular coordination is required to generate the mechanical power necessary to propel the wheelchair while maintaining joint stability (e.g., Rankin et al., 2012; Rankin et al., 2011; van der Helm and Veeger, 1996).

While the exact relationship between the physical demands of wheelchair propulsion and upper extremity demand is not yet fully understood, ergonomics studies consistently suggest that there is a link between highly repetitive tasks and the occurrence of upper extremity pain and injury (e.g., Boninger et al., 2005). Many of these studies specifically discourage tasks with high frequency and force requirements. Manual wheelchair propulsion typically involves cadences and handrim forces (e.g., Boninger et al., 2002) that far exceed suggested thresholds in the ergonomics literature (e.g., Silverstein et al., 1987). As risk indicators for upper extremity pain and injury, large-scale variables such as cadence and peak handrim force are commonly used as indirect measures of upper extremity demand (e.g., Boninger et al., 2002; Kwarciak et al., 2012). The widespread use of these variables is also likely due to the difficulty in obtaining more direct measures such as muscle and joint forces (e.g., Erdemir et al., 2007). Even when inverse dynamics modeling techniques have been used, the redundancy of the upper extremity musculature and the absence of the nonlinear muscle dynamics in the model make it difficult to ascertain individual muscle forces (Zajac et al., 2002). In addition, while the use of electromyographic data does provide insight into the timing of individual muscle activity (e.g., Mulroy et al., 1996), the complex nonlinear relationships between muscle excitation signals and individual muscle forces complicates analyses and limits the conclusions that can be drawn from such studies.

In contrast, forward dynamics modeling and simulation techniques can provide a powerful framework for examining the biomechanics of a task at the individual muscle level (Erdemir et al., 2007). These techniques have previously been used to analyze a wide range of human movement tasks such as gait (e.g., Hamner et al., 2010; Liu et al., 2006; Sasaki and Neptune, 2006) and pedaling (e.g., Hakansson and Hull, 2007; Neptune et al., 2000). In addition, recent studies have demonstrated how the application of these techniques can add to the current understanding of the biomechanics of manual wheelchair propulsion. One such study identified individual muscle contributions to manual wheelchair propulsion (Rankin et al., 2011), while others have used simulation to identify how adjusting seat position (Slowik and Neptune, 2013), direction of handrim force application (Rankin et al., 2010) and propulsion technique (i.e., cadence, peak force and contact angle; Rankin et al., 2012) can influence direct measures of upper extremity demand (e.g., muscle stresses and powers).

Simulation techniques could therefore be very useful in identifying the influence of individual muscle weakness on upper extremity demand. The relative levels of individual muscle strengths (i.e., force-generating capacities) can be affected by a variety of factors, including injury level (e.g., van Drongelen et al., 2006) and fatigue (e.g., Kumar, 2001). Due to the redundancy of the upper extremity musculature, different combinations of muscle forces can produce identical propulsion mechanics (i.e., joint kinematics and handrim forces), and muscle strength differences likely influence which combination is selected (e.g., Erdemir et al., 2007). Some combinations of muscle forces may place the upper extremity at a greater risk of developing pain and injury (e.g., van Drongelen et al., 2013), so it is critical to understand how weakness in specific muscle groups can lead to shifts in individual muscle contributions to upper extremity demand. Therefore, the goal of the study in Chapter 2 was to use musculoskeletal modeling and forward dynamics simulations of wheelchair propulsion to identify the compensatory strategies necessary to overcome weakness in specific muscle groups and restore propulsion mechanics. Such an analysis would illustrate shifts in upper extremity demand that may occur during manual wheelchair propulsion without measureable differences in technique and provide a foundation for the design of targeted muscle strengthening programs.

While manual wheelchair users can overcome impairments by using different combinations of muscle forces to produce similar propulsion mechanics, individuals may also alter their propulsion technique. Studies have shown that manual wheelchair users can use a number of different propulsion techniques to accomplish the same task because propulsion mechanics are largely unconstrained (e.g., Vegter et al., 2014). Although manual wheelchair propulsion requires application of a propulsive force to the handrim during the contact phase, individuals can choose a variety of kinematic paths along which to return the hand during the recovery phase (e.g., de Groot et al., 2004). Thus, propulsion technique can be characterized by the kinematic hand pattern (i.e., full-cycle hand path), which is commonly assigned to one of four distinct pattern types (Fig. 1.1): arcing (AR), single loop (SL), double loop (DL) and semi-circular (SC) (e.g., Boninger et al., 2002).

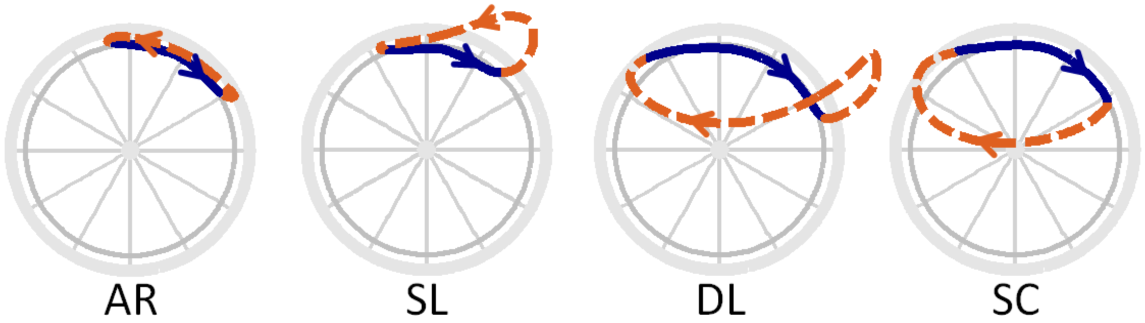

Figure 1.1: Hand pattern definitions. The four common hand pattern types are arcing (AR), single loop (SL), double loop (DL) and semi-circular (SC). The solid line denotes the contact phase, while the dashed line denotes the recovery phase. The arrows indicate the direction of hand motion and the direction of propulsion is to the right.

Previous studies have primarily used subjective and qualitative methods to classify hand patterns, which has led to inconsistencies between studies when hybrid patterns are encountered (i.e., patterns with features similar to multiple hand pattern types) (e.g., Koontz et al., 2009). In addition, this broad categorization ignores all differences between patterns of the same type. Thus, hand pattern characterization could be improved by addressing these limitations.

Although individuals typically develop a preferred hand pattern for level propulsion at their self-selected speed, they may modify their propulsion technique in response to changes in task demands, such as speed (Boninger et al., 2002) or grade of incline (Richter et al., 2007). As manual wheelchair users frequently encounter different propulsion conditions during activities of daily living, it is important to understand the influence of these conditions on propulsion technique. Therefore, the goal of the study in Chapter 3 was to develop a set of objective, quantitative parameters to characterize hand patterns and determine the influence of propulsion condition (i.e., speed and grade of incline) on the hand patterns preferred by manual wheelchair users.

While the study in Chapter 3 identified the influence of speed and grade on preferred hand patterns, the next step was to assess whether there are any potential biomechanical advantages or disadvantages of one pattern type over the others. Current clinical guidelines recommend the use of the SC pattern (PVACSCM, 2005), citing advantageous levels of large-scale biomechanical variables (e.g., low cadence and low peak forces). However, it would be beneficial to understand how the different hand patterns influence direct measures of upper extremity demand (e.g., required muscle power and muscle stress). A detailed understanding of these differences could help identify potential injury risks and reduce the development of pain by providing a foundation for clinical recommendations and propulsion training programs. Therefore, the goal of the study in Chapter 4 was to use musculoskeletal modeling and forward dynamics simulations to investigate the influence of wheelchair propulsion hand pattern on upper extremity demand.

The overall goal of these studies was to combine experimental analyses with modeling and simulation techniques to gain an increased understanding of the relationships between muscle weakness, wheelchair propulsion technique and upper extremity demand. Understanding these relationships has implications for the design of rehabilitation and propulsion training programs aimed at minimizing the development of pain and injury in manual wheelchair users.

Chapter 2: Compensatory Mechanisms during Manual Wheelchair Propulsion in Response to Weakness in Individual Muscle Groups

INTRODUCTION

Over half of all manual wheelchair users will develop upper extremity pain and injury at some point in their lifetime (e.g., Finley and Rodgers, 2004), which can be highly debilitating and lead to a decrease in independence and quality of life (e.g., Gutierrez et al., 2007). This high incidence of pain and injury is correlated with the considerable physical demand placed on the upper extremity during wheelchair propulsion (e.g., Curtis et al., 1999), as significant intermuscular coordination is needed to generate the mechanical power necessary to propel the wheelchair while maintaining joint stability (e.g., Rankin et al., 2012; Rankin et al., 2011; van der Helm and Veeger, 1996).

Due to the mechanical redundancy of the musculoskeletal system, many different combinations of muscle forces can produce the same net joint moments and generate the required mechanical power (e.g., Pandy and Andriacchi, 2010). Although there is some uncertainty in how the neuromuscular system resolves muscle redundancy to perform a given movement task, most theories suggest that the relative levels of force-generating capacity in individual muscles influence the selection (Erdemir et al., 2007). Muscle weakness (or decrease in the capacity to generate force) can be influenced by a number of factors including fatigue and neurological deficits (Requejo et al., 2008).

Muscle fatigue can result from a number of mechanisms, but it is generally quantified as a transient reduction in the force capacity of a muscle due to sustained physical activity (Enoka and Duchateau, 2008). In order to fulfill specific task requirements, fatigue may occur at different rates in individual muscles and resulting fatigue-related changes in musculoskeletal loading may lead to injury (Kumar, 2001). However, the overall effect of fatigue on wheelchair propulsion biomechanics is not well understood, as one study concluded that fatigue may lead to potentially harmful changes in propulsion mechanics (Rodgers et al., 1994) while others have suggested that during an extended period of propulsion, individuals may actually make beneficial adjustments to their propulsion mechanics to mitigate the increased risk of injury (Rice et al., 2009). Inverse dynamics-based analyses have found that during manual wheelchair propulsion, the highest net joint moments and powers are generated at the shoulder, suggesting that the shoulder joint may be the most at risk for overuse injury (e.g., Rodgers et al., 1994; Veeger et al., 1991). These analyses also identified small fatigue-related shifts in joint power from the shoulder to more distal joints (Rodgers et al., 2003). Recently, a study found that electromyography intensity increases with fatigue and suggested that fatigue could contribute to imbalances between the propulsive and recovery phase muscles (Qi et al., 2012). However, the effect of fatigue in individual muscles on propulsion mechanics has remained relatively unexplored.

Muscle weakness can also result from neurological deficiencies due to injury or disease and ensuing neuromuscular changes, such as denervation and atrophy (e.g., Thomas and Zijdewind, 2006). Furthermore, the breadth and magnitude of these reductions can vary based on the specific impairment or injury level. For example, a person with paraplegia will likely be able to produce larger forces with their triceps and pectoralis major muscles than a person with tetraplegia (e.g., van Drongelen et al., 2006). However, despite these differences, shoulder joint kinematic patterns and net joint moments during wheelchair propulsion have been shown to be remarkably similar across different spinal cord injury levels (Kulig et al., 2001; Newsam et al., 1999).

Although muscle redundancy may minimize the effect of individual muscle weakness on propulsion mechanics, it is important to understand the potential compensatory mechanisms used by the neuromuscular system, as the resulting combinations of muscle forces may put the upper extremity at a higher risk for the development of pain and injury. The potential for injury has been illustrated in previous studies showing that larger forces from the deltoid relative to the humeral head depressors (i.e., rotators and adductors) may lead to subacromial impingement (e.g., Burnham et al., 1993; Sharkey and Marder, 1995) and that other unbalanced combinations of forces can lead to dislocation (Labriola et al., 2005).

To gain an increased understanding of intermuscular coordination during wheelchair propulsion, forward dynamics simulations have been shown to be an effective tool (e.g., Zajac et al., 2002). Potential compensatory strategies in response to individual muscle weakness can be revealed through analyzing the resulting shifts in individual muscle activation or power generation. A similar approach has previously been used to determine the effect of muscle weakness during steady-state walking (Goldberg and Neptune, 2007; Jonkers et al., 2003; van der Krogt et al., 2012). Forward dynamics simulations can also be used to examine specific measures of upper extremity demand, such as muscle stress, to help identify muscles that may be placed at risk for overuse injuries (Rankin et al., 2012).

Therefore, the purpose of this study was to use musculoskeletal modeling and forward dynamics simulations of wheelchair propulsion to identify the compensatory strategies necessary to overcome weakness in individual muscle groups and highlight those strategies that could lead to the development of upper extremity pain and injury. The results of this study can provide rationale for the design of targeted rehabilitation programs aimed at minimizing the development of pain and injury in manual wheelchair users.

METHODS

Musculoskeletal model

The upper extremity musculoskeletal model and dynamic optimization framework used in this study to generate the simulations of manual wheelchair propulsion have been previously described in detail (Rankin et al., 2010; Rankin et al., 2011). The musculoskeletal model was developed using SIMM (Musculographics, Inc., Santa Rosa, CA, USA) based on the work of Holzbaur et al. (2005) and consisted of segments representing the trunk and right upper arm, forearm and hand. There were six rotational degrees-of-freedom representing trunk lean, shoulder plane-of-elevation, shoulder elevation angle, shoulder internal-external rotation, elbow flexion-extension and forearm pronation-supination. Shoulder angles were thoracohumeral angles, while scapulohumeral rhythm was defined using regression equations based on cadaver data (de Groot and Brand, 2001). Full-cycle trunk lean and contact phase hand translations were prescribed based on experimentally measured kinematic data. The dynamic equations-of-motion were generated using SD/FAST (Parametric Technology Corp., Needham, MA, USA). Twenty-six Hill-type musculoskeletal actuators, governed by intrinsic muscle force-length-velocity and tendon force-strain relationships, represented the major upper extremity muscles crossing the shoulder and elbow joints (e.g., Slowik and Neptune, 2013). Each actuator received a distinct excitation signal except the two sternocostal pectoralis major actuators, the three latissimus dorsi actuators, and the two actuators representing the lateral triceps and anconeus. Within each of these groups, the actuators received the same excitation signal. Muscle excitation-activation dynamics were modeled using a first order differential equation (Raasch et al., 1997) with muscle-specific activation and deactivation time constants (Happee and van der Helm, 1995; Winters and Stark, 1988). The musculotendon lengths and moment arms were determined using polynomial regression equations (Rankin and Neptune, 2012) and the product of the appropriate muscle moment arm and force determined the muscle moment that was applied to each joint. In addition, passive torques were applied at the joints to represent ligaments and other passive joint structures that limit extreme joint positions (Davy and Audu, 1987).

Simulation and optimization framework

Each muscle excitation pattern was generated using a bimodal pattern defined by six parameters (Hall et al., 2011), resulting in a total of 132 optimization parameters. A simulated annealing optimization algorithm (Goffe et al., 1994) was used to identify the excitation parameters that produced a simulation that best emulated the group-averaged experimental propulsion data (i.e., joint angle and 3D handrim force profiles; see *Experimental data* below) using an optimal tracking cost function (Neptune et al., 2001). An additional term was included in the cost function that minimized the square of muscle stress to prevent excess co-contraction.

Based on a combination of anatomical location and muscle function, the musculotendon actuators were assigned to 12 muscle groups for analysis (Table 2.1). An initial simulation was generated using a set of baseline isometric muscle force values derived from anatomical studies (Holzbaur et al., 2005; Table 2.1). These values were then systematically reduced by 50% one group at a time with the remaining groups left unaltered. The excitation pattern of the weakened group was constrained to remain at the baseline values so that it could not compensate for itself, and the muscle excitation patterns of the remaining groups were re-optimized in order to restore the propulsion mechanics that emulated the experimental propulsion data, resulting in an additional 12 simulations.

Experimental data

To provide tracking data for the dynamic optimization, experimental data from twelve experienced male manual wheelchair users with complete motor paraplegia and free of shoulder pain (Table 2.2) were used. The subjects were recruited from outpatient clinics throughout the Rancho Los Amigos National Rehabilitation Center (RLANRC). The participants provided informed written consent in accordance with the Institutional Review Board at RLANRC. Participants propelled their own wheelchair at a self-selected speed on a stationary ergometer with the resistance level set similar to overground propulsion (e.g., Raina et al., 2012). Subjects were allowed to acclimate until they felt comfortable, and a ten-second trial (preceded by at least 30 seconds of propulsion to ensure near steady-state propulsion) was recorded. Trunk, right side upper extremity and wheel kinematics were collected using a 4-scanner CODA motion analysis system (Charnwood Dynamics Ltd., Leicestershire, UK) with 15 markers placed on landmarks on the body and right wheel (e.g., Lighthall-Haubert et al., 2009). Three-dimensional handrim kinetics were measured using an instrumented wheel (SmartWheel; Three Rivers Holdings, Mesa, AZ, USA).

Table 2.1: Upper extremity muscle and group definitions.

Muscle Group	Muscle	Compartment	Abbreviation	Maximum Isometric Force (N)
ADelt	Deltoid	Anterior	DELT1	1142.6
MDelt		Middle	DELT2	1142.6
		Posterior	DELT3	259.9
Subsc	Subscapularis	----------------------	SUBSC	1377.8
Supra	Supraspinatus	----------------------	SUPSP	487.8
Infra	Infraspinatus	----------------------	INFSP	1210.8
	Teres Minor	----------------------	TMIN	354.3
PecMaj	Pectoralis major	Clavicular head	PECM1	364.4
		Sternocostal head - sternum	PECM2	515.4
		Sternocostal head - ribs	PECM3	390.6
	Coracobrachialis	----------------------	CORB	242.5
Lat	Latissimus dorsi	Thoracic	LAT1	389.1
		Lumbar	LAT2	389.1
		Iliac	LAT3	281.7
	Teres Major	----------------------	TMAJ	425.4
Tri	Triceps brachii	Long head	TRIlong	798.5
		Medial head	TRImed	624.3
		Lateral head	TRIlat	624.3
	Anconeus	----------------------	ANC	350.0
Bra	Brachialis	----------------------	BRA	987.3
	Brachioradialis	----------------------	BRD	261.3
Bic	Biceps brachii	Long head	BIClong	624.3
		Short head	BICshort	435.6
Sup	Supinator	----------------------	SUP	476.0
Pro	Pronator teres	----------------------	PT	566.2
	Pronator quadratus	----------------------	PQ	75.5

Table 2.2: Individual and group-averaged subject and propulsion characteristics.

Subject characteristics					**Propulsion characteristics**		
Subject	Age (yr)	Time from injury (yr)	Height (m)	Mass (kg)	Full-cycle time (s)	Contact phase time (s)	Propulsion speed (m/s)
1	26.7	4.6	1.68	69.7	0.79	0.28	1.95
2	29.6	9.7	1.75	95.3	1.20	0.48	1.10
3	43.0	16.4	1.75	53.5	0.91	0.35	1.21
4	39.6	15.5	1.70	86.0	0.96	0.36	1.45
5	21.9	6.6	1.83	68.0	1.21	0.33	1.69
6	43.5	16.8	1.73	62.5	1.08	0.36	1.14
7	25.7	2.4	1.73	74.9	1.29	0.37	1.85
8	28.5	6.0	1.73	97.7	1.15	0.38	1.22
9	30.3	15.8	1.68	61.4	1.30	0.48	1.08
10	20.6	2.8	1.85	91.2	1.02	0.35	1.32
11	37.5	15.5	1.70	74.0	1.10	0.44	0.99
12	32.1	16.9	1.73	88.4	1.18	0.41	0.85
Average	**31.6**	**10.7**	**1.74**	**76.9**	**1.10**	**0.38**	**1.32**

Kinematic and kinetic data were low-pass filtered with a fourth-order zero-lag Butterworth filter with cutoff frequencies of 4 Hz and 8 Hz, respectively, using Visual3D (C-Motion, Inc., Germantown, MD, USA). A resultant handrim force threshold of 5N was used to delineate between contact and recovery phases. Contact and recovery phase data for each cycle were time-normalized and averaged across propulsion cycles within each subject. Mean subject data were then averaged across subjects to create group-averaged joint angle and 3D handrim force profiles.

Analysis

Two consecutive propulsion cycles were simulated and the second cycle was analyzed to allow the simulations to reach steady-state. Average differences from experimental data were calculated to assess how well each simulation tracked the experimental data. Individual muscle data were analyzed over the full propulsion cycle (contact and recovery). To quantify muscle contributions to propulsion, instantaneous mechanical power was calculated for each muscle at each time step and summed within each muscle group. Mean positive (negative) power generation was calculated by averaging the instantaneous positive (negative) power across time steps, and then total (i.e., absolute value sum) mean power was calculated for each muscle group. Muscle stress was calculated as the instantaneous muscle force at each time step divided by the physiological cross-sectional area and then normalized by the maximum possible isometric stress. This measure of normalized muscle stress is also equivalent to the ratio of the muscle force to the maximum isometric muscle force. Peak and average stress values over the full propulsion cycle were calculated to identify muscle groups that may be at risk for overuse injuries.

RESULTS

All 13 simulations resulted in propulsion mechanics that closely emulated the group-averaged experimental joint kinematics and handrim forces (e.g., Fig. 2.1), with average differences of 0.8° and 1.0 N, respectively (Table 2.3). All root-mean-square (RMS) differences between the simulated and group-averaged experimental mechanics were well within one standard deviation (SD) of the experimental data. The maximum SD-normalized RMS difference (0.37) corresponded to forearm pronation/supination when the pronator group (Table 2.3: Pro) was weakened. Additional figures comparing the simulation and experimental data can be found in the supplementary material in Appendix A.

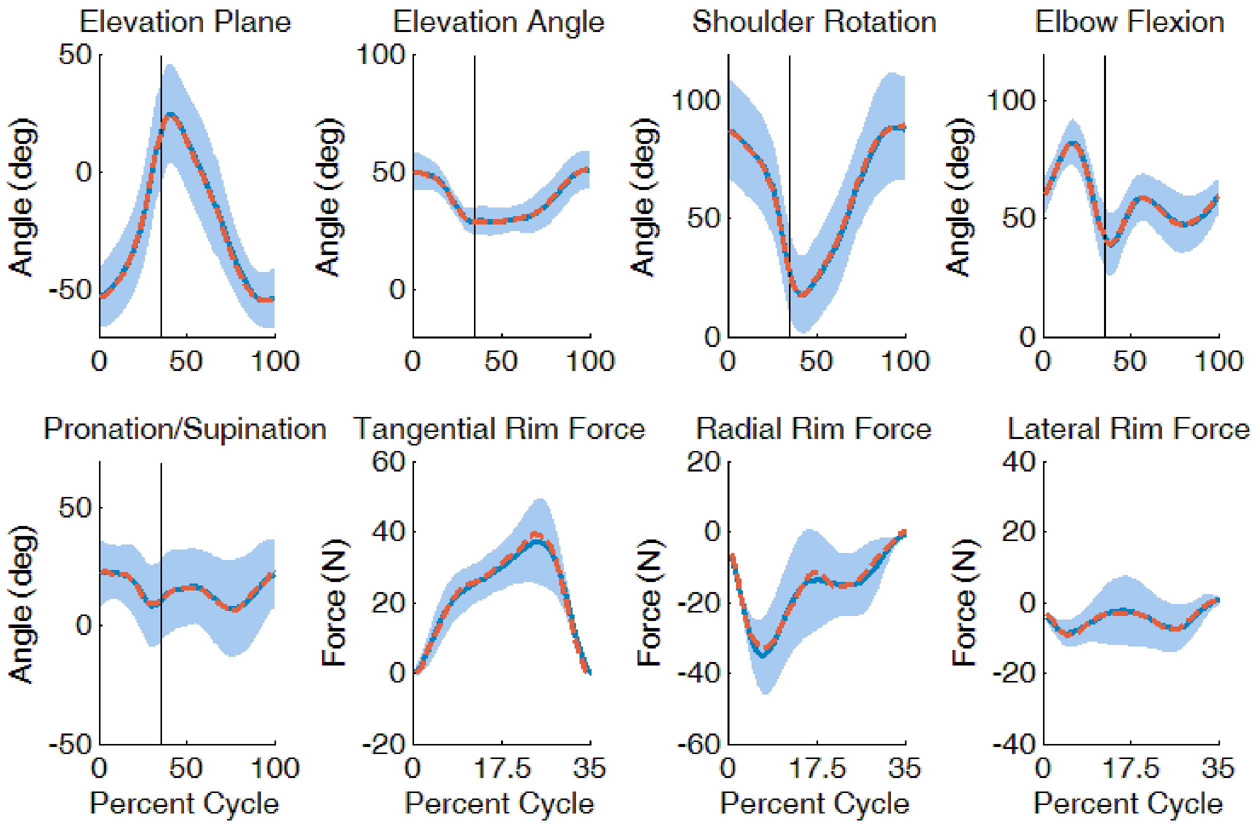

Figure 2.1: Comparison between the baseline simulation and group-averaged experimental mechanics. Experimental and simulation values are represented by solid and dashed lines, respectively. Shaded regions represent ± 1 SD of the experimental data. The joint angle plots depict the full cycle, with the end of the contact phase indicated with a vertical line. The handrim force plots only depict the contact phase, as values are approximately zero throughout the recovery phase.

Table 2.3: Root-mean-square differences between the simulated mechanics and group-averaged experimental mechanics. For comparison, one standard deviation (SD) of the experimental data is provided to indicate the inter-subject variability.

		Simulations													All Simulations	Experimental variability (1 SD)
		Baseline	ADelt	MDelt	Subsc	Supra	Infra	PecMaj	Lat	Tri	Bra	Bic	Sup	Pro		
Joint kinematics (degrees)	Elevation plane	0.8	0.8	0.8	0.7	0.9	0.8	0.8	1.0	0.8	0.8	0.8	0.8	1.0	0.8	17.7
	Elevation angle	0.3	0.3	0.3	0.3	0.4	0.4	0.3	0.4	0.3	0.3	0.3	0.3	0.3	0.3	6.7
	Shoulder rotation	0.8	0.8	0.8	1.2	0.8	1.6	0.9	2.9	0.9	0.9	0.9	0.9	0.9	1.1	20.1
	Elbow flexion	0.5	0.5	0.5	0.5	0.4	0.5	0.5	0.5	0.5	0.4	0.5	0.5	0.4	0.5	10.6
	Pronation/supination	0.6	0.6	0.7	0.7	0.6	0.8	0.7	0.8	0.9	0.8	1.1	0.7	6.2	1.2	16.7
	All joints	0.6	0.6	0.6	0.7	0.6	0.8	0.7	1.1	0.7	0.6	0.7	0.6	1.8	0.8	14.3
Handrim forces (N)	Tangential	1.1	1.2	1.1	1.0	1.3	0.9	1.3	1.2	1.1	1.2	1.1	1.1	1.1	1.1	6.5
	Radial	1.2	0.9	1.1	1.0	1.7	1.6	1.1	1.0	2.6	1.2	1.1	1.0	1.4	1.3	8.9
	Lateral	0.4	0.4	0.5	0.5	1.6	0.9	0.5	0.5	0.7	0.4	0.5	0.4	0.4	0.6	6.0
	All forces	0.9	0.8	0.9	0.8	1.5	1.1	1.0	0.9	1.4	1.0	0.9	0.8	1.0	1.0	7.1

Muscle power

In general, weakness in individual muscle groups was compensated for by power increases from synergistic groups and decreases from antagonistic groups (Tables 2.4 and 2.5). The largest power shifts occurred among the shoulder muscles. The largest individual compensation occurred in ADelt due to Supra weakness, while the next largest compensation also occurred in ADelt but in response to PecMaj weakness. The third largest compensation occurred in MDelt due to Subsc weakness.

Muscle stress

In the baseline simulation, Subsc experienced the highest full-cycle average stress of any muscle group while Supra experienced the second highest level (Fig. 2.2). Supra also experienced the highest full-cycle maximum stress of any muscle group while Infra experienced the second highest level. On an individual muscle level, subscapularis (SUBSC) experienced the highest average stress and teres minor (TMIN) experienced the highest maximum stress, while supraspinatus (SUPSP) and pronator quadratus (PQ) experienced high levels (both average and maximum).

Table 2.4: Total muscle power shifts between muscle groups. Color gradient from red (increase) to green (decrease) represents the change in total muscle power. (For interpretation of the references to color, the reader is referred to the web version of this article). Italics denote a shift greater than 1.50 W.

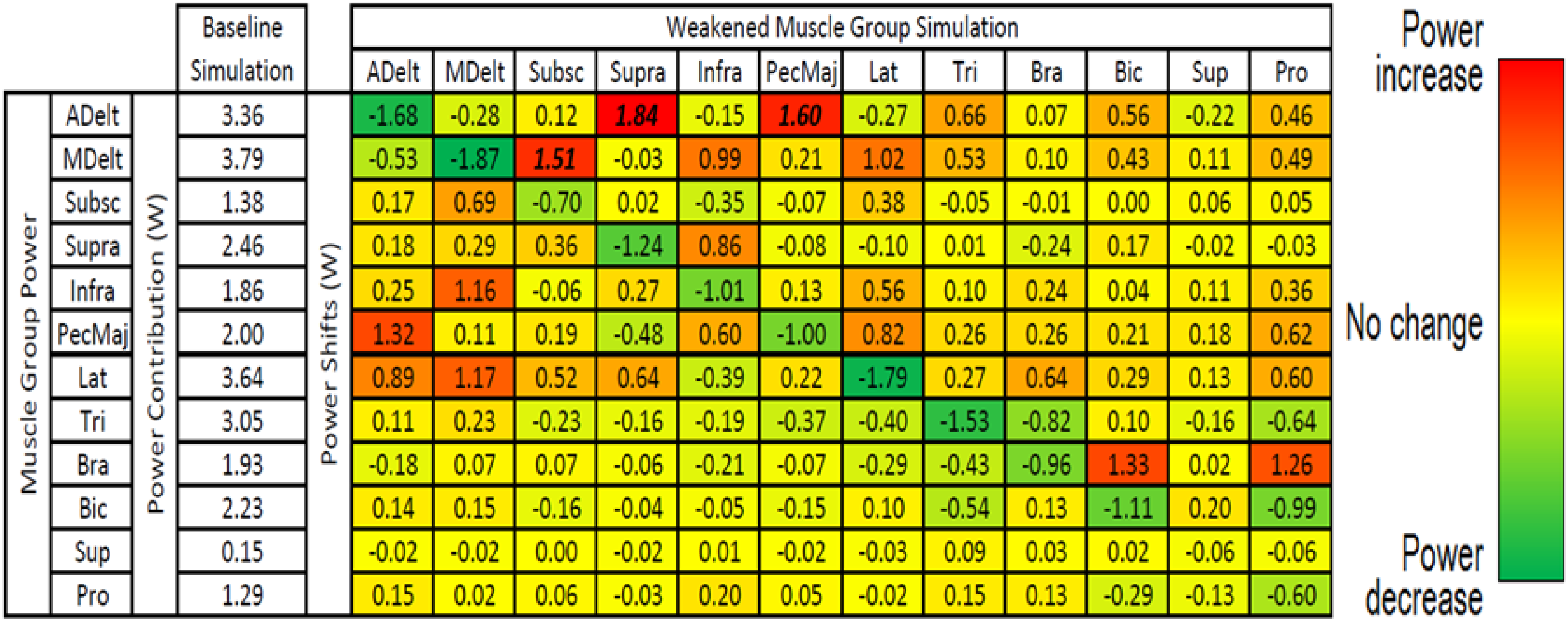

			Baseline Simulation		Weakened Muscle Group Simulation											
					ADelt	MDelt	Subsc	Supra	Infra	PecMaj	Lat	Tri	Bra	Bic	Sup	Pro
Muscle Group Power	ADelt	Power Contribution (W)	3.36	Power Shifts (W)	-1.68	-0.28	0.12	***1.84***	-0.15	***1.60***	-0.27	0.66	0.07	0.56	-0.22	0.46
	MDelt		3.79		-0.53	-1.87	***1.51***	-0.03	0.99	0.21	1.02	0.53	0.10	0.43	0.11	0.49
	Subsc		1.38		0.17	0.69	-0.70	0.02	-0.35	-0.07	0.38	-0.05	-0.01	0.00	0.06	0.05
	Supra		2.46		0.18	0.29	0.36	-1.24	0.86	-0.08	-0.10	0.01	-0.24	0.17	-0.02	-0.03
	Infra		1.86		0.25	1.16	-0.06	0.27	-1.01	0.13	0.56	0.10	0.24	0.04	0.11	0.36
	PecMaj		2.00		1.32	0.11	0.19	-0.48	0.60	-1.00	0.82	0.26	0.26	0.21	0.18	0.62
	Lat		3.64		0.89	1.17	0.52	0.64	-0.39	0.22	-1.79	0.27	0.64	0.29	0.13	0.60
	Tri		3.05		0.11	0.23	-0.23	-0.16	-0.19	-0.37	-0.40	-1.53	-0.82	0.10	-0.16	-0.64
	Bra		1.93		-0.18	0.07	0.07	-0.06	-0.21	-0.07	-0.29	-0.43	-0.96	1.33	0.02	1.26
	Bic		2.23		0.14	0.15	-0.16	-0.04	-0.05	-0.15	0.10	-0.54	0.13	-1.11	0.20	-0.99
	Sup		0.15		-0.02	-0.02	0.00	-0.02	0.01	-0.02	-0.03	0.09	0.03	0.02	-0.06	-0.06
	Pro		1.29		0.15	0.02	0.06	-0.03	0.20	0.05	-0.02	0.15	0.13	-0.29	-0.13	-0.60

Table 2.5: Muscle group power compensations. Key compensations were defined to be those that accounted for at least ten percent of the total magnitude of power shifts that resulted from a muscle group being weakened.

Muscle Group Weakened	**Key Compensations**	
	Increased Power	**Decreased Power**
ADelt	PecMaj, Lat	-----
MDelt	Lat, Infra, Subsc	-----
Subsc	MDelt, Lat	-----
Supra	ADelt, Lat	-----
Infra	MDelt, Supra, PecMaj	-----
PecMaj	ADelt	-----
Lat	MDelt, PecMaj	-----
Tri	ADelt, MDelt	Bic
Bra	Lat	Tri
Bic	Bra, ADelt	-----
Sup	Bic, PecMaj	ADelt, Tri
Pro	Bra, PecMaj	Bic, Tri

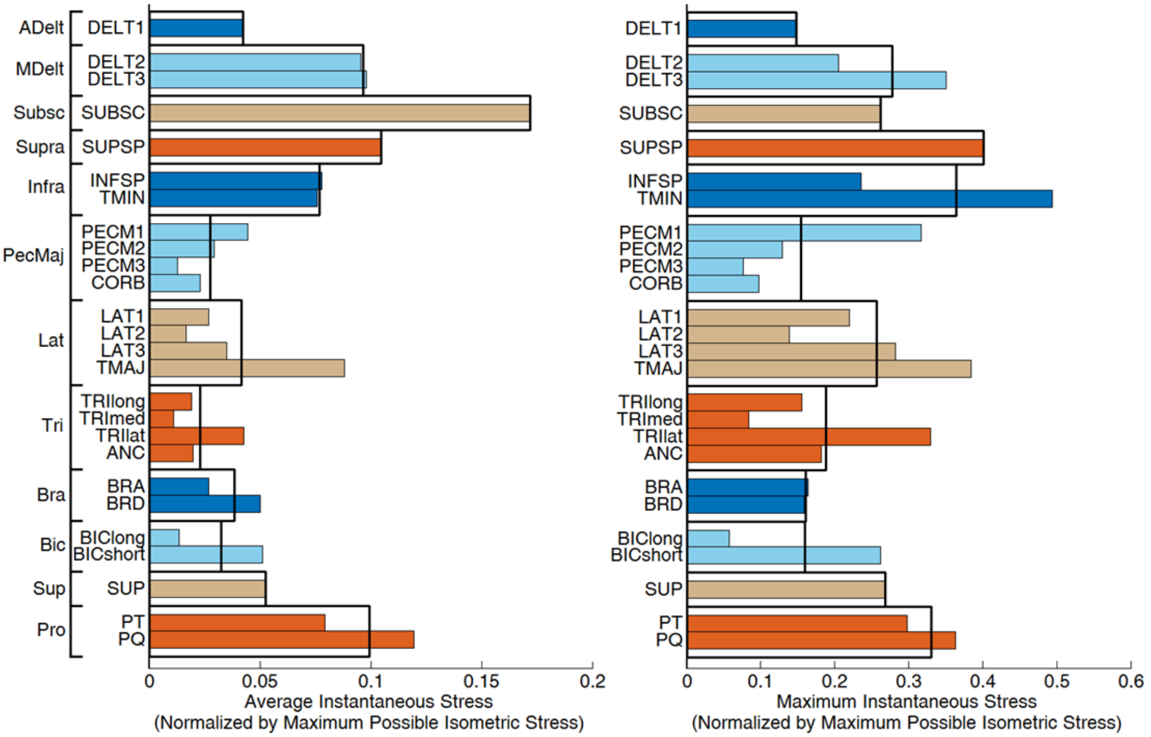

Figure 2.2: Baseline simulation average and maximum stress values over the full cycle for the individual muscles. The thick black boxes correspond to the average value for the muscle group.

In general, when individual muscle groups were weakened, the shifts in stress levels (Tables 2.6 and 2.7) corresponded to the shifts in muscle power contributions (Table 2.4). Muscle groups that compensated with increased muscle power generally experienced an increase in stress while muscle groups that compensated by decreasing their power also saw a decrease in stress. Across simulations, the rotator cuff muscle groups (i.e., Subsc, Supra and Infra) were consistently among the muscle groups with the highest stress levels (Tables 2.6 and 2.7).

Table 2.6: Average stress values over the full cycle for the individual muscle groups. Columns correspond to the different simulations (i.e., the weakened muscle groups). Color gradient from light (low) to dark (high) represents the average stress levels.

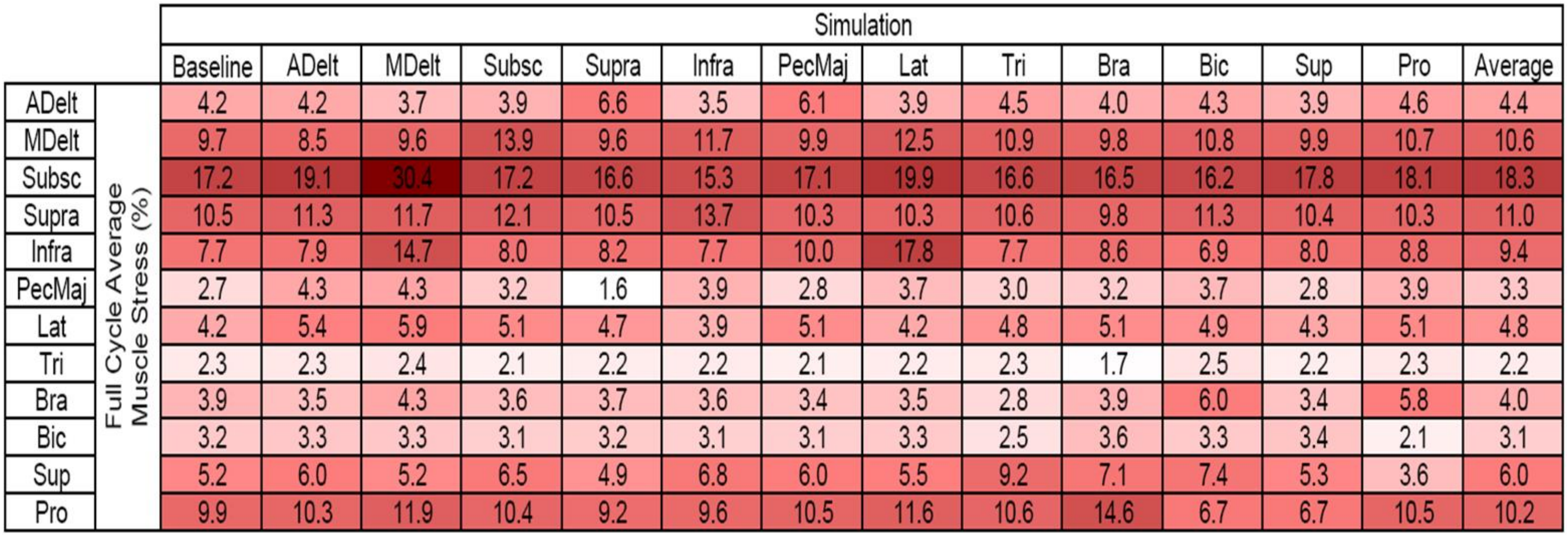

		Simulation													
		Baseline	ADelt	MDelt	Subsc	Supra	Infra	PecMaj	Lat	Tri	Bra	Bic	Sup	Pro	Average
ADelt	Full Cycle Average Muscle Stress (%)	4.2	4.2	3.7	3.9	6.6	3.5	6.1	3.9	4.5	4.0	4.3	3.9	4.6	4.4
MDelt		9.7	8.5	9.6	13.9	9.6	11.7	9.9	12.5	10.9	9.8	10.8	9.9	10.7	10.6
Subsc		17.2	19.1	30.4	17.2	16.6	15.3	17.1	19.9	16.6	16.5	16.2	17.8	18.1	18.3
Supra		10.5	11.3	11.7	12.1	10.5	13.7	10.3	10.3	10.6	9.8	11.3	10.4	10.3	11.0
Infra		7.7	7.9	14.7	8.0	8.2	7.7	10.0	17.8	7.7	8.6	6.9	8.0	8.8	9.4
PecMaj		2.7	4.3	4.3	3.2	1.6	3.9	2.8	3.7	3.0	3.2	3.7	2.8	3.9	3.3
Lat		4.2	5.4	5.9	5.1	4.7	3.9	5.1	4.2	4.8	5.1	4.9	4.3	5.1	4.8
Tri		2.3	2.3	2.4	2.1	2.2	2.2	2.1	2.2	2.3	1.7	2.5	2.2	2.3	2.2
Bra		3.9	3.5	4.3	3.6	3.7	3.6	3.4	3.5	2.8	3.9	6.0	3.4	5.8	4.0
Bic		3.2	3.3	3.3	3.1	3.2	3.1	3.1	3.3	2.5	3.6	3.3	3.4	2.1	3.1
Sup		5.2	6.0	5.2	6.5	4.9	6.8	6.0	5.5	9.2	7.1	7.4	5.3	3.6	6.0
Pro		9.9	10.3	11.9	10.4	9.2	9.6	10.5	11.6	10.6	14.6	6.7	6.7	10.5	10.2

Table 2.7: Maximum stress values over the full cycle for the individual muscle groups. Columns correspond to the different simulations (i.e., the weakened muscle groups). Color gradient from light (low) to dark (high) represents the maximum stress levels.

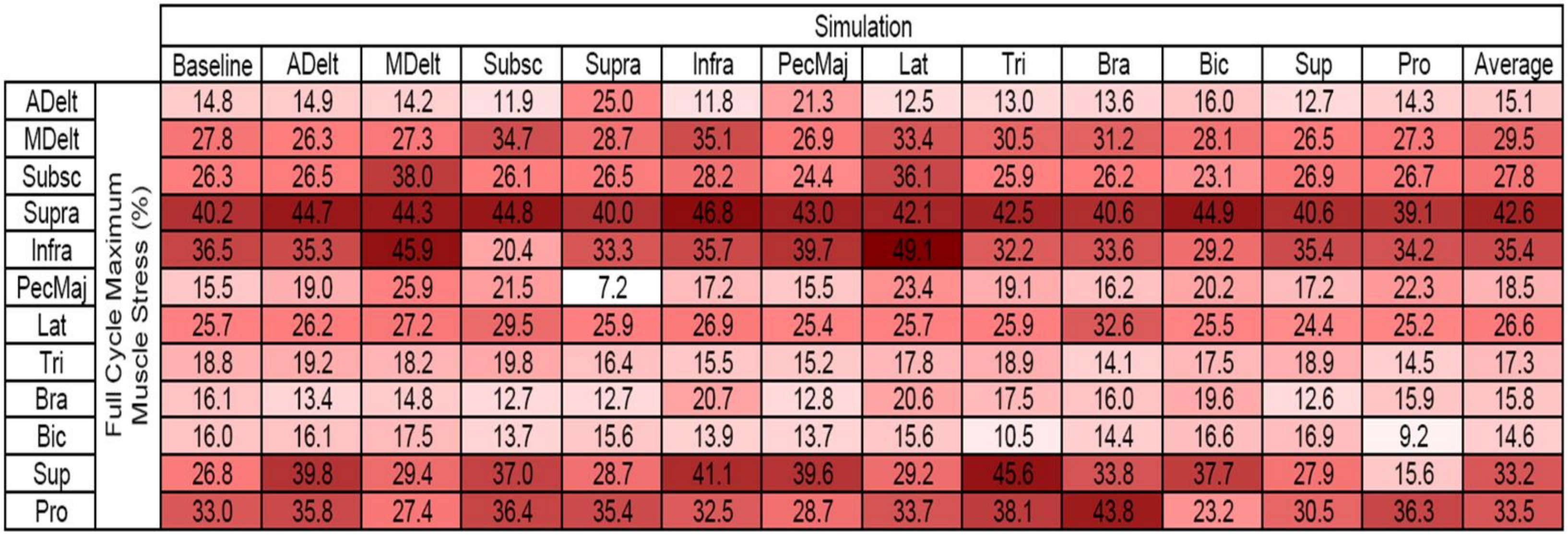

		Simulation													
		Baseline	ADelt	MDelt	Subsc	Supra	Infra	PecMaj	Lat	Tri	Bra	Bic	Sup	Pro	Average
ADelt	Full Cycle Maximum Muscle Stress (%)	14.8	14.9	14.2	11.9	25.0	11.8	21.3	12.5	13.0	13.6	16.0	12.7	14.3	15.1
MDelt		27.8	26.3	27.3	34.7	28.7	35.1	26.9	33.4	30.5	31.2	28.1	26.5	27.3	29.5
Subsc		26.3	26.5	38.0	26.1	26.5	28.2	24.4	36.1	25.9	26.2	23.1	26.9	26.7	27.8
Supra		40.2	44.7	44.3	44.8	40.0	46.8	43.0	42.1	42.5	40.6	44.9	40.6	39.1	42.6
Infra		36.5	35.3	45.9	20.4	33.3	35.7	39.7	49.1	32.2	33.6	29.2	35.4	34.2	35.4
PecMaj		15.5	19.0	25.9	21.5	7.2	17.2	15.5	23.4	19.1	16.2	20.2	17.2	22.3	18.5
Lat		25.7	26.2	27.2	29.5	25.9	26.9	25.4	25.7	25.9	32.6	25.5	24.4	25.2	26.6
Tri		18.8	19.2	18.2	19.8	16.4	15.5	15.2	17.8	18.9	14.1	17.5	18.9	14.5	17.3
Bra		16.1	13.4	14.8	12.7	12.7	20.7	12.8	20.6	17.5	16.0	19.6	12.6	15.9	15.8
Bic		16.0	16.1	17.5	13.7	15.6	13.9	13.7	15.6	10.5	14.4	16.6	16.9	9.2	14.6
Sup		26.8	39.8	29.4	37.0	28.7	41.1	39.6	29.2	45.6	33.8	37.7	27.9	15.6	33.2
Pro		33.0	35.8	27.4	36.4	35.4	32.5	28.7	33.7	38.1	43.8	23.2	30.5	36.3	33.5

DISCUSSION

For all the simulations, the optimization framework was able to identify muscle excitation patterns that produced propulsion mechanics that emulated well the group-averaged experimental data. The simulation tracking performance illustrates the ability of the upper extremity muscles to compensate for weakness in individual muscle groups and produce normal (group-averaged) propulsion mechanics.

Muscle power

The deltoid and rotator cuff muscle groups (i.e., ADelt, MDelt, Subsc, Supra and Infra) were among the largest contributors to propulsion. These muscles have also been highlighted as key contributors to generating needed mechanical power in previous simulation (e.g., Rankin et al., 2011) and experimental (e.g., Mulroy et al., 1996) analyses. The large power shifts observed between these muscle groups suggest that they can compensate for each other to restore normal propulsion mechanics, which is consistent with investigations that have found these muscle groups to have similar and overlapping functional capabilities (e.g., Escamilla et al., 2009; Liu et al., 1997).

Although the deltoid and rotator cuff muscles can produce similar moments about the shoulder, they do so with different combinations of force vectors and moment arms (e.g., Fig. 2.3). Therefore, shifts in contribution between these muscle groups could potentially decrease joint stability and increase injury risk. A previous study investigating the effects of rotator cuff tears highlighted this injury mechanism using an inverse dynamics-based model (van Drongelen et al., 2013). The investigators found that rotator cuff tears, simulated by eliminating the force-generating capacity of the individual muscles, can lead to increased deltoid activity and a more superiorly-directed glenohumeral contact force during wheelchair propulsion. This force vector alteration can initiate an injury mechanism in which the humeral head migrates upward into the subacromial space causing rotator cuff impingement. Superior migration of the humeral head after rotator cuff fatigue has also been shown using experimental measurements (e.g., Teyhen et al., 2008).

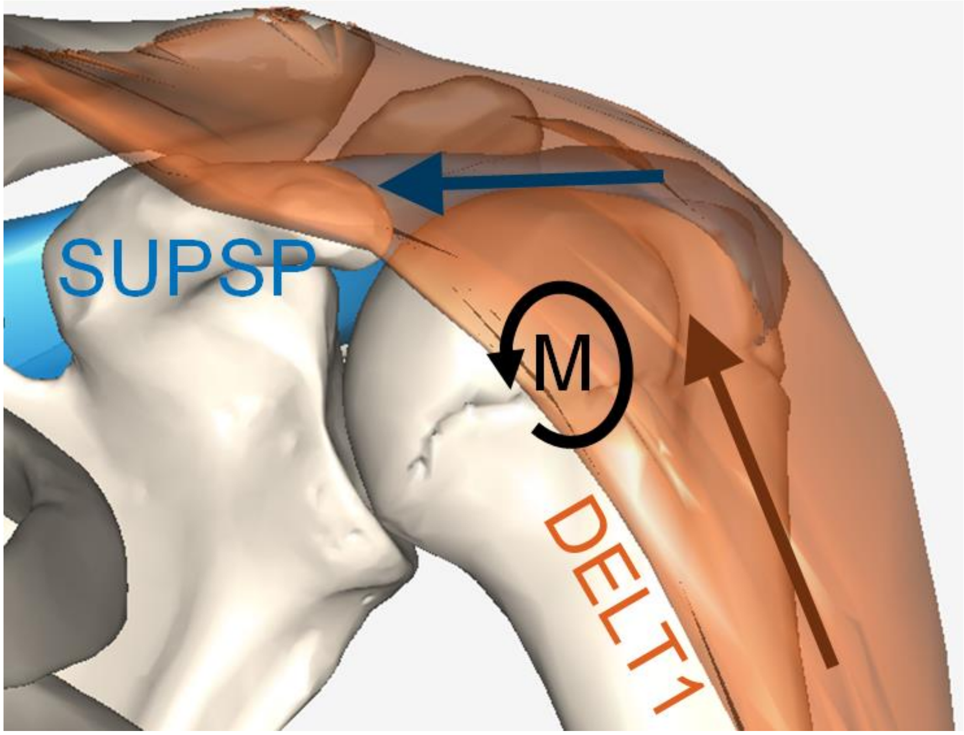

Figure 2.3: Moment (M) created by the forces generated by supraspinatus (SUPSP) and anterior deltoid (DELT1). While both muscles can produce an abduction moment, the supraspinatus force draws the humeral head towards the glenoid fossa while the anterior deltoid provides a more superiorly directed force.

The thoracohumeral depressors (i.e., PecMaj and Lat) are capable of counteracting this superior humeral head migration and increasing joint stability by drawing the humeral head towards the glenoid fossa (e.g., Oh et al., 2011), with the smaller negative side effect of increased co-contraction due to the associated adduction moment (Steenbrink et al., 2009). Therefore, compensations involving the thoracohumeral depressors are likely preferable compared to those dominated by the deltoid. The distinctions between ADelt and PecMaj in particular may be important as our results also showed that these muscles compensate for each other to provide much of the power required to propel the wheelchair during the push phase.

Muscle stress

The rotator cuff muscles experienced high stress values in the various simulations, which is consistent with previous inverse dynamics-based analyses (Lin et al., 2004; Veeger et al., 2002). These results are also consistent with previous studies suggesting that the rotator cuff muscles are highly active during wheelchair propulsion (e.g., Mulroy et al., 1996; Rankin et al., 2011) and susceptible to fatigue (Newsam et al., 2008). High stress levels could also lead to rotator cuff degeneration and tearing (e.g., Nho et al., 2008), which could further contribute to the power shifts observed in the previous section.

Although Pro experienced high stress levels, it also had the lowest muscle power contributions. The high stress levels were primarily due to the relatively small size of these muscles and lack of synergistic muscles to help compensate. The possibility of reducing the amount of pronation while still achieving the propulsive task (e.g., Newsam et al., 1999), along with the low occurrence of pronator injuries and the inherent stability of the pronation/supination degree-of-freedom, suggests that the associated injury risk is much lower for Pro compared to the rotator cuff muscles.

Clinical implications

Manual wheelchair users have an elevated risk of rotator cuff injury with tears of the supraspinatus tendon being especially common (Morrow et al., 2014). Glenohumeral joint biomechanics can be affected by rotator cuff injuries and have been found to be critically altered when there is a complete supraspinatus tear (Oh et al., 2011). Rotator cuff injuries are produced by a combination of factors such muscle stress, overuse and extrinsic mechanisms such as impingement (Seitz et al., 2011). Therefore, strengthening of the rotator cuffs muscles and supporting muscles whose contributions do not increase the risk for impingement (i.e., the thoracohumeral depressors) has the potential to reduce the development of shoulder pain and injury.

Study limitations

A potential limitation in this study is that the experimental data was collected on a calibrated wheelchair ergometer rather than overground. However, while stationary propulsion simulators do not perfectly replicate overground propulsion, they provide greater control over experimental variables in a laboratory setting while still resulting in propulsion mechanics consistent with overground propulsion (Koontz et al., 2012). Thus, the advantage of having steady-state data was deemed to outweigh the limitations the ergometer data may present. Another limitation is that the musculoskeletal model did not include the wrist muscles and the joint was fixed in the anatomical position, thus reducing the ability of the hand to produce a pure moment at the handrim. However, wrist moments are generally small relative to shoulder and elbow moments (e.g., Robertson et al., 1996; Sabick et al., 2004). In addition, the consistency of the model across all simulations and the requirement that final optimized simulations produce the same experimental joint kinematics and handrim forces minimize the effect of the fixed wrist on the other joints and the study conclusions.

A final limitation is that the compensatory strategies identified by the simulations are not the only ones possible. While the identified strategies restore the group-averaged propulsion mechanics while minimizing excess co-contraction, the specific compensatory strategy used by an individual may be influenced by subject-specific differences in muscle capacities and preferred propulsion technique. In addition, it is possible that a subject would modify their propulsion mechanics in response to individual muscle weakness instead of seeking to maintain their original pattern. An interesting future study would be to assess the influence of individual muscle weakness on propulsion mechanics.

CONCLUSIONS

In summary, this study details the effects of individual muscle weakness during manual wheelchair propulsion and highlights the potential risks for the development of upper extremity pain and injury. Despite significant reductions in individual muscle strength, wheelchair propulsion mechanics were able to be restored through compensations from other muscle groups. The largest intermuscular compensations occurred within the shoulder muscles. The simulation results indicate that the deltoid and rotator cuff muscles can produce moments to compensate for each other. However, shifts between these muscles may compromise glenohumeral stability and lead to impingement or other similar injuries. Stability can be increased through additional contributions from the thoracohumeral depressors, but with the possible consequence of increased co-contraction. The rotator cuff muscles also experienced many of the highest stress levels across simulations, further highlighting their susceptibility to fatigue and injury. These results highlight the importance of strengthening the rotator cuff muscles and supporting muscles whose contributions do not increase the risk for impingement (i.e., the thoracohumeral depressors) in rehabilitation interventions aimed at minimizing the risk of upper extremity injury in manual wheelchair users.

Chapter 3: The Influence of Speed and Grade on Wheelchair Propulsion Hand Pattern

INTRODUCTION

The manual wheelchair propulsion cycle can be divided into contact and recovery phases (e.g., Kwarciak et al., 2009). During the contact phase, the user delivers mechanical power to the wheelchair via contact with the handrim and consequently the hand is constrained to the handrim. During the recovery phase, the user repositions the arm and hand in preparation for the next stroke. The hand is far less constrained during the recovery phase and can follow any number of paths in preparation for the next cycle. This relative freedom leads to a wide spectrum of possible hand patterns (i.e., full-cycle hand paths) that are frequently classified into four pattern types based on the shape of their projection onto the plane of the handrim (Fig. 3.1): arcing (AR), single loop (SL), double loop (DL) and semi-circular (SC) (e.g., Boninger et al., 2002). DL and SC are sometimes grouped together and designated as under-rim patterns, which is a term describing the location of the hand just prior to initiation of contact with the handrim (Kwarciak et al., 2009). As the movement of the hand is closely linked with propulsion mechanics, the hand pattern is a clinically visible indicator that can provide insight into an individual's propulsion technique (e.g., Shimada et al., 1998).

Previous studies classifying hand patterns have primarily used subjective and qualitative methods (e.g., de Groot et al., 2008; Shimada et al., 1998). However, hybrid patterns occur and the lack of objective methods to classify them can lead to inconsistencies between studies (Koontz et al., 2009). Early studies relied on a single rater system (e.g., Boninger et al., 2002), but recent investigations have attempted to minimize the influence of subjectivity by using a multiple rater classification procedure (Koontz et al., 2009; Kwarciak et al., 2012). One study used a set of quantitative parameters and data clustering techniques to distinguish between pattern types (Aissaoui and Desroches, 2008). However, while their investigation revealed four distinct pattern types, three resembled variants of AR and the fourth resembled SL. None of their identified patterns resembled SC or DL, despite the prevalence of these patterns in other studies. A more recent study attempted to characterize hand patterns using a complex set of quantitative parameters such as maximum length and height (Stephens and Engsberg, 2010). However, they did not attempt to use these parameters to distinguish between pattern types, instead relying on typical subjective classification methods.

Most hand pattern studies have focused on level propulsion at a self-selected speed. However, daily living activities often require an individual to propel their wheelchair under more intense conditions (e.g., at a higher speed or up a graded surface) that may place the upper extremity at a higher risk for injury. Both speed and grade have been shown to influence propulsion spatiotemporal characteristics (e.g., van der Woude et al., 1988), joint kinetics (Kulig et al., 1998) and muscle activity (e.g., Chow et al., 2009). However, studies investigating their influence on hand patterns have been limited. One study has suggested that an increase in propulsion speed may lead to fewer individuals selecting an under-rim hand pattern (Boninger et al., 2002). Others have suggested that individuals may be more likely to use AR when encountering a higher grade of incline (Richter et al., 2007), with the investigators attributing this preference to previous results suggesting that AR may be the most biomechanically efficient pattern (de Groot et al., 2004). However, as these studies specified hand pattern solely as a categorical variable, changes in patterns could only be quantified by the number of individuals that crossed a subjective threshold between patterns.

The purpose of this study was to develop a set of objective quantitative parameters to characterize hand patterns and determine the influence of propulsion speed and grade of incline on the patterns preferred by manual wheelchair users. Based on previous study observations, we hypothesized that (1) increased propulsion speed would result in a shift away from under-rim patterns (DL and SC), and (2) increased grade would result in a shift toward the AR pattern.

METHODS

Subjects

Experimental data were collected from 170 individuals with complete motor paraplegia and free of shoulder pain (153 men; age: 34.9±9.1 yrs; time from injury: 9.6±6.2 yrs; height: 1.74±0.09 m; mass: 75.0±16.5 kg). Participants were recruited from outpatient clinics throughout the Rancho Los Amigos National Rehabilitation Center and provided informed written consent in accordance with the Institutional Review Board.

Data collection

Each participant propelled their own wheelchair on a stationary ergometer during 3 conditions: free, fast and graded. For the free condition, subjects performed level propulsion at their self-selected free speed (1.04 ± 0.30 m/s) with the resistance level set similar to overground propulsion over a tile surface (e.g., Raina et al., 2012). For the fast condition, subjects performed level propulsion at their fastest comfortable speed (1.90 ± 0.46 m/s). For the graded condition, subjects performed at their level self-selected speed (1.05 ± 0.30 m/s) but with the front end of the ergometer elevated and resistance level increased to simulate propulsion at an 8% incline (e.g., Lighthall-Haubert et al., 2009).

Subjects acclimated to each condition until they felt comfortable, and a 10-second trial (preceded by at least 30 seconds of propulsion to ensure near steady-state propulsion) was recorded for each condition. Trunk, right-side upper extremity and wheel kinematics were collected using a CODA motion analysis system (Charnwood Dynamics Ltd., Leicestershire, UK) with 15 active markers placed on landmarks on the body and right wheel. Three-dimensional right-side handrim kinetics were measured using an instrumented wheel (SmartWheel; Three Rivers Holdings, Mesa, AZ, USA).

Data processing

Kinematic and kinetic data were low-pass filtered with a fourth-order zero-lag Butterworth filter with cutoff frequencies of 8 Hz and 10 Hz, respectively, using Visual3D (C-Motion, Inc., Germantown, MD, USA). A resultant handrim force threshold of 5N was used to delineate between contact and recovery phases. Contact and recovery phase data for each cycle were time-normalized and averaged across propulsion cycles within each subject. Cadence, contact percentage (i.e., percentage of cycle time spent in the contact phase) and the average (F_{avg}) and peak (F_{peak}) resultant handrim forces were calculated for each cycle and then averaged across cycles.

Pattern characterization

The third metacarpophalangeal joint center (MCP3) was located using a previously described method (Rao et al., 1996), and the average MCP3 path was projected onto the plane of the handrim resulting in a closed curve (e.g., Fig. 3.1) to define the hand pattern. Next, a multiple rater system was used to classify each pattern into one of the four previously defined types (Fig. 3.1). Custom Matlab (Mathworks Inc., Natick, MA, USA) code displayed the individual hand patterns to the rater in a random order. Two raters that were familiar with the literature on propulsion hand patterns independently classified each hand pattern based solely on the displayed image of the hand pattern. In the case of a disagreement between raters, a third rater independently classified the hand pattern into one of the two hand pattern types chosen by the first two raters.

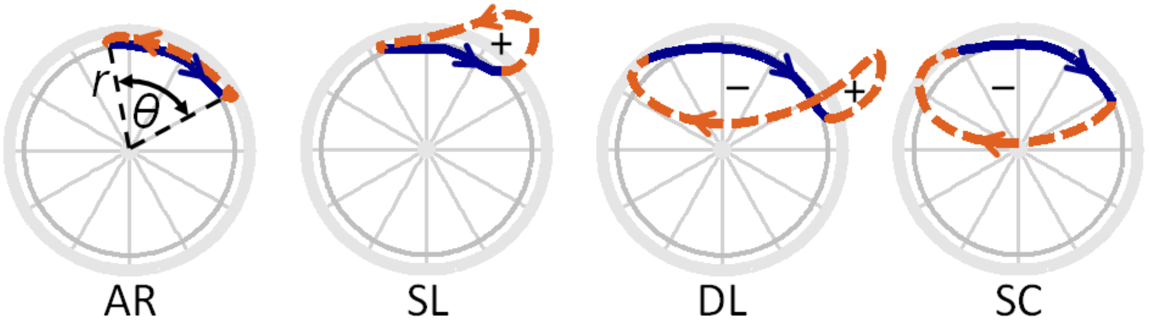

Figure 3.1: Hand pattern and variable definitions. The four hand pattern types are arcing (AR), single loop (SL), double loop (DL) and semi-circular (SC). The solid line denotes the contact phase, while the dashed line denotes the recovery phase. Also depicted is the radius of the handrim (r) and angle of handrim contact (θ). The mathematical signs denote whether the signed area enclosed by each loop is positive (+) or negative (-).

Each pattern was also objectively characterized using two newly developed parameters, net (linear sum) radial thickness, NRT (Eqn. 1), and total (absolute value sum) radial thickness, TRT (Eqn. 2) as follows:

$$\mathrm{NRT} = \frac{\sum_{i=1}^{nloops} A_i}{r\theta} \tag{1}$$

$$\mathrm{TRT} = \frac{\sum_{i=1}^{nloops} |A_i|}{r\theta} \tag{2}$$

where $nloops$ is the number of loops in the curve, A_i is the signed area enclosed by the ith loop of the curve, r is the radius of the handrim, and θ is the angle of handrim contact (Fig. 3.1). The number of loops was calculated using custom Matlab code that determined the number of curve intersections.

The signed area was calculated using the surveyor's area formula, which is a special case of Green's theorem (e.g., Braden, 1986), such that counter-clockwise loops resulted in positive values and clockwise loops resulted in negative values (Fig. 3.1). Using this convention, positive NRT values denote hand patterns that are primarily over-rim (e.g., SL), while negative NRT values denote hand patterns that are primarily under-rim (e.g., SC). Meanwhile, small TRT values denote patterns in which the hand remains near the handrim (e.g., AR), while large TRT values denote patterns in which the hand moves farther away from the handrim (e.g., SL, SC, DL). As a result, on a two-dimensional plot with the vertical axis corresponding to TRT and the horizontal axis corresponding to either the ratio NRT/TRT (e.g., Fig. 3.2) or NRT (e.g., Fig B.1 in Appendix B), a set of basic thresholds can divide the space into four regions that correspond to the four commonly observed hand pattern types. When used in coordination with TRT, the ratio NRT/TRT is helpful for pattern type classification and can improve figure clarity in the AR region. However, independently the NRT/TRT ratio is limited in its ability to differentiate between multiple patterns as it provides no information about pattern thickness. Therefore, NRT is more useful when comparing across conditions. To help validate the use of these new parameters to quantify hand patterns, the pattern type corresponding to the calculated parameters was compared with the pattern type identified by the multi-rater system.

Statistical analyses

To determine if propulsion condition affected the hand pattern, statistical analyses were performed using SPSS (IBM Corp., Armonk, NY, USA). Differences in the propulsion variables (NRT, TRT, θ, cadence, contact percentage, F_{avg} and F_{peak}) were assessed using a one-factor (propulsion condition) repeated measures ANOVA with three levels (free, fast and graded). When a significant main effect was found, pairwise comparisons were performed using paired t-tests with a Bonferroni adjustment for multiple comparisons. The unadjusted threshold for statistical significance for all analyses was set at $\alpha=0.05$.

RESULTS

With pattern type thresholds set at TRT = 0.03m, NRT/TRT = -0.95 and NRT/TRT = +0.95, the objective pattern classification method and the subjective multi-rater method produced the same results 90% of the time (Fig 3.2, Fig B.1).

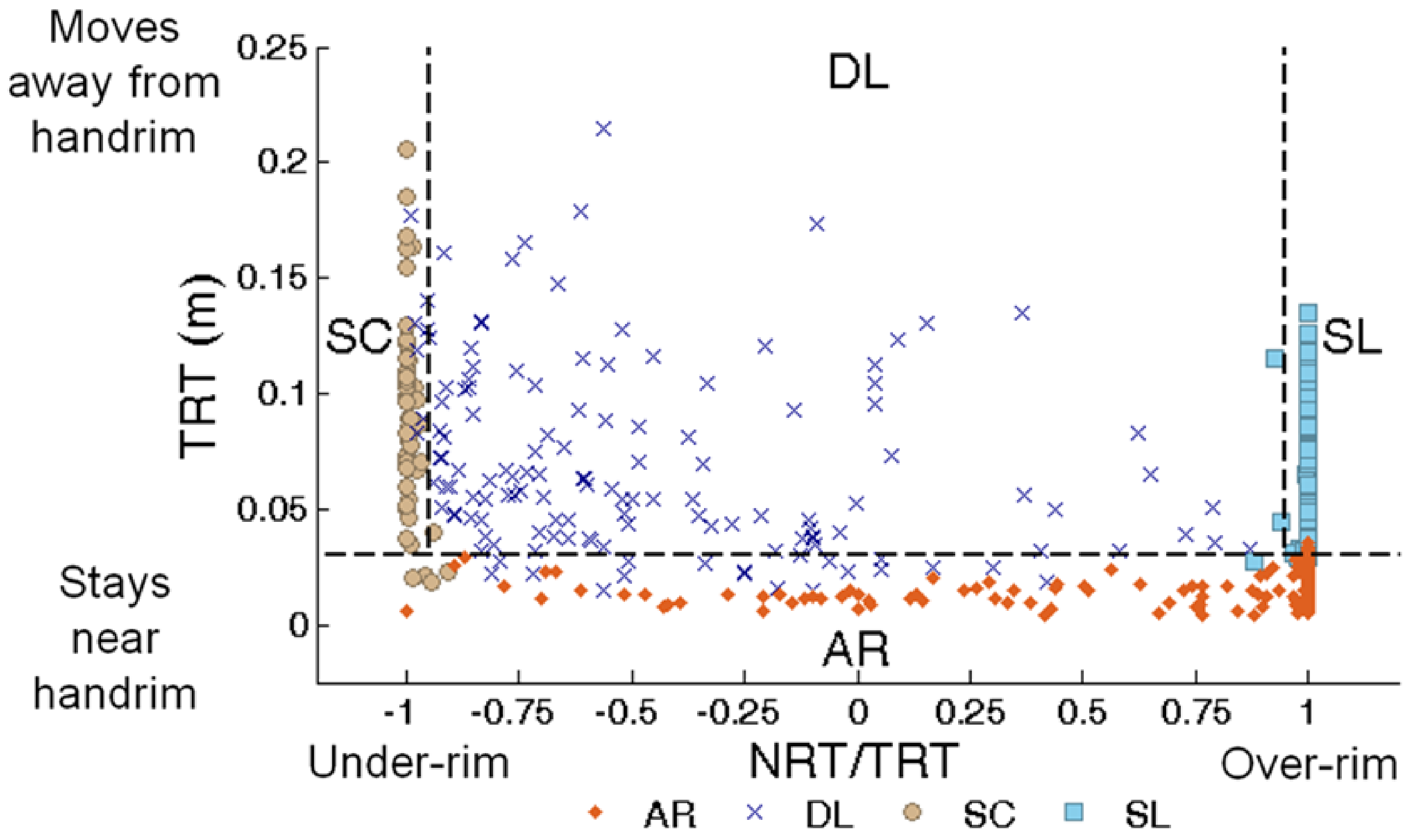

Figure 3.2: Comparison of objective and subjective hand pattern classification results. The vertical axis corresponds to TRT and the horizontal axis corresponds to the ratio NRT/TRT. Thresholds for the objective classification are depicted with the dashed lines at TRT = 0.03m, NRT/TRT = -0.95 and NRT/TRT = 0.95. Regions corresponding to each pattern type are labeled with the objective classification. Subjective classification is indicated with the following symbols: AR (◆), DL (×), SC (●) and SL (■). For figure clarity, NRT/TRT was selected as the horizontal axis variable instead of NRT.

All variables were found to have a significant propulsion condition main effect ($p<0.001$). The pairwise comparisons showed that compared to the free condition, the fast condition resulted in significantly higher NRT, θ, cadence, F_{avg} and F_{peak} and significantly lower contact percentage (Table 3.1, $p<0.001$). The fast condition also resulted in significantly higher TRT ($p=0.006$). Compared to the free condition, the graded condition resulted in significantly lower TRT and significantly higher NRT, θ, cadence, contact percentage, F_{avg}, and F_{peak} ($p<0.001$). Compared to the fast condition, the graded condition resulted in significantly lower TRT and significantly higher θ, contact percentage, F_{avg}, and F_{peak}. The propulsion pattern changes across conditions were also evident in a plot of TRT vs. NRT (Fig. 3.3) or TRT vs. NRT/TRT (Fig B.2), as well as the number of wheelchair users corresponding to each propulsion type (Table 3.2).

Table 3.1: Mean (SD) values of the propulsion variables for each condition.

	Propulsion Condition			**Significant Comparisons [α=0.05]**
	Free	**Fast**	**Graded**	
NRT [m]	-0.0219 (0.0555)	0.0103 (0.0585)	0.0095 (0.0309)	□▨
TRT [m]	0.0529 (0.0401)	0.0601 (0.0418)	0.0261 (0.0224)	□▨■
θ [deg]	78.3 (15.7)	83.7 (14.2)	88.1 (14.2)	□▨■
Cadence [Hz]	0.890 (0.218)	1.312 (0.318)	1.258 (0.269)	□▨
Contact Percentage [% Cycle]	37.6 (7.6)	34.0 (7.2)	60.0 (6.8)	□▨■
F_{avg} [N]	29.7 (8.0)	42.8 (13.0)	74.0 (18.0)	□▨■
F_{peak} [N]	46.2 (15.3)	79.3 (29.6)	124.5 (32.3)	□▨■

□ denotes a significant free to fast pairwise comparison
▨ denotes a significant free to graded pairwise comparison
■ denotes a significant fast to graded pairwise comparison

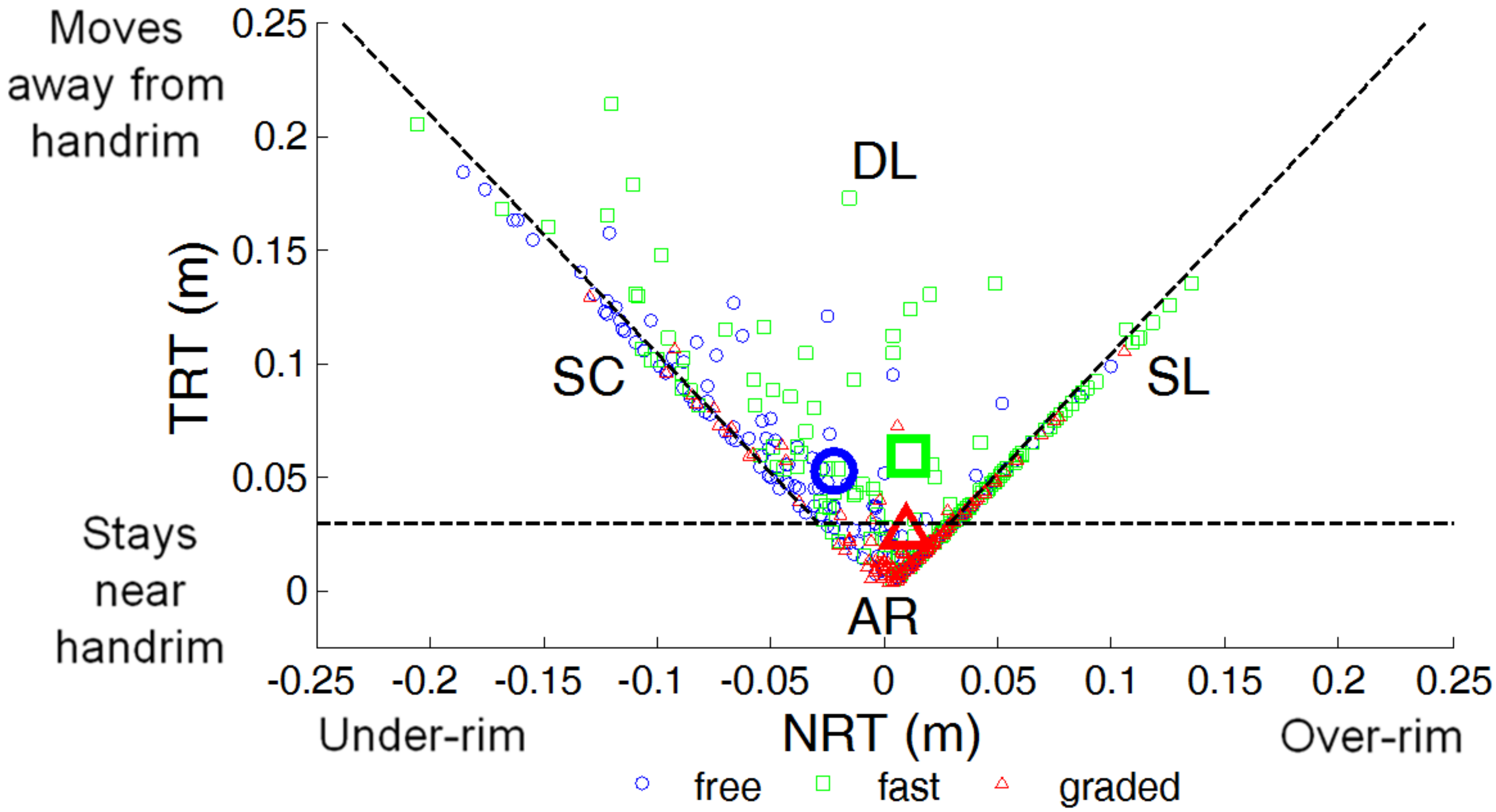

Figure 3.3: Hand pattern parameter values across conditions. The vertical axis corresponds to TRT and the horizontal axis corresponds to NRT. Thresholds for the objective classification are depicted with the dashed lines at TRT = 0.03m, NRT/TRT = -0.95 and NRT/TRT = 0.95. Regions corresponding with each pattern type are labeled with the objective classification. Propulsion condition is indicated as follows: free (○), fast (□) and graded (△). The across-subject mean values are indicated with a larger version of the same symbols. For comparisons across conditions, NRT was selected as the horizontal axis variable instead of NRT/TRT.

Table 3.2: Number of wheelchair users (percentage) using each hand pattern type across conditions using the objective classification method.

	Condition		
	Free	**Fast**	**Graded**
AR	63 (37.1%)	46 (27.1%)	125 (73.5%)
SL	24 (14.1%)	61 (35.9%)	26 (15.3%)
DL	49 (28.8%)	55 (32.4%)	12 (7.1%)
SC	34 (20.0%)	8 (4.7%)	7 (4.1%)

DISCUSSION

Manual wheelchair users encounter a variety of propulsion conditions throughout their daily living activities that require modifications to their propulsion technique. The hand pattern is a clinically observable indicator that can provide insight into an individual's propulsion technique, but studies analyzing the influence of propulsion condition on hand patterns have been limited. This study used a set of objective quantitative parameters to assess the influence of speed and grade of incline on the preferred hand patterns used by manual wheelchair users.

The finding that NRT was significantly larger in the fast condition than during the free condition supports the hypothesis that increased propulsion speed would result in a shift away from under-rim patterns and is consistent with previous research showing a decrease in the number of under-rim patterns used with increasing speed (Boninger et al., 2002). This increase in NRT may be a result of the arm inertia and its increased velocity during the contact phase. At the beginning of the recovery phase, shoulder motion transitions from flexion to extension (e.g., Rao et al., 1996). Thus, the increased velocity of fast propulsion would prolong the transition unless there was an offsetting increase in the extensor moment at the shoulder (which would increase energy demands). A delayed transition would result in additional shoulder flexion and encourage the hand to move above the handrim during this period. This initial movement would likely lead to increases in both NRT and TRT, which is consistent with our results. The prolonged transition would also require an increase in the percentage of cycle time spent in the recovery phase, which is consistent with the significant decrease in contact percentage we observed.

In order to increase power output to the handrim, either θ, cadence and/or handrim force must increase. When increasing propulsion speed on level ground, users increased all of these parameters (Table 3.1). While there was a small increase in θ (6.9%), there were much larger increases in cadence, F_{avg} and F_{peak} (47.4%, 44.1%, and 71.6%, respectively). These results are consistent with previous studies suggesting that an increase in speed leads to an increase in cadence and force, but a decrease in contact percentage (e.g., Boninger et al., 2002; Chow et al., 2009). While only one study found a statistically significant increase in θ (Gil-Agudo et al., 2010), others have shown increases in θ similar to those in the present study (e.g., Boninger et al., 2002; Koontz et al., 2002). Since most of these studies used a limited number of subjects, it is possible that they would have found statistical significance with a larger sample size.

The finding that TRT was significantly smaller in the graded condition compared to the free condition supports the hypothesis that increased grade would result in a shift toward the AR pattern. This result is consistent with a previous study showing an increase in number of AR patterns with increasing grade of incline (Richter et al., 2007). Propulsion in the graded condition required increased contact percentage (and decreased recovery percentage). This may encourage the selection of a shorter recovery hand path, contributing to the decrease in TRT. Furthermore, individuals must keep the hand near the handrim in order to prevent the wheelchair from rolling backward while on the incline. In addition to the decrease in TRT, there was also an increase in NRT with increased grade of incline, which appears to be related to the decrease in the number of under-rim patterns and corresponding increase in the number of AR patterns (Table 3.2). While under-rim patterns have negative NRT values, AR patterns on average have small but positive NRT values due to the large quantity of AR patterns in which the hand never drops below the handrim (i.e., along the rightmost edge of the AR regions in Figs. 3.2 and 3.3). This concentration may be explained by examining the ergonomics of the standard handrim grip. The thumb is placed along the top surface while the rest of the hand wraps laterally around the rim such that the fingers contact the bottom surface (e.g., Koontz et al., 2006). When the fingers are opened slightly to relax the grip, the hand can disengage from the handrim with either an upward or lateral movement, but the placement of the thumb prevents an initial downward movement. As there is minimal movement away from the handrim during the AR pattern, this initial constraint may encourage the hand to move slightly above the handrim instead of slightly below.

To achieve the substantial power increase between the free and graded conditions, users increased θ, cadence and force, which showed a similarity to the changes observed when moving between the free and fast conditions. Similarly, the smallest increase was in θ (12.5%). However, while the increase in cadence was similar to that seen with increased speed (41.3%), there was a much larger increase in the handrim force (F_{avg}: 149.2%, F_{peak}: 169.5%). These results are similar to studies showing an increased grade results in increases in both contact percentage (e.g., van der Woude et al., 1988) and handrim force (e.g., Gagnon et al., 2014; Richter et al., 2007). However, there is disagreement between studies on the influence of grade on cadence. While some studies agree with the present results suggesting that cadence increases with grade (Gagnon et al., 2014; van der Woude et al., 1988), others have found that cadence decreases with grade (Richter et al., 2007). This discrepancy is likely due to differences in the study protocols. Richter et al. (2007) allowed their subjects to reduce their speed with grade, while the other studies had their subjects maintain their level ground speed. There is also little consensus regarding the influence of grade on θ. While one study found a significant decrease in θ with increased grade (Richter et al., 2007), others suggest that there may not be a consistent trend across a full range of typical incline grades (Chow et al., 2009; Gagnon et al., 2014; van der Woude et al., 1988). These differences may also be due to differences in study methods and numbers of subjects analyzed.

The results of the present study suggest that speed and grade significantly influence preferred hand patterns and related parameters. While differences in individual anthropometrics, strength and functional capacity among wheelchair users may prevent the identification of a single optimal hand pattern for all subjects (Raina et al., 2012), task-specific constraints and required upper extremity demand likely preclude the existence of a single optimal hand pattern for all tasks (Richter et al., 2007).

The hand pattern characterization method presented in this study has a number of advantages over previously used methods. The method can be used not only to classify hand patterns as one of the four commonly described pattern types but also characterize patterns using quantitative parameters that can differentiate between patterns of the same type, which can be challenging using subjective methods. This quantitative data also enables statistical analyses (e.g., Table 3.1) and clear illustrations of trends (e.g., Fig. 3.3). The output can also help a clinician gain a greater understanding of an individual's propulsion technique across conditions or in different wheelchair configurations. The method could therefore be adapted into an algorithm that could assist a clinician by suggesting beneficial alterations to configuration and/or technique as part of a wheelchair fitting and propulsion training program. The method can also be adapted for a clinical or real-world setting easily, because although we used SmartWheel data to separate individual cycles, simple geometric limits could be used instead. Thus, data collection could be simplified to a single camera recording hand motion in the sagittal plane.

While the method has these advantages, it is not without limitation. One limitation is that the experimental data was not collected overground but instead on a calibrated wheelchair ergometer. Although ergometers are unable to replicate every aspect of overground propulsion, they have been shown to produce steady-state propulsion mechanics that are consistent with overground data while also providing precise control over the experimental conditions (e.g., Koontz et al., 2012). In addition, while differences between overground and simulated propulsion may induce small changes to hand patterns (Stephens and Engsberg, 2010), this study examined relative differences between propulsion conditions and the same ergometer was used throughout the data collection. Thus, the use of an ergometer likely did not influence the study conclusions.

Another potential limitation is related to the thresholds used to delineate between pattern types based on their NRT and TRT values. These thresholds were selected in an attempt to reproduce the subjective classifications and are therefore effectively a quantification of the subjective opinions of the individual raters. While the success rate for the current data set could have been increased by further optimizing the thresholds and increasing their precision (e.g., adding decimal places), it is unlikely that the increased precision would result in consistently increased success rates across studies with different raters and their own subjective assessments. However, the primary purpose behind the development of the hand pattern characterization method was not pattern type classification, but an objective quantification of individual patterns (i.e., TRT and NRT values) that could be statistically analyzed, which is unaffected by the uncertainty in the threshold selection.

CONCLUSIONS

This study identified the influence of both speed and grade on hand patterns during wheelchair propulsion. The results suggest that the specific goals and constraints of the propulsion task can significantly influence preferred hand pattern selection. While hand pattern parameters can provide insight into propulsion technique, current understanding of the advantages and disadvantages of different hand pattern types is centered on large-scale biomechanical measures (e.g., θ and cadence). Further work is needed to identify the relationships between hand patterns and upper extremity demand. These relationships could then be used to help design rehabilitation programs and wheeled mobility devices aimed at minimizing the development of overuse injuries and pain in manual wheelchair users.

Chapter 4: The Influence of Wheelchair Propulsion Hand Pattern on Upper Extremity Demand

INTRODUCTION

The manual wheelchair propulsion cycle can be divided into the contact phase, when mechanical power is delivered to the wheelchair via hand contact with the handrim, and the recovery phase, when the hand is repositioned in preparation for the next cycle (e.g., Kwarciak et al., 2009). During the contact phase, the hand is restricted to the arc of the handrim. However, during the recovery phase, the hand is much less constrained and can follow a number of different paths. The resulting hand patterns (i.e., full-cycle hand paths) are frequently classified into four distinct hand pattern types based on the shape of their projection onto the plane of the handrim: arcing (AR), single loop (SL), double loop (DL) and semi-circular (SC) (Fig. 4.1, e.g., Boninger et al., 2002). The hand pattern is a clinically visible indicator that can provide insight into an individual's propulsion technique due to the close relationship between the movement of the hand and propulsion mechanics (e.g., Shimada et al., 1998).

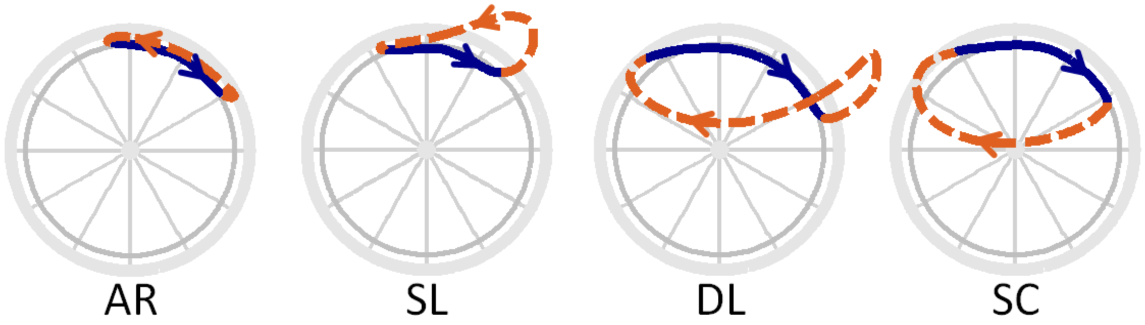

Figure 4.1: Hand pattern definitions. The four hand pattern types are arcing (AR), single loop (SL), double loop (DL) and semi-circular (SC). The solid line denotes the contact phase, while the dashed line denotes the recovery phase. The arrows indicate the direction of hand motion and the direction of wheelchair propulsion is to the right.

Previous investigations have attempted to ascertain whether the choice of hand pattern may influence the likelihood of developing upper extremity pain and injury (e.g., Boninger et al., 2002; de Groot et al., 2004; Kwarciak et al., 2012; Qi et al., 2014). Most of these studies have focused on the influence of hand pattern on large-scale biomechanical metrics that have been identified as risk factors (e.g., cadence, peak handrim force). Results suggest that SC produces lower cadence, larger contact percentages, larger contact angles, longer push distances and lower peak forces (e.g., Boninger et al., 2002; Kwarciak et al., 2012; Qi et al., 2014). SC may also produce lower joint accelerations (Shimada et al., 1998) and result in a clearer separation between contact and recovery muscle activity timing (Qi et al., 2014). As a result, current clinical guidelines recommend the use of SC, citing many of these potentially advantageous biomechanics (PVACSCM, 2005).

However, other hand patterns may have favorable characteristics as well. A recent study found that DL is associated with an increased contact angle, decreased cadence and decreased braking moment (Kwarciak et al., 2012), leading those investigators to recommend the use of this hand pattern. DL and AR have also been shown to have the lowest integrated electromyography (iEMG) values (Kwarciak et al., 2012). In addition, AR may be a more metabolically efficient hand pattern than SC (de Groot et al., 2004).

While it is valuable to understand the influence of hand pattern on large-scale biomechanical metrics (e.g., cadence, contact angle), it would also be useful to understand the influence of hand pattern on more direct measures of upper extremity demand (e.g., muscle power and stress). While the use of electromyographic (EMG) data can provide insight into the timing of individual muscle activity, the complex nonlinear relationships between muscle excitation signals and individual muscle force and power complicates the analyses and limits the conclusions that can be drawn from EMG data. In contrast, forward dynamics modeling and simulation techniques can provide a powerful framework for examining the biomechanics of a task at the individual muscle level (e.g., Erdemir et al., 2007). Therefore, the purpose of this study was to use musculoskeletal modeling and forward dynamics simulations to investigate the four distinct hand pattern types commonly observed in manual wheelchair propulsion and identify the influence of hand pattern on upper extremity demand (i.e., muscle power and stress). These results can then be applied to the design of rehabilitation programs and wheeled mobility devices aimed at limiting the development of overuse injuries and pain in individuals that use manual wheelchairs.

METHODS

Musculoskeletal model

An upper extremity musculoskeletal model and dynamic optimization framework that have been previously described in detail (e.g., Rankin et al., 2010; Rankin et al., 2011) were used in this study to generate forward dynamics simulations of manual wheelchair propulsion. The musculoskeletal model was based on the work of Holzbaur et al. (2005) and developed using SIMM (Musculographics, Inc., Santa Rosa, CA, USA). The model had six rotational degrees-of-freedom and included segments representing the trunk and right upper arm, forearm and hand. In addition to trunk lean, elbow flexion-extension and forearm pronation-supination, there were three degrees-of-freedom at the shoulder: plane-of-elevation, elevation angle and internal-external rotation (thoracohumeral angles). Scapulohumeral rhythm was defined using regression equations based on cadaver data (de Groot and Brand, 2001). Full-cycle trunk lean and contact-phase hand translations were prescribed based on experimentally-collected kinematic data. The dynamic equations-of-motion were generated using SD/FAST (Parametric Technology Corp., Needham, MA, USA). The major upper extremity muscles crossing the shoulder and elbow joints were represented by 26 Hill-type musculotendon actuators (e.g., Slowik and Neptune, 2013), governed by intrinsic muscle force-length-velocity and tendon force-strain relationships. Each actuator received a distinct excitation signal except the three latissimus dorsi actuators, the two sternocostal pectoralis major actuators, and the two actuators representing the lateral triceps and anconeus. Muscles within each of these groups received the same excitation signal. Muscle excitation-activation dynamics were modeled using a first order differential equation (Raasch et al., 1997) with muscle-specific activation and deactivation time constants (Happee and van der Helm, 1995; Winters and Stark, 1988). The musculotendon lengths and moment arms were calculated using polynomial regression equations (Rankin and Neptune, 2012), and the product of each muscle moment arm and force was applied at the joint as a muscle moment. Passive torques were applied at the joints to represent ligaments and other passive joint structures that limit extreme joint positions (Davy and Audu, 1987).

Simulation and optimization framework

Each muscle excitation pattern was generated using a bimodal pattern defined by six parameters (e.g., Hall et al., 2011), resulting in a total of 132 optimization parameters. For each hand pattern type, the excitation parameters that produced a simulation that best emulated hand pattern subgroup-averaged experimental propulsion data (i.e., joint angle and 3D handrim force profiles; see *Experimental data* below) were identified using a simulated annealing optimization algorithm (Goffe et al., 1994) and an optimal tracking cost function (Neptune et al., 2001). To prevent excess co-contraction, an additional term was included in the cost function that minimized the muscle stress squared. Average power delivered to the handrim was kept constant (6 W) across simulations to better enable comparisons.

Experimental data

As part of a previous study (see Chapter 3), experimental data was collected from 170 individuals with complete motor paraplegia while they propelled their wheelchair at a self-selected speed on a stationary ergometer that simulated level propulsion over a tile surface (e.g., Raina et al., 2012). Subjects were allowed to acclimate until they felt comfortable, and a ten-second trial was recorded following at least 30 seconds of propulsion to ensure near steady-state propulsion. Trunk, right side upper extremity and wheel kinematics were collected using a 4-scanner CODA motion analysis system (Charnwood Dynamics Ltd., Leicestershire, UK) with 15 active markers placed on landmarks on the body and right wheel (e.g., Lighthall-Haubert et al., 2009). Three-dimensional handrim kinetics were measured using an instrumented wheel (SmartWheel; Three Rivers Holdings, Mesa, AZ, USA).

Kinematic and kinetic data were low-pass filtered using a fourth-order zero-lag Butterworth filter with cutoff frequencies of 8 Hz and 10 Hz, respectively, in Visual3D (C-Motion, Inc., Germantown, MD, USA). Contact and recovery phases were delineated using a resultant handrim force threshold of 5 N. Contact and recovery-phase data for each cycle were time-normalized and averaged across propulsion cycles within each subject. A previously-described method (Rao et al., 1996) was used to locate the third metacarpophalangeal joint center (MCP3), and the hand pattern was defined as the average MCP3 path projected onto the plane of the handrim (e.g., Fig. 4.1). Hand patterns were characterized using a set of objective, quantitative parameters (see Chapter 3 for details), and this characterization was used to identify four groups of subjects that used each of the four hand pattern types. From these groups, twenty male subjects (five of each hand pattern type) were then identified such that differences between pattern-type group averages for propulsion speed, mass, height, age and time from injury were minimized (Table 4.1). Mean subject data were then averaged across subjects within each pattern type group to create group-averaged hand pattern, joint angle and 3D handrim force profiles.

Table 4.1: Mean values of subject and propulsion characteristics for the four hand pattern types: arcing (AR), single loop (SL), double loop (DL) and semi-circular (SC).

Subject characteristics					Propulsion characteristics			
Hand pattern type	Age (yr)	Time from injury (yr)	Height (m)	Mass (kg)	Propulsion speed (m/s)	Cycle Time (s)	Contact Percentage (%)	Contact Angle (°)
AR	39.4	9.3	1.77	77.3	0.97	0.95	45.8	73.2
SL	39.2	14.2	1.80	77.6	1.02	1.02	36.4	71.7
DL	32.7	12.9	1.73	81.1	0.97	1.43	34.7	86.6
SC	35.0	10.0	1.77	79.9	0.99	1.34	44.9	92.9
All 20 subjects	36.6	11.6	1.77	79.0	0.99	1.19	40.5	81.1

Analysis

Three consecutive propulsion cycles were simulated for each hand pattern type, and the third cycle was analyzed to allow the simulation to reach steady-state. To assess how well each simulation tracked the experimental data, root-mean-square (RMS) differences between simulated and experimental data were calculated. Individual muscle data at each time step were then obtained from the simulations and used to calculate a set of direct measures of upper extremity demand. Instantaneous muscle stress was calculated by dividing the instantaneous muscle force by the physiological cross-sectional area of the muscle, and time-averaged within the contact and recovery phases, as well as across the full cycle. The full-cycle values were also decomposed into contributions during the contact and recovery phases, enabling additional comparisons across simulations that account for the differences in contact percentages.

Instantaneous muscle mechanical power was computed as the product of the instantaneous muscle force and velocity. Mean positive and negative powers for the contact phase, recovery phase and full cycle were calculated by time-averaging the instantaneous positive and negative powers, respectively. Mean total (absolute value sum) and net (linear sum) powers were subsequently calculated. The full-cycle values were again decomposed into contributions from the contact and recovery phases. The individual muscle data from the 26 muscles were combined into 13 analysis groups based on a combination of anatomical location and muscle function (Table 4.2), with power data summed and stress data averaged within each muscle group. Overall measures of upper extremity demand were then calculated as the summed power and average stress of all 26 muscles.

Table 4.2: Upper extremity muscle and group definitions.

Muscle Group	Muscle	Compartment	Abbreviation
ADelt	Deltoid	Anterior	DELT1
MDelt		Middle	DELT2
PDelt		Posterior	DELT3
Subsc	Subscapularis	----------------------	SUBSC
Supra	Supraspinatus	----------------------	SUPSP
Infra	Infraspinatus	----------------------	INFSP
	Teres Minor	----------------------	TMIN
PecMaj	Pectoralis major	Clavicular head	PECM1
		Sternocostal head - sternum	PECM2
		Sternocostal head - ribs	PECM3
	Coracobrachialis	----------------------	CORB
Lat	Latissimus dorsi	Thoracic	LAT1
		Lumbar	LAT2
		Iliac	LAT3
	Teres Major	----------------------	TMAJ
Tri	Triceps brachii	Long head	TRIlong
		Medial head	TRImed
		Lateral head	TRIlat
	Anconeus	----------------------	ANC
Bra	Brachialis	----------------------	BRA
	Brachioradialis	----------------------	BRD
Bic	Biceps brachii	Long head	BIClong
		Short head	BICshort
Sup	Supinator	----------------------	SUP
Pro	Pronator teres	----------------------	PT
	Pronator quadratus	----------------------	PQ

RESULTS

Experimental data tracking

All four simulations resulted in propulsion mechanics that closely emulated the corresponding hand pattern type experimental joint kinematics and handrim forces (Table 4.3, Appendix C), with average RMS differences of 2.1° and 1.7 N, respectively. All RMS differences were well within one standard deviation of the experimental data.

Table 4.3: Root-mean-square differences between simulated and experimental joint kinematics and handrim forces for the four hand pattern types: arcing (AR), single loop (SL), double loop (DL) and semi-circular (SC). For comparison, one standard deviation of the experimental data is provided in parentheses to indicate inter-subject variability.

Tracking differences (simulation vs. experimental)		Simulations			
		AR	SL	DL	SC
Joint kinematics (degrees)	Elevation plane	1.2 (10.3)	1.8 (19.1)	2.3 (13.3)	3.3 (12.4)
	Elevation angle	0.7 (5.3)	1.0 (7.3)	0.9 (6.4)	1.1 (8.2)
	Shoulder rotation	1.0 (23.6)	2.9 (32.4)	2.3 (18.0)	9.2 (26.0)
	Elbow flexion	0.9 (18.5)	0.7 (8.4)	0.8 (8.6)	0.8 (12.9)
	Pronation/supination	4.2 (23.6)	1.7 (12.0)	1.2 (11.6)	4.3 (22.5)
	All joints	1.6 (16.3)	1.6 (15.8)	1.5 (11.6)	3.7 (16.4)
Handrim forces (N)	Tangential	0.9 (5.2)	3.2 (3.8)	1.0 (6.2)	2.3 (5.5)
	Radial	3.3 (11.4)	0.8 (5.8)	1.9 (4.8)	2.0 (10.1)
	Lateral	0.7 (5.0)	1.7 (3.0)	1.7 (3.8)	1.3 (4.1)
	All forces	1.6 (7.2)	1.9 (4.2)	1.5 (4.9)	1.9 (6.6)

Overall muscle power

Full-cycle net muscle power was similar across hand pattern types, with the lowest power generated with SC and the highest power generated with SL (7.0 W vs. 7.6 W, Fig. 4.2). While contact-phase net muscle power was larger for SL and DL compared to AR and SC (14.6 W and 15.2 W vs. 11.4 W and 11.3 W, respectively), contact-phase contributions to the full-cycle net muscle power were similar across all hand pattern types (range: 5.1-5.3 W). There were larger differences in the total muscle power, with DL requiring the least full-cycle total power and AR requiring the most (22.5 W vs. 26.5 W). The contact and recovery phases exhibited comparable amounts of negative (eccentric, active lengthening) muscle power. However, the contact phase consistently exhibited greater amounts of positive (concentric, active shortening) muscle power than the recovery phase. As a result, the contact phase also consistently exhibited larger total and net muscle power than the recovery phase, although the net power was positive during both phases for all hand pattern types. While the recovery-phase contributions accounted for only a small portion of the full-cycle net power (26-30%), recovery-phase contributions accounted for a much larger portion of the full-cycle total power (37-57%).

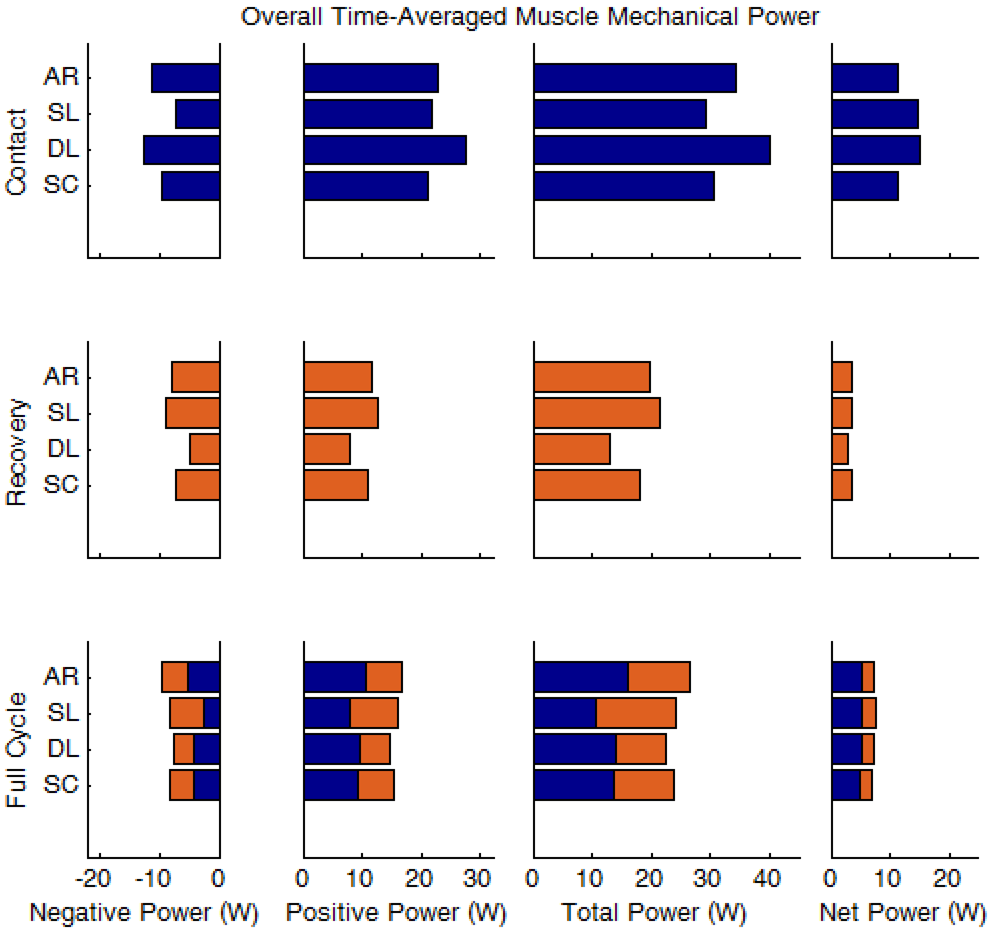

Figure 4.2: Overall levels of time-averaged negative, positive, total and net power (summed across all muscles) for the four hand pattern types: arcing (AR), single loop (SL), double loop (DL) and semi-circular (SC). The top, middle and bottom rows correspond to the contact phase, recovery phase and full cycle respectively. Contact and recovery-phase contributions are colored blue and orange respectively.

Individual muscle power

For all hand pattern types, ADelt and Tri were among the primary contributors to the full-cycle total and net muscle power (Fig. 4.3). The majority of this power was generated during the contact phase. Other large contributors to the full-cycle total muscle power included PDelt, Lat and Bra with AR; MDelt and Bra with SL; and Lat with SC.

Comparisons between hand pattern types revealed a few differences in individual muscle power generation. Full-cycle Lat total power generation was increased with AR. Full-cycle MDelt total power generation was increased with SL, but full-cycle ADelt total power generation was decreased. Contact-phase ADelt and Tri total power generation was increased with DL, but contact-phase PecMaj and recovery-phase Lat total power generation was decreased. Total power generation was not notably higher or lower for any individual muscle group with SC relative to the other hand pattern types.

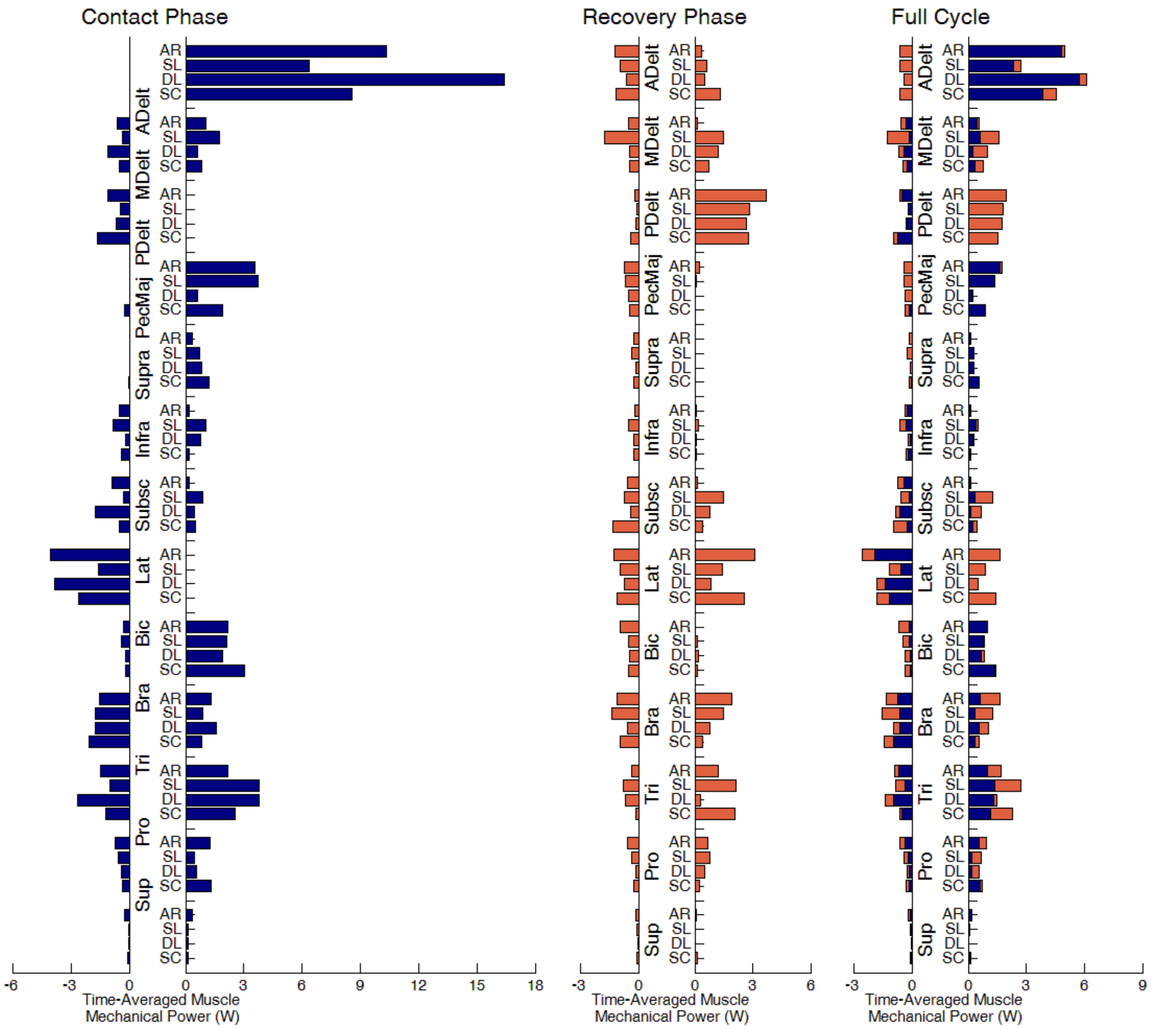

Figure 4.3: Time-averaged positive and negative power generated by each muscle group for the four hand pattern types: arcing (AR), single loop (SL), double loop (DL) and semi-circular (SC). The left, center and right plots correspond to the contact phase, recovery phase and full cycle respectively. Contact and recovery-phase contributions are colored blue and orange respectively.

Overall muscle stress

Full-cycle muscle stress was lowest with DL and highest with AR (31.5 kPa vs. 43.0 kPa, Fig 4.4). Contact-phase stress was lowest with SC and highest with SL (39.4 kPa vs. 50.7 kPa). However, contact-phase contribution to the full-cycle muscle stress was lowest with DL and highest with AR (14.7 kPa vs. 22.6 kPa). Recovery-phase stress was lowest with DL and highest with AR (25.8 kPa vs. 38.0 kPa). While recovery-phase contribution to the full-cycle muscle stress was also lowest with DL, it was highest with SL (16.8 kPa vs. 21.9 kPa). Recovery-phase muscle stress was consistently lower than contact-phase muscle stress, with percent differences between contact and recovery values ranging from 5% (SC) to 48% (DL). However, the recovery phase consistently contributed approximately half of the full-cycle muscle stress (46-53%) due to the longer duration of this phase.

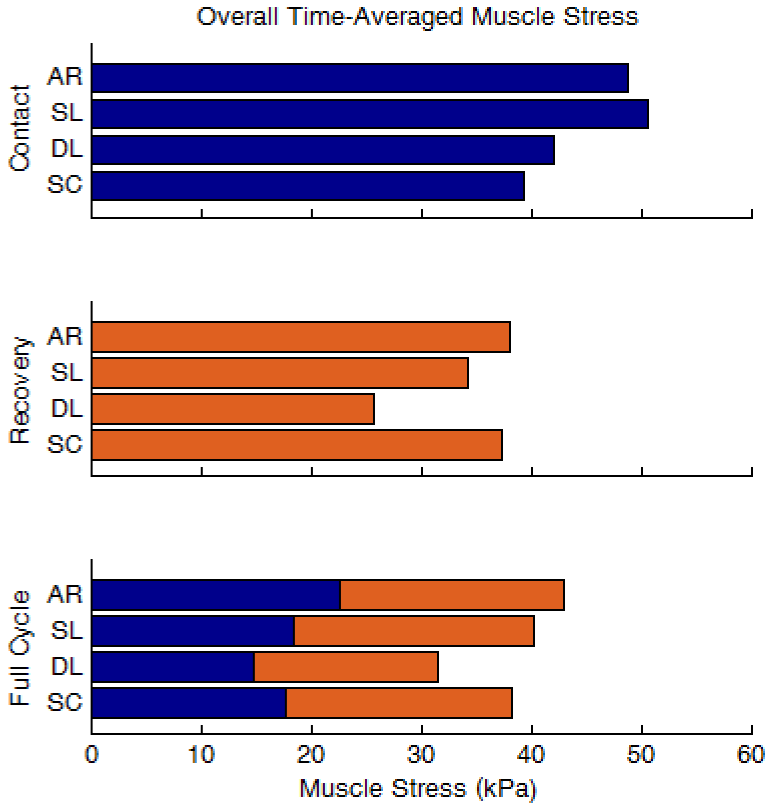

Figure 4.4: Overall levels of time-averaged muscle stress (averaged across all muscles) for the four hand pattern types: arcing (AR), single loop (SL), double loop (DL) and semi-circular (SC). The top, middle and bottom rows correspond to the contact phase, recovery phase and full cycle respectively. Contact and recovery-phase contributions are colored blue and orange respectively.

Individual muscle stress

For all hand pattern types, Subsc, MDelt, PDelt and ADelt were among the muscle groups that experienced the highest full-cycle stress levels (Fig 4.5). The majority of the full-cycle ADelt stress was attributed to high stress during the contact phase, while the majority of the full-cycle PDelt and Subsc stresses was attributed to the high stresses during the recovery phase. The high full-cycle MDelt stress was attributed to high stresses during both phases. Other high full-cycle muscle stress values occurred in Lat and Sup with AR; Infra, Bra, Pro and Sup with SL; and Bra and Sup with SC.

Comparisons between hand pattern types revealed a number of differences in individual muscle stress levels. AR experienced relatively high full-cycle MDelt stress due to contributions during both phases. AR also experienced high contact-phase stress from Sup and high recovery-phase stress from Lat. However, AR experienced low full-cycle stress from Subsc compared to other hand pattern types, primarily related to low stress during the recovery phase. SL experienced high full-cycle Infra stress, primarily related to the high stress during the contact phase. SL also experienced high full-cycle Subsc stress, primarily related to high stress during the recovery phase. In addition, SL experienced high contact-phase Pro stress. However, SL experienced low full-cycle ADelt stress, primarily related to low stress during the contact phase. SL also experienced low full-cycle PDelt stress due to low stresses during both phases. In addition, SL experienced low contact-phase Lat stress. DL experienced high contact-phase ADelt and Lat stresses, but low full-cycle MDelt stress, primarily related to low stress during the contact phase. DL also experienced low full-cycle Sup stress (due to low stress during both phases), low contact-phase PecMaj stress and low recovery-phase Lat stress. SC only experienced high recovery-phase Sup stress.

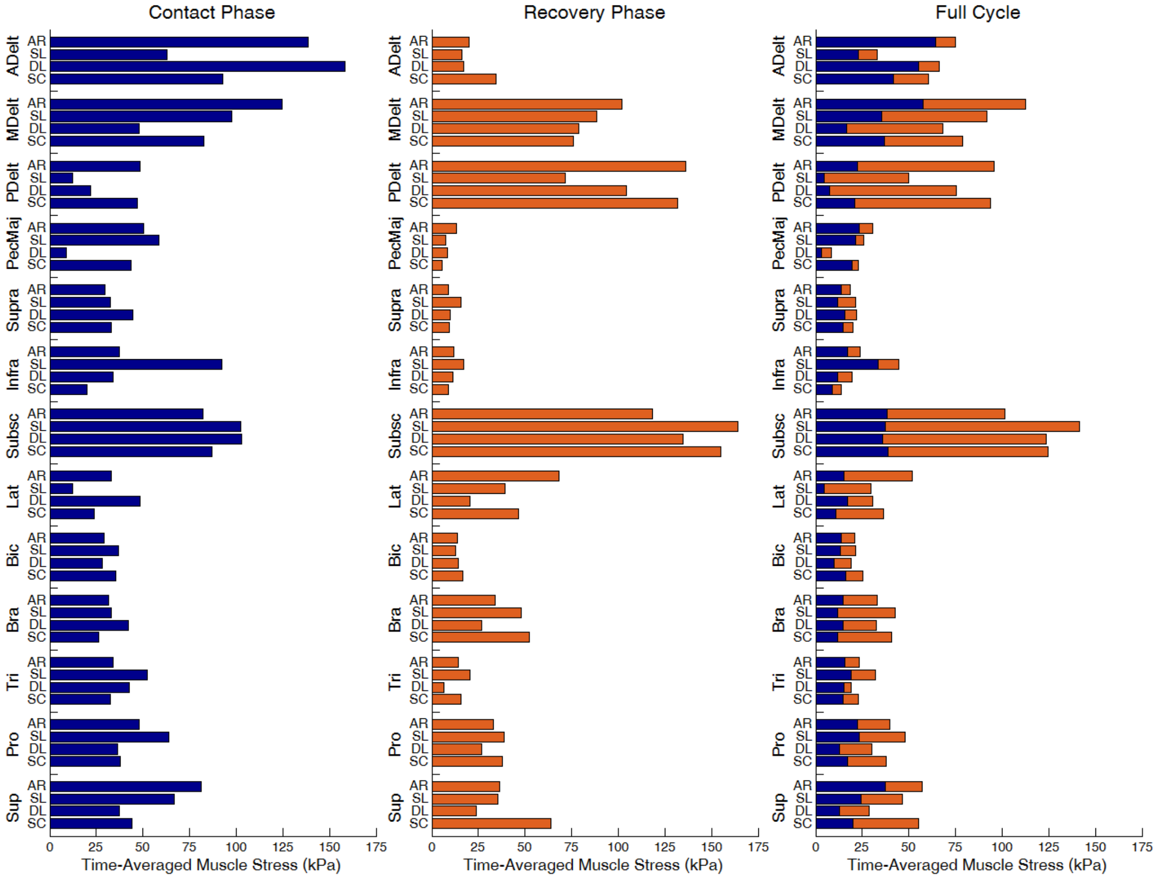

Figure 4.5: Time-averaged individual muscle stress values for the four hand pattern types: arcing (AR), single loop (SL), double loop (DL) and semi-circular (SC). The left, center and right plots correspond to the contact phase, recovery phase and full cycle respectively. Contact and recovery-phase contributions are colored blue and orange respectively.

DISCUSSION

The purpose of this study was to identify the influence of wheelchair propulsion hand pattern on upper extremity demand by developing forward dynamics simulations of the four distinct hand pattern types. While there were many similarities between the hand pattern types, there were also some key differences.

Propulsion characteristics

While the subjects were chosen such that the four hand pattern subgroups would have similar propulsion speeds (Table 4.1), there were differences in other propulsion characteristics that influenced the individual muscle power and stress quantities. SC had a long cycle time, large contact percentage and large contact angle (Table 4.1), which have all previously been suggested as favorable characteristics (e.g., PVACSCM, 2005). DL had a long cycle time and large contact angle, but a small contact percentage. AR had a large contact percentage, but a short cycle time and small contact angle. SL had a short cycle time, small contact percentage and small contact angle, which have all been suggested as unfavorable characteristics. The relative levels of these spatiotemporal variables across hand pattern types were consistent with previous studies (Boninger et al., 2002; Kwarciak et al., 2012), providing confirmation that the selected subjects appropriately represented the different hand pattern types.

AR

Of the four hand pattern types, AR experienced the highest full-cycle levels of overall upper extremity demand (i.e., total muscle power and muscle stress). This was primarily due to AR having the highest contributions during the contact phase, derived from both high contact-phase demand levels and a large contact percentage. However, AR did have the lowest full-cycle Subsc stress, which may reduce the risk of fatigue and injury in this rotator cuff muscle. As Subsc plays a critical role in stabilizing the shoulder (e.g., Ward et al., 2006), this may also prevent more extensive injury.

SL

SL experienced the second highest full-cycle levels of overall upper extremity demand. SL exhibited the highest recovery-phase contributions to the total power, but lowest contact-phase contributions, leading to the second highest full-cycle average total power. SL also experienced the highest contact-phase stress. However, due to its small contact percentage, it experienced only the second highest contact-phase contribution to full-cycle stress which resulted in the second highest overall full-cycle stress. SL also experienced high Infra and Subsc stress, which could increase the risk of fatigue and injury in these rotator cuff muscles. As Infra and Subsc help stabilize the shoulder (e.g., Ward et al., 2006), this could lead to more extensive injury.

DL

Of the four hand pattern types, DL experienced the lowest full-cycle levels of overall upper extremity demand. This was primarily due to a combination of the lowest recovery-phase demand levels and the smallest contact percentage. Despite high demand levels during the contact phase, time spent in this phase was relatively short, and therefore DL actually experienced the lowest contact-phase contribution to the full-cycle average muscle stress and only the second highest contact-phase contribution to the full-cycle power. The low recovery-phase demand levels for DL are consistent with a previous study that suggested that using a low cadence technique could reduce muscle power requirements during the recovery phase (Rankin et al., 2012). One potential disadvantage of this technique is that it showed increased contact-phase ADelt power combined with decreased contact-phase PecMaj power, which could increase the risk of impingement (see Chapter 2).

SC

SC experienced the second lowest full-cycle levels of overall upper extremity demand. SC consistently exhibited the second lowest total power, for each individual phase and the full-cycle. In addition, SC experienced the lowest contact-phase stress, but the second-highest recovery-phase stress. This led to the smallest percent difference between contact and recovery-phase stresses among the four hand pattern types, suggesting that upper extremity demand is most evenly distributed throughout the cycle when using SC. There were no individual muscles that appeared to be at a greater risk of injury during SC in comparison with the other hand pattern types.

Study limitations

A potential limitation of this study is that the experimental data was not collected overground but on a calibrated wheelchair ergometer. Ergometers and other stationary propulsion simulators do not perfectly replicate overground propulsion. However, they result in similar propulsion mechanics while providing greater control over experimental variables in a laboratory setting (Koontz et al., 2012).

Another potential limitation is that the musculoskeletal model ignored the ability of the hand to produce a pure moment at the handrim because it did not include the wrist muscles and the wrist joint was fixed in the anatomical position. However, relative to shoulder and elbow moments, wrist moments are generally small (e.g., Robertson et al., 1996; Sabick et al., 2004). In addition, the effect of the fixed wrist on the other joints and the study conclusions was minimized by using a consistent model across all simulations and requiring optimized simulations to emulate the experimental joint kinematics and handrim forces.

A final potential limitation of this study is that it only examined level propulsion at a self-selected speed. Results of previous investigations suggest that people who use manual wheelchairs modify their hand pattern with changes in propulsion speed (Chapter 3; Boninger et al., 2002) and grade of incline (Chapter 3; Richter et al., 2007). Thus, future work should examine upper extremity demand during these other propulsion conditions.

CONCLUSIONS

DL and SC produced the most favorable levels of upper extremity demand. While DL exhibited the lowest full-cycle and recovery-phase demand values, it did require high levels of muscle power during its relatively short contact phase. The full-cycle demand levels of SC were the second-lowest, and the demand was more evenly distributed between the contact and recovery phases. The results of this study suggest that when propelling their wheelchairs at a self-selected speed on level ground, individuals should consider using either the DL or SC pattern.

Chapter 5: Conclusions

Manual wheelchair users are at an increased risk of developing upper extremity pain and injuries due to the considerable physical demand of wheelchair propulsion. An increased understanding of the relationships between muscle weakness, wheelchair propulsion technique and upper extremity demand may help reduce this risk. Therefore, the overall goal of this research was to add to the current understanding of these relationships through a combination of experimental and simulation analyses.

In Chapter 2, forward dynamics simulations of wheelchair propulsion were used to identify the influence of individual muscle weakness on upper extremity demand during manual wheelchair propulsion. The simulation results suggested that the upper extremity musculature is robust to weakness in individual muscle groups as other muscles were able to compensate and restore normal propulsion mechanics. The observed shifts in power between muscles demonstrated how the distribution of upper extremity demand can be modified without any discernable changes in propulsion technique. However, while the deltoid and rotator cuff muscles can produce moments to compensate for each other, shifts between these muscles may compromise glenohumeral stability and lead to impingement or other similar injuries. In addition, the rotator cuff muscles experienced many of the highest stress levels across simulations, further highlighting their susceptibility to fatigue and injury. These results suggest that rehabilitation programs should seek to strengthen the rotator cuff muscles and supporting muscles whose contributions do not increase the risk for impingement (i.e., the thoracohumeral depressors) as this may help reduce the risk of upper extremity injury in manual wheelchair users.

In Chapter 3, a set of objective quantitative parameters were developed to characterize kinematic hand patterns and identify the influence of propulsion condition (i.e., speed and grade of incline) on the hand patterns preferred by manual wheelchair users. Increased propulsion speed resulted in a shift away from under-rim hand patterns (DL and SC) while increased grade resulted in the hand remaining near the handrim throughout the cycle (e.g., AR). These results revealed that manual wheelchair users modify their hand patterns in response to different propulsion conditions encountered in daily activities, suggesting that it is unlikely that a single optimal propulsion pattern exists for all propulsion conditions. In addition, the hand pattern characterization method developed for this study has several advantages over previous methods. The method can be used not only to objectively classify hand patterns as one of the four commonly described pattern types but also to differentiate between patterns of the same type, which can be challenging using subjective methods. These quantitative parameters also enable improved statistical analyses and clearer illustrations of trends across conditions.

In Chapter 4, forward dynamics simulations of the four commonly observed hand pattern types were developed and used to determine the influence of hand pattern on upper extremity demand. The under-rim patterns, DL and SC, produced the most favorable levels of overall muscle stress and total muscle power. DL exhibited the lowest full-cycle and recovery-phase demand values but required high levels of muscle power during the relatively short contact phase. SC exhibited the second-lowest full-cycle levels of overall muscle stress and total muscle power, and demand was more evenly distributed between the contact and recovery phases. These results suggest that in order to decrease upper extremity demand, manual wheelchair users may want to use either the DL or SC pattern when propelling their wheelchairs at their self-selected speed on level ground.

Each of the studies addressed a research question exploring the relationships between muscle weakness, wheelchair propulsion technique and upper extremity demand. Together, the results of these studies have provided a scientific basis for designing rehabilitation and training programs aimed at reducing the prevalence of upper extremity injury and pain among manual wheelchair users.

Chapter 6: Future Work

The studies presented in this dissertation have provided insight into the relationships between muscle weakness, wheelchair propulsion technique and upper extremity demand. However, there are several opportunities for future work to build upon these results. For example, future studies could further investigate the interactions between propulsion condition, propulsion technique and upper extremity demand. While the results of Chapters 3 and 4 provide some insight into these interactions, the simulations in Chapter 4 only analyzed level propulsion at self-selected speed. Detailed analyses of simulations during other conditions (e.g., varied speed or grade of incline) would further the understanding of why and how individuals adjust their hand pattern.

Another area of future work involves using predictive simulations of wheelchair propulsion to investigate why a manual wheelchair user may select one hand pattern over another. Predictive simulations are not produced by tracking experimental data, but instead are generated by optimizing an objective function based on task performance, such as the minimization of metabolic cost (e.g., Erdemir et al., 2007). Predictive simulations can enable systematic examinations of the influence of propulsion variables such as cadence, contact percentage, contact angle, propulsion speed and power output on hand pattern and upper extremity demand. Compared to experimental methods, predictive simulations have the ability to isolate specific variables without the confounding effect of other variables changing simultaneously. For example, when an individual is prompted to modify one propulsion variable (e.g., via biofeedback), they usually modify other variables as well (e.g., Rankin et al., 2012). However, a set of predictive simulations could be generated in which the contact percentage is systematically modified while all other variables are held constant. Then, any resulting alterations to the hand pattern and/or the levels of upper extremity demand could be precisely attributed to the change in contact percentage, which cannot be done in an experimental study. Predictive simulations could also be used to examine the influence of different performance criteria (i.e., objective functions) on hand pattern. For example, hypothetically a minimization of metabolic cost could result in a DL pattern while a minimization of hand jerk (i.e., rate of change of the acceleration of the hand) could result in a SC pattern. Such an analysis would confirm the important role that the specific performance criterion plays in selecting a propulsion technique.

Another area of future work could be in the quantification of contact forces. While Chapters 2 and 4 focused on the influence of muscle weakness and propulsion technique on muscle stress and power, additional insights into injury mechanisms could be obtained from examinations of joint contact forces, which the current model is unable to provide. The current model uses regression equations to calculate musculotendon lengths and moment arms based on joint positions, and does not include information regarding the orientation of the individual muscle force vectors (Rankin and Neptune, 2012). Prior to this simplification, the model required a set of complex geometric surface constraints representing musculoskeletal structures to calculate muscle paths (Holzbaur et al., 2005), which increased computation time by a factor of over 100. However, it may be possible to re-enable joint contact force calculation without significantly increasing simulation time by developing another set of regression equations that include the force vector information, and thus could be an area of future work.

Future work should also address other limitations of the musculoskeletal model. For instance, the current model prescribes trunk and scapular motion and assumes a fixed wrist joint. As a result, the model is limited in the information that it can provide about these joints. The addition of relevant muscles at these joints could enable investigations into the functional roles of these muscles and their contributions to upper extremity demand. Finally, in order to represent handrim contact, the translations of the hand were prescribed during the contact phase in lieu of a more detailed contact model. Some potential studies would likely benefit from a more complex representation of the initial impact of the hand on the handrim and the ability of the hand to grip the handrim. However, it should be noted that as with any model, the benefits of any added complexity should be carefully considered in light of the additional computational cost and the research questions being asked. While the goals of the present studies would not have benefited from the added model complexity, these additions could open up additional avenues for future research. Therefore, while the studies presented in this dissertation provide additional insight into the relationships between muscle weakness, wheelchair propulsion technique and upper extremity demand, there is still much potential for future work.

Appendix A: Supplementary Material for Chapter 2

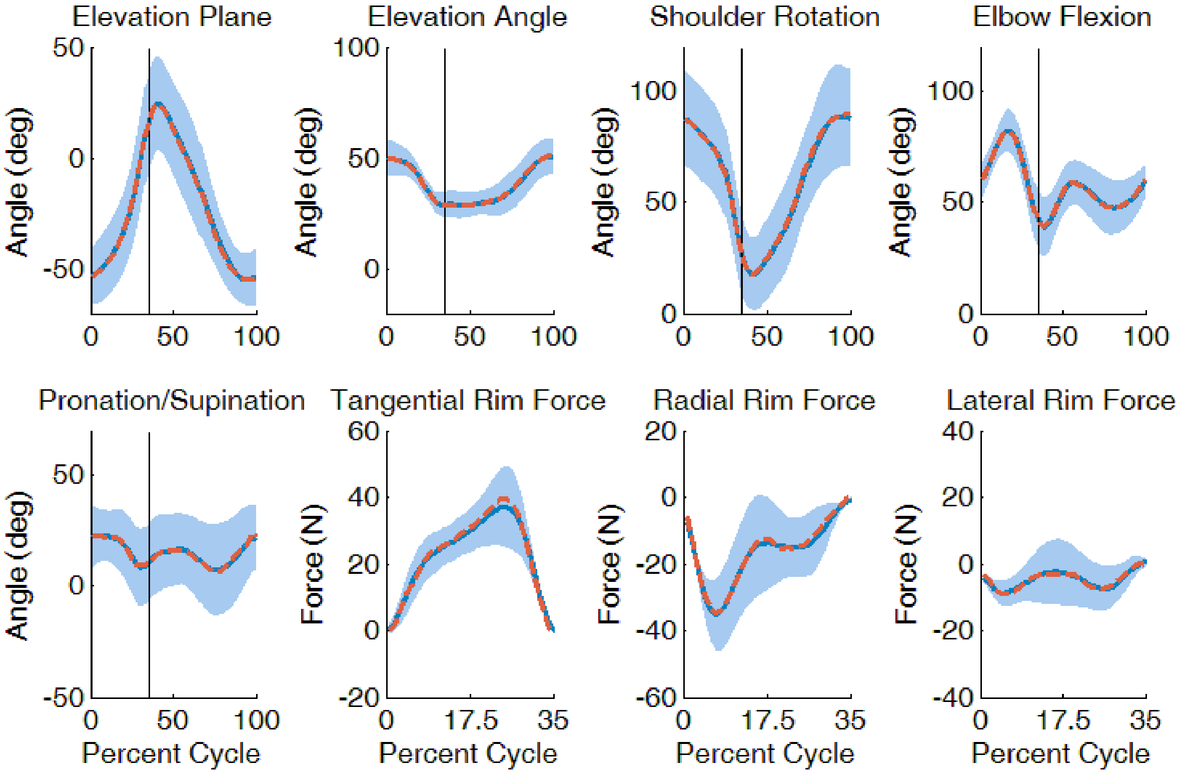

Figure A.1: Comparison between the ADelt-weakened simulation and group-averaged experimental mechanics. Experimental and simulation values are represented by solid and dashed lines, respectively. Shaded regions represent ± 1 SD of the experimental data. The joint angle plots depict the full cycle, with the end of the contact phase indicated with a vertical line. The handrim force plots only depict the contact phase, as values are approximately zero throughout the recovery phase.

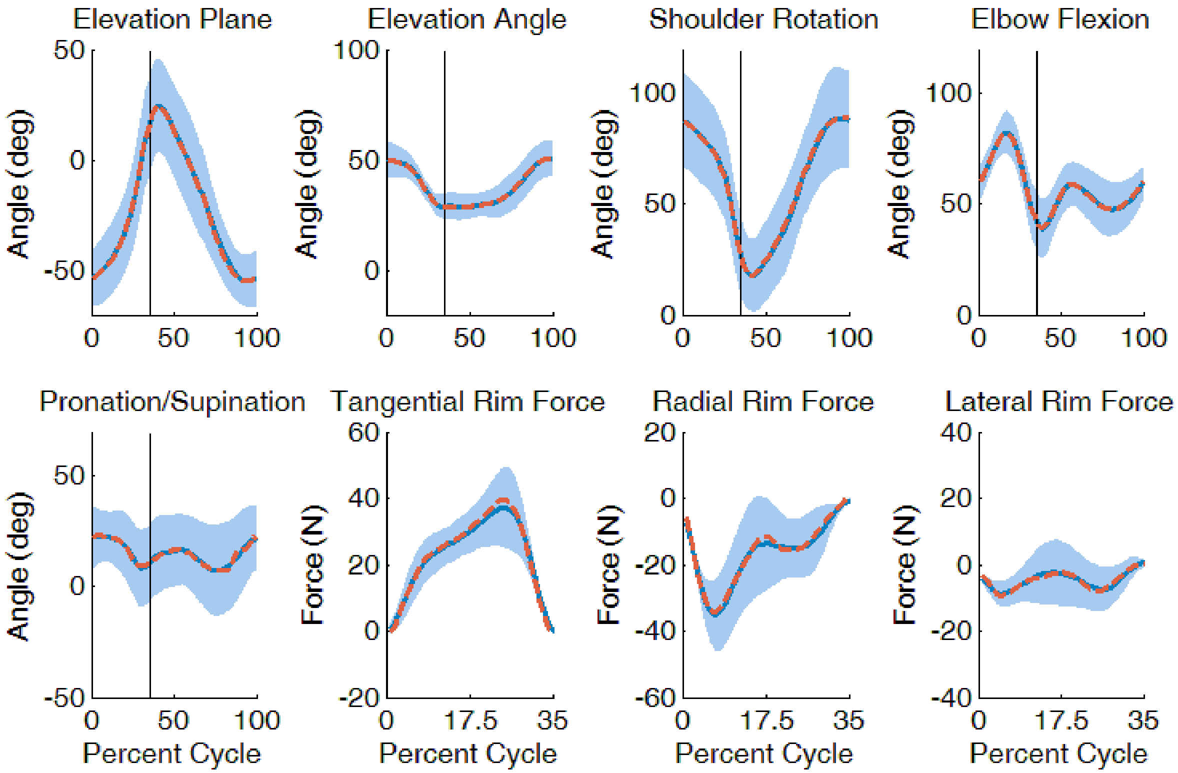

Figure A.2: Comparison between the MDelt-weakened simulation and group-averaged experimental mechanics. Experimental and simulation values are represented by solid and dashed lines, respectively. Shaded regions represent ± 1 SD of the experimental data. The joint angle plots depict the full cycle, with the end of the contact phase indicated with a vertical line. The handrim force plots only depict the contact phase, as values are approximately zero throughout the recovery phase.

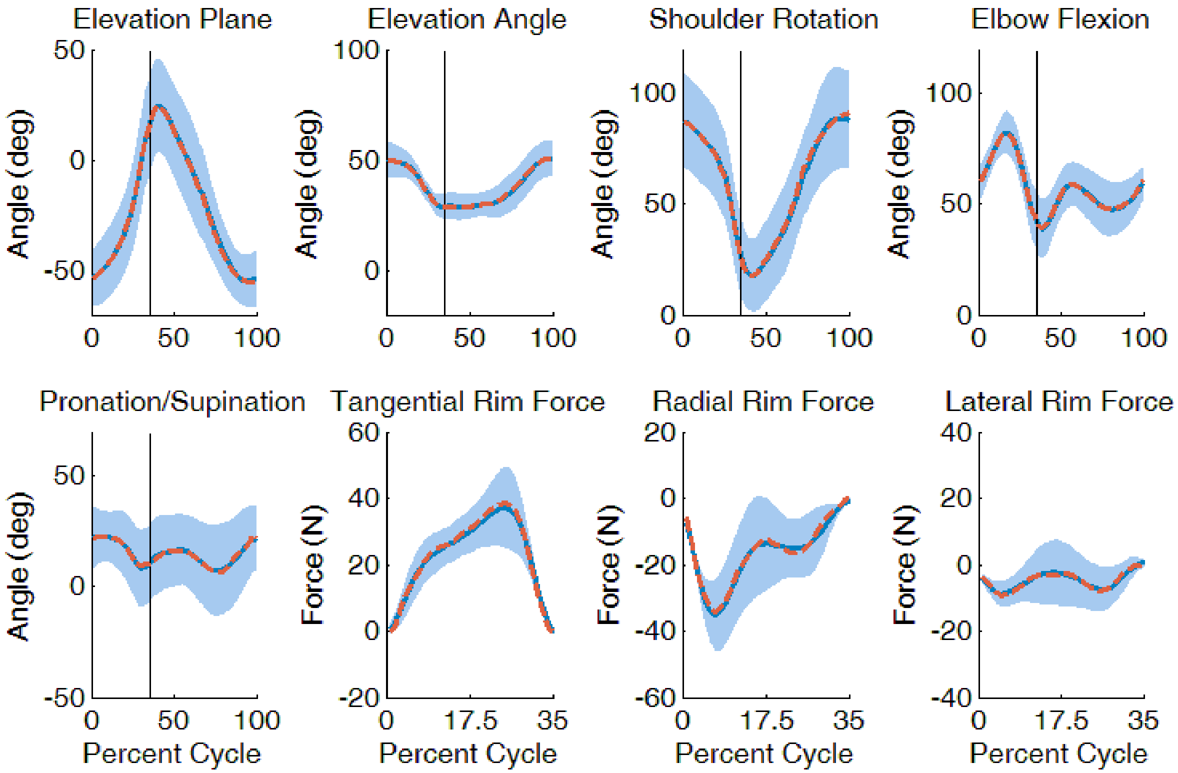

Figure A.3: Comparison between the Subsc-weakened simulation and group-averaged experimental mechanics. Experimental and simulation values are represented by solid and dashed lines, respectively. Shaded regions represent ± 1 SD of the experimental data. The joint angle plots depict the full cycle, with the end of the contact phase indicated with a vertical line. The handrim force plots only depict the contact phase, as values are approximately zero throughout the recovery phase.

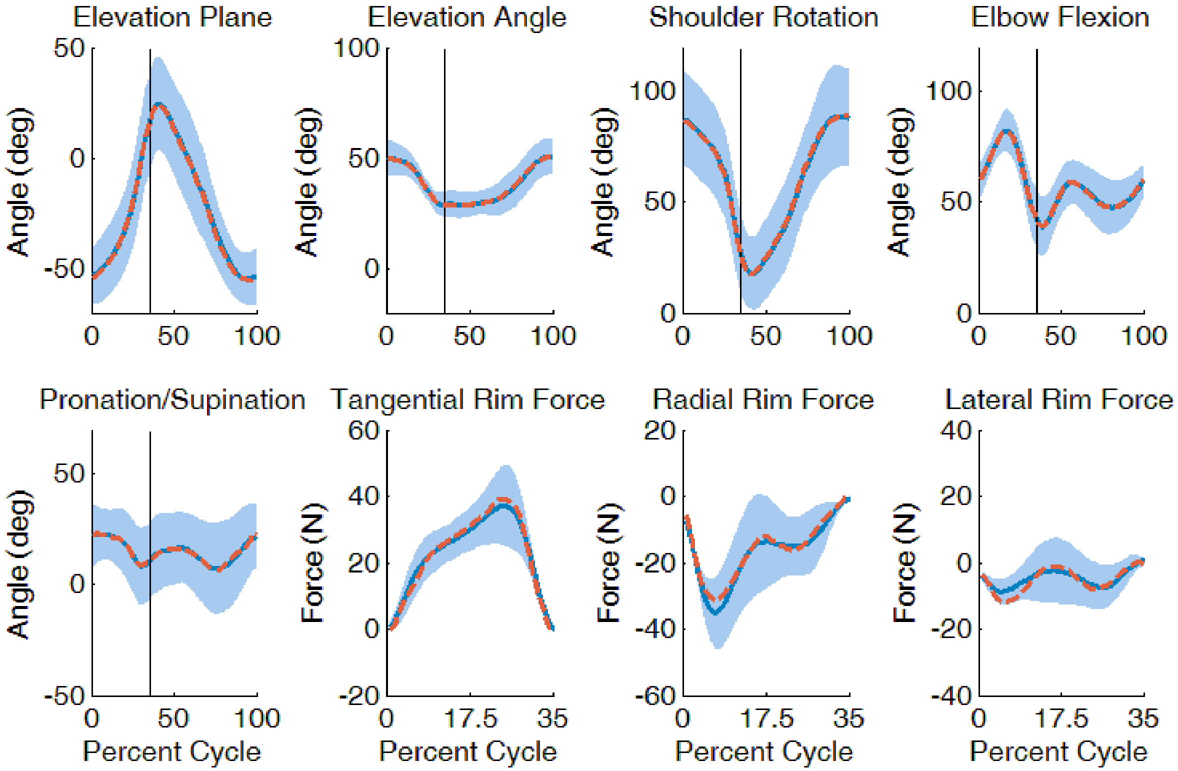

Figure A.4: Comparison between the Supra-weakened simulation and group-averaged experimental mechanics. Experimental and simulation values are represented by solid and dashed lines, respectively. Shaded regions represent ± 1 SD of the experimental data. The joint angle plots depict the full cycle, with the end of the contact phase indicated with a vertical line. The handrim force plots only depict the contact phase, as values are approximately zero throughout the recovery phase.

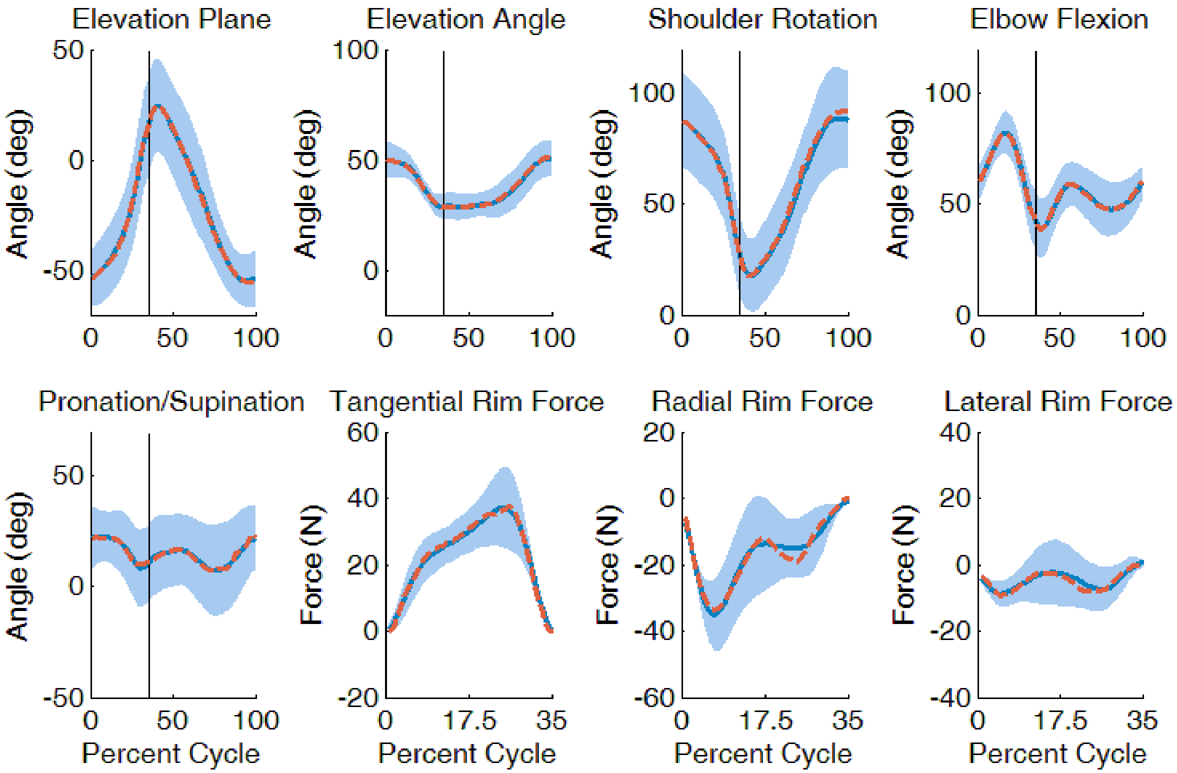

Figure A.5: Comparison between the Infra-weakened simulation and group-averaged experimental mechanics. Experimental and simulation values are represented by solid and dashed lines, respectively. Shaded regions represent ± 1 SD of the experimental data. The joint angle plots depict the full cycle, with the end of the contact phase indicated with a vertical line. The handrim force plots only depict the contact phase, as values are approximately zero throughout the recovery phase.

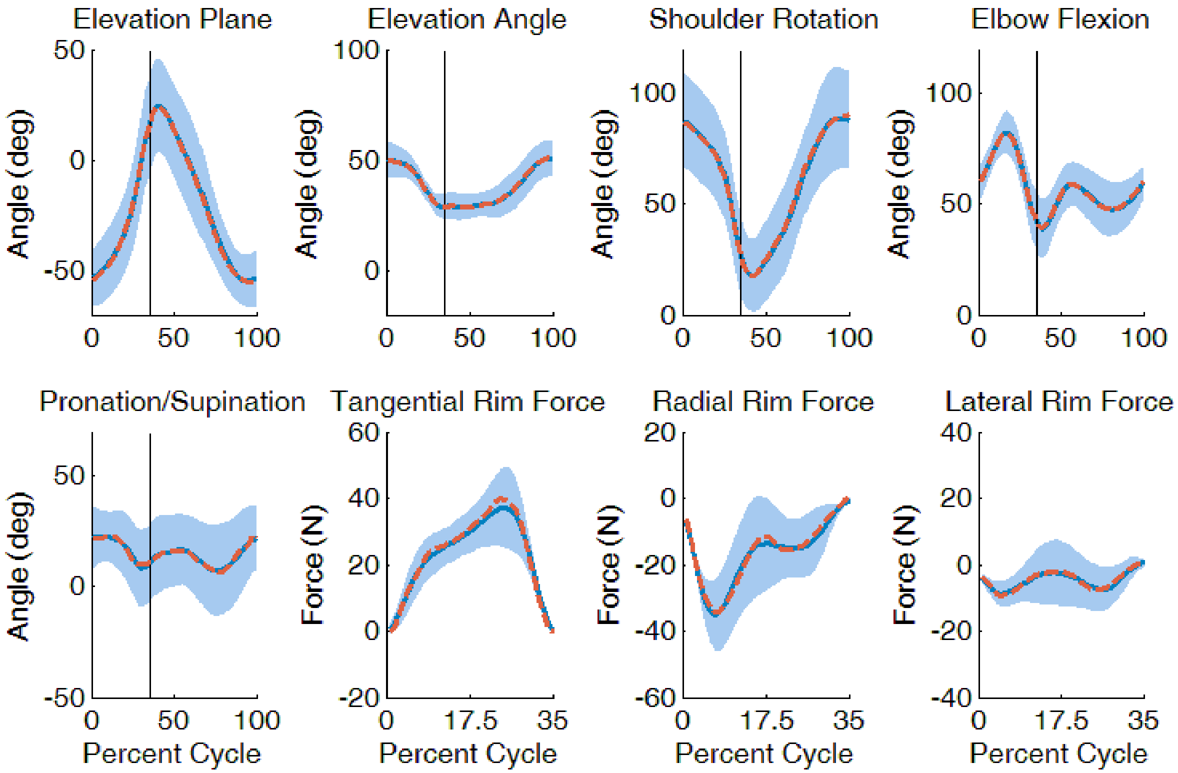

Figure A.6: Comparison between the PecMaj-weakened simulation and group-averaged experimental mechanics. Experimental and simulation values are represented by solid and dashed lines, respectively. Shaded regions represent ± 1 SD of the experimental data. The joint angle plots depict the full cycle, with the end of the contact phase indicated with a vertical line. The handrim force plots only depict the contact phase, as values are approximately zero throughout the recovery phase.

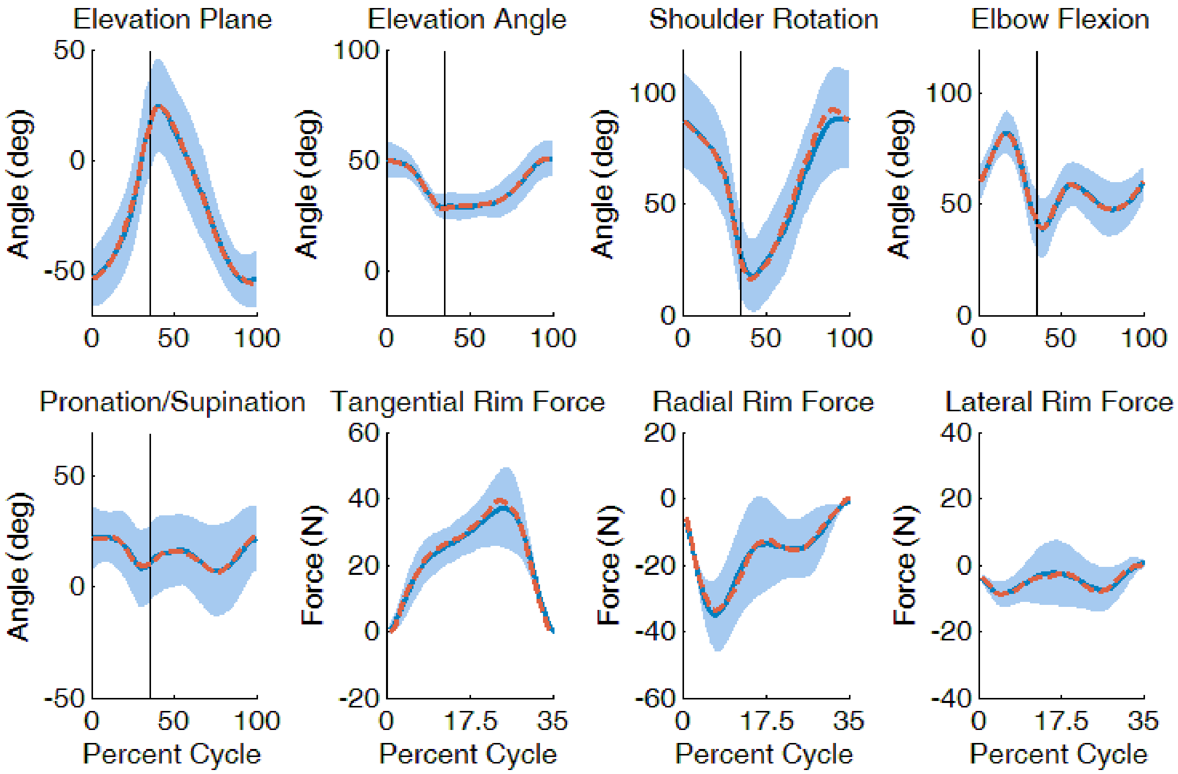

Figure A.7: Comparison between the Lat-weakened simulation and group-averaged experimental mechanics. Experimental and simulation values are represented by solid and dashed lines, respectively. Shaded regions represent ± 1 SD of the experimental data. The joint angle plots depict the full cycle, with the end of the contact phase indicated with a vertical line. The handrim force plots only depict the contact phase, as values are approximately zero throughout the recovery phase.

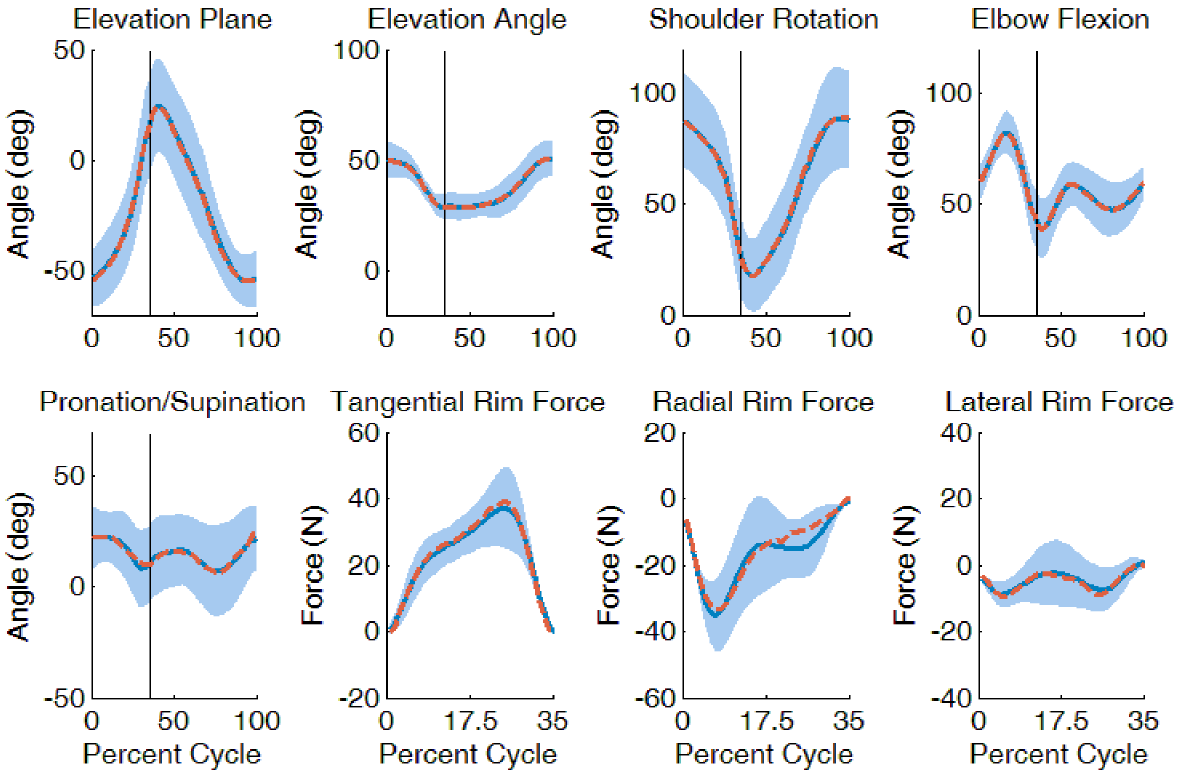

Figure A.8: Comparison between the Tri-weakened simulation and group-averaged experimental mechanics. Experimental and simulation values are represented by solid and dashed lines, respectively. Shaded regions represent ± 1 SD of the experimental data. The joint angle plots depict the full cycle, with the end of the contact phase indicated with a vertical line. The handrim force plots only depict the contact phase, as values are approximately zero throughout the recovery phase.

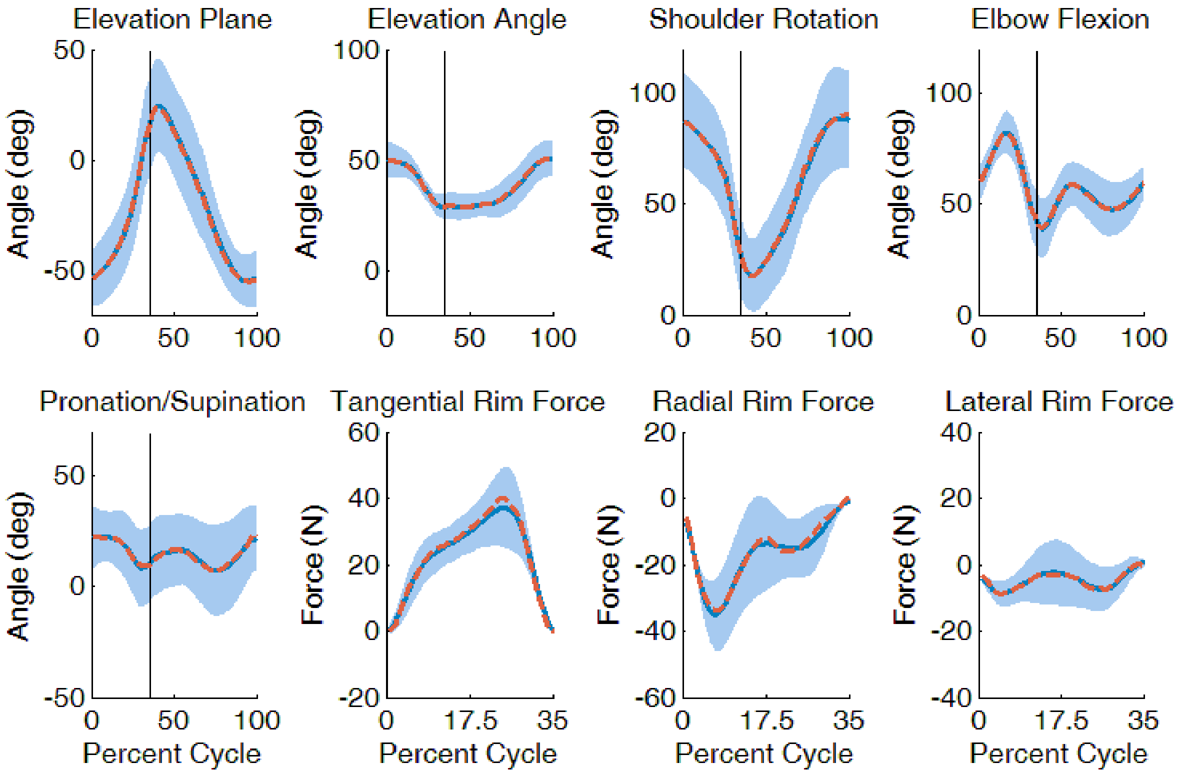

Figure A.9: Comparison between the Bra-weakened simulation and group-averaged experimental mechanics. Experimental and simulation values are represented by solid and dashed lines, respectively. Shaded regions represent ± 1 SD of the experimental data. The joint angle plots depict the full cycle, with the end of the contact phase indicated with a vertical line. The handrim force plots only depict the contact phase, as values are approximately zero throughout the recovery phase.

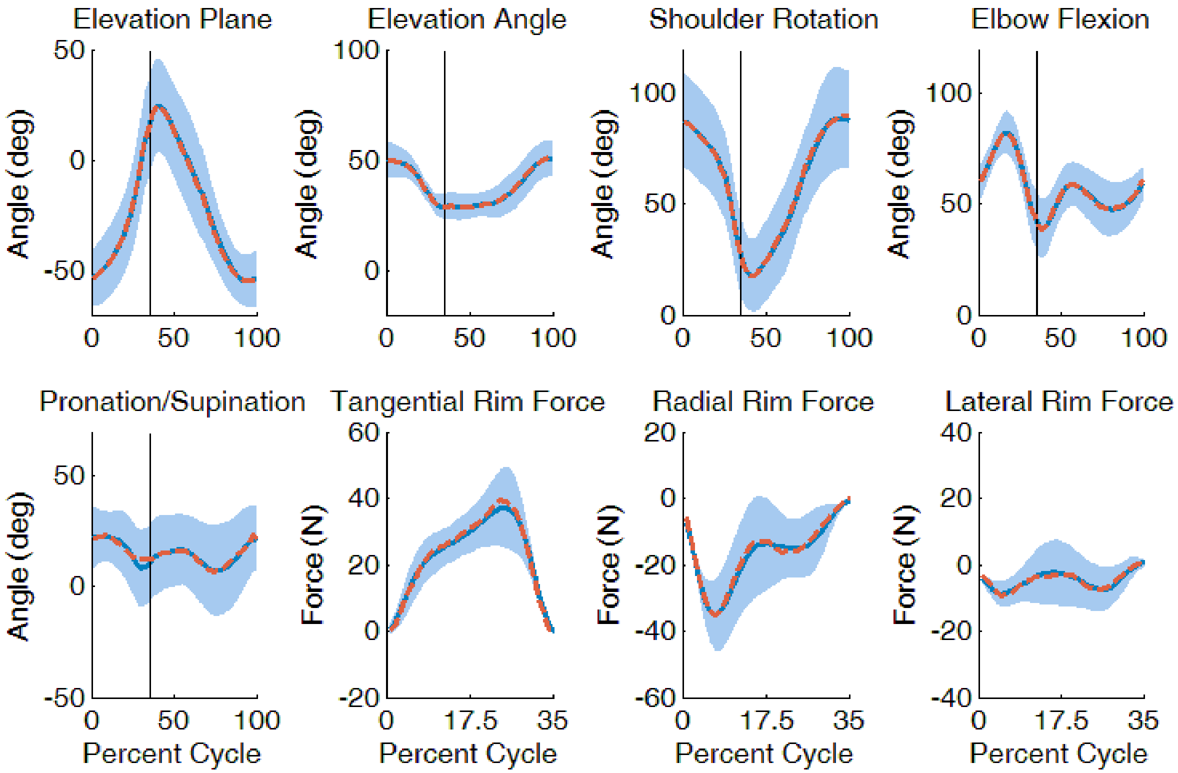

Figure A.10: Comparison between the Bic-weakened simulation and group-averaged experimental mechanics. Experimental and simulation values are represented by solid and dashed lines, respectively. Shaded regions represent ± 1 SD of the experimental data. The joint angle plots depict the full cycle, with the end of the contact phase indicated with a vertical line. The handrim force plots only depict the contact phase, as values are approximately zero throughout the recovery phase.

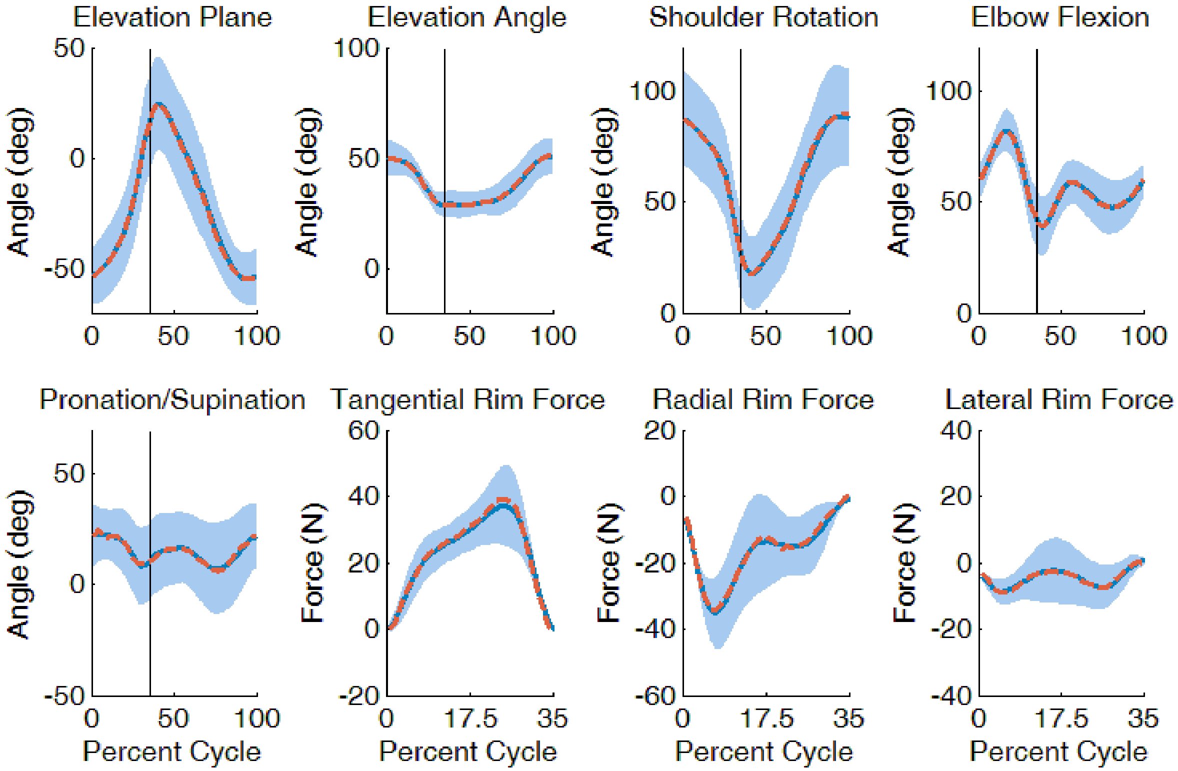

Figure A.11: Comparison between the Sup-weakened simulation and group-averaged experimental mechanics. Experimental and simulation values are represented by solid and dashed lines, respectively. Shaded regions represent ± 1 SD of the experimental data. The joint angle plots depict the full cycle, with the end of the contact phase indicated with a vertical line. The handrim force plots only depict the contact phase, as values are approximately zero throughout the recovery phase.

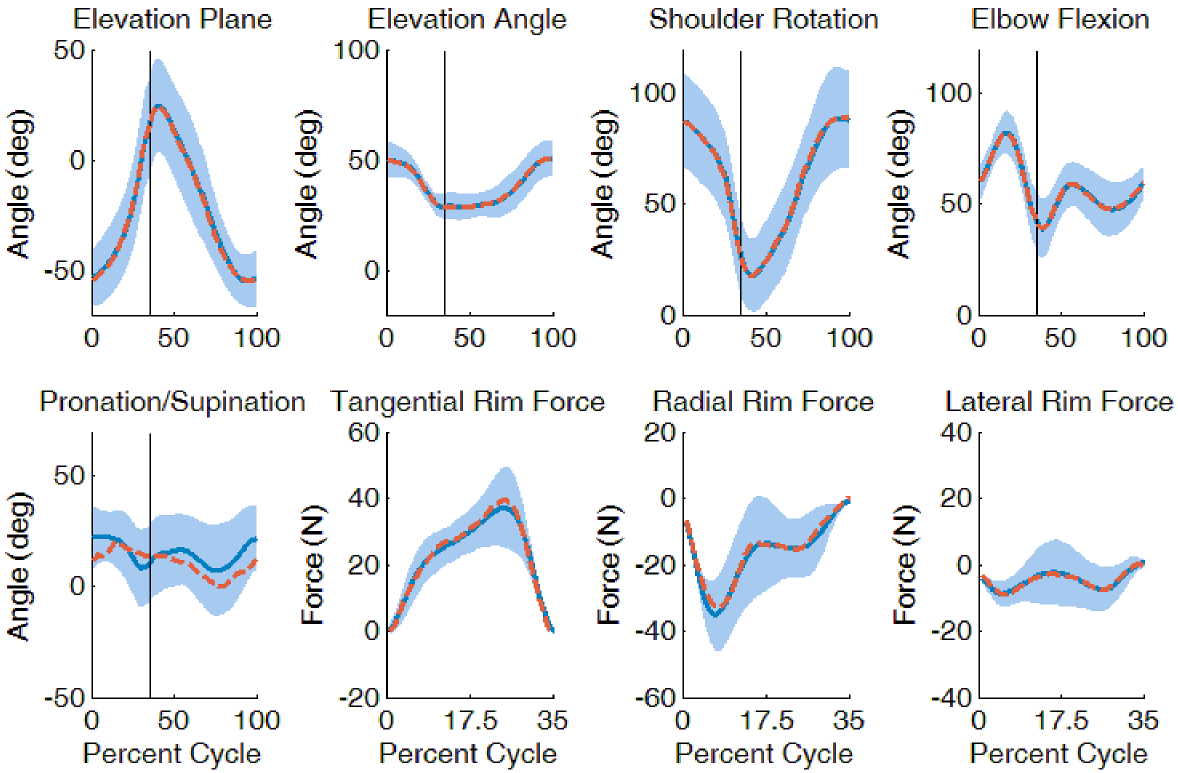

Figure A.12: Comparison between the Pro-weakened simulation and group-averaged experimental mechanics. Experimental and simulation values are represented by solid and dashed lines, respectively. Shaded regions represent ± 1 SD of the experimental data. The joint angle plots depict the full cycle, with the end of the contact phase indicated with a vertical line. The handrim force plots only depict the contact phase, as values are approximately zero throughout the recovery phase.

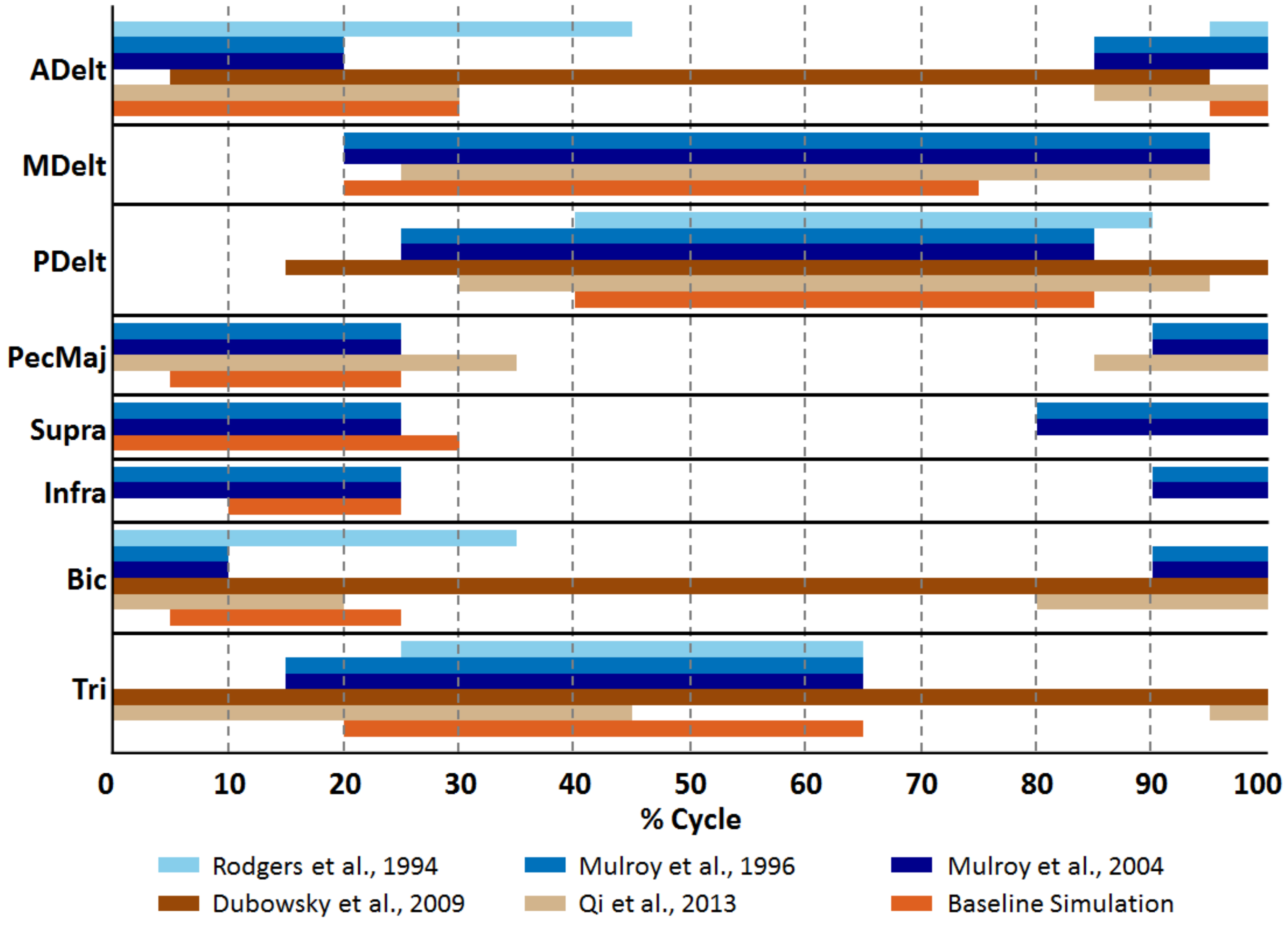

Figure A.13: Comparison between muscle excitation timing data from the baseline simulation and values found in the literature (Dubowsky et al., 2009; Mulroy et al., 2004; Mulroy et al., 1996; Qi et al., 2013; Rodgers et al., 1994).

Appendix B: Supplementary Material for Chapter 3

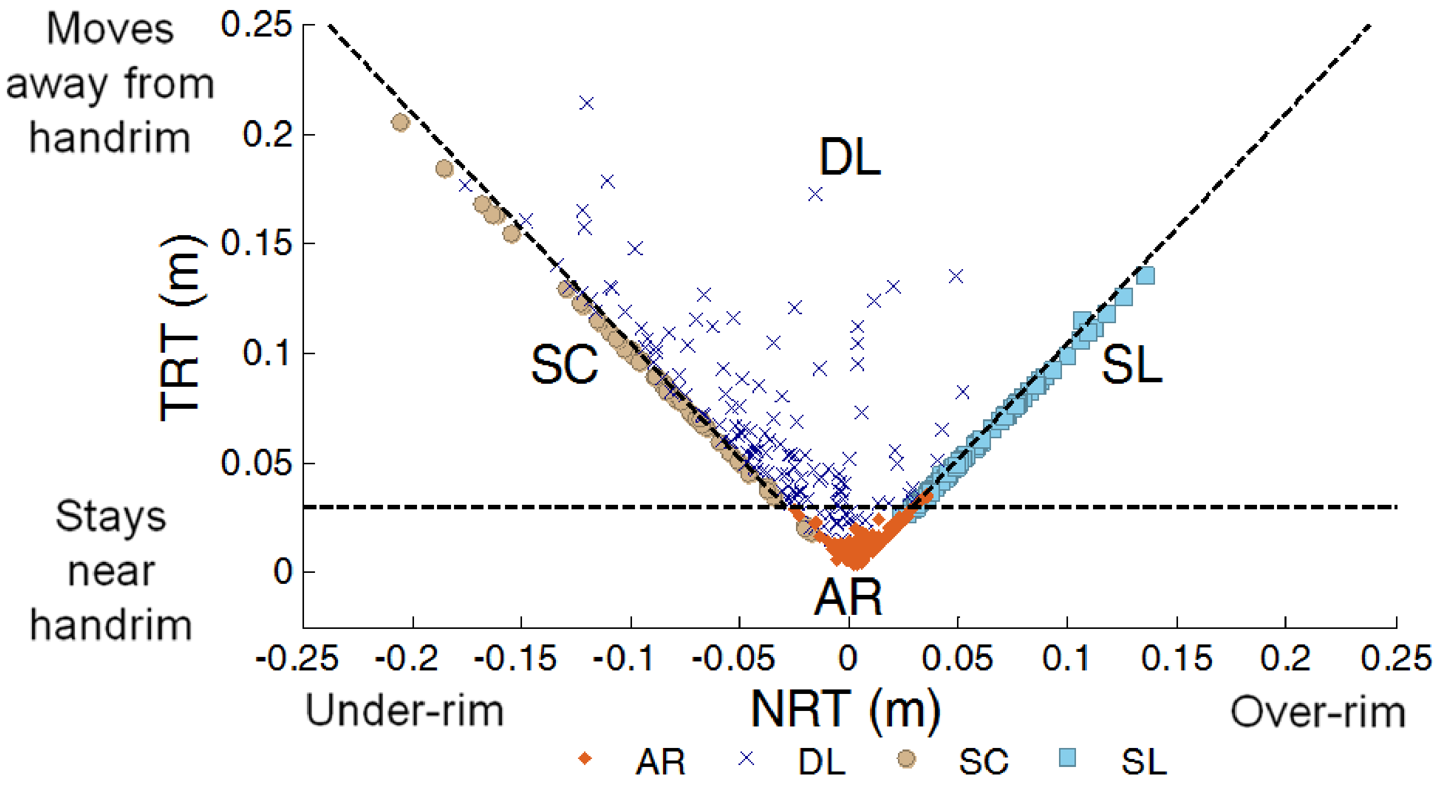

Figure B.1: Comparison of objective and subjective hand pattern classification results. The vertical axis corresponds to TRT and the horizontal axis corresponds to the ratio NRT. Thresholds for the objective classification are depicted with the dashed lines at TRT = 0.03m, NRT/TRT = -0.95 and NRT/TRT = 0.95. Regions corresponding to each pattern type are labeled with the objective classification. Subjective classification is indicated with the following symbols: AR (◆), DL (×), SC (●) and SL (■).

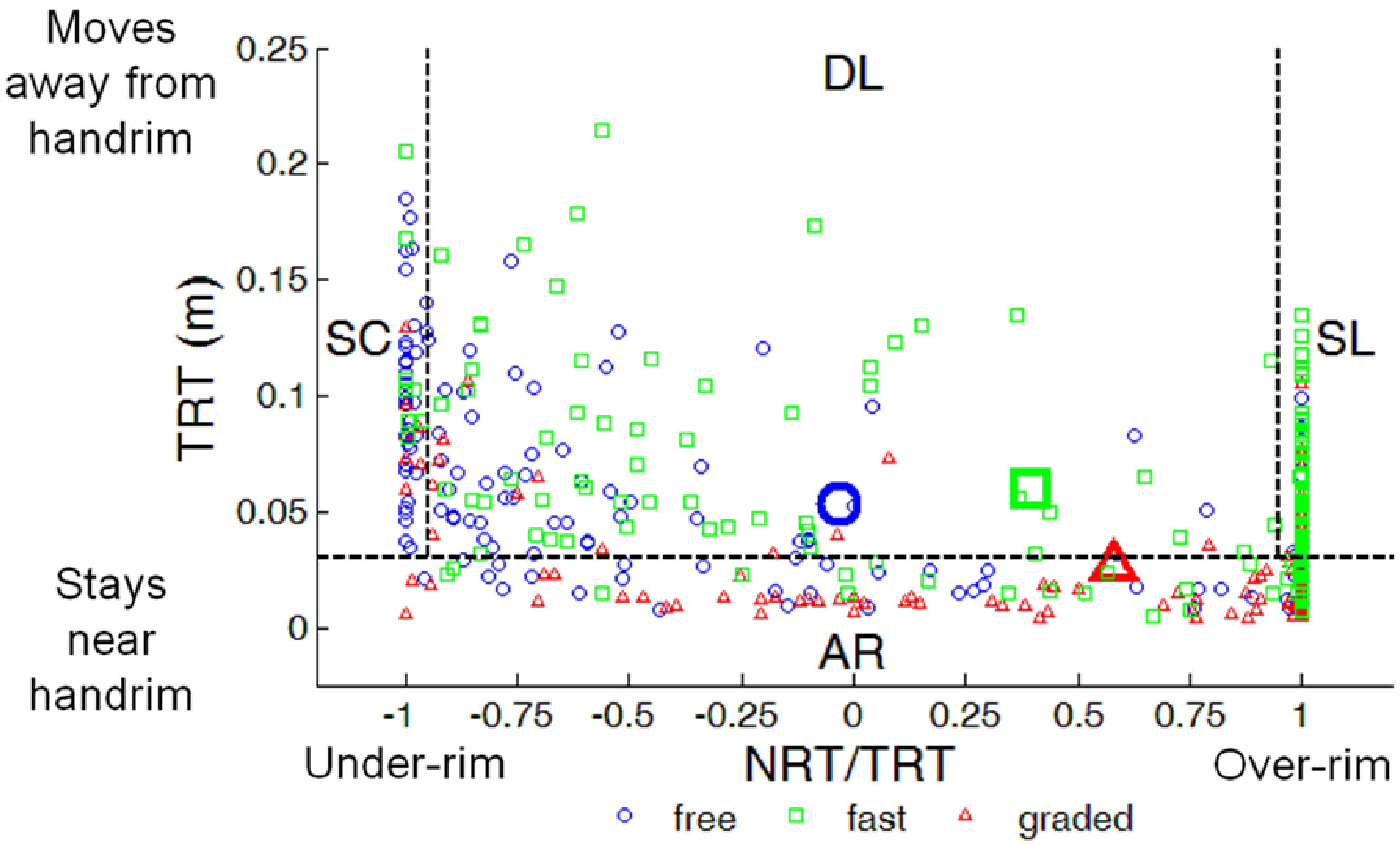

Figure B.2: Hand pattern parameter values across conditions. The vertical axis corresponds to TRT and the horizontal axis corresponds to NRT/NRT. Thresholds for the objective classification are depicted with the dashed lines at TRT = 0.03m, NRT/TRT = -0.95 and NRT/TRT = 0.95. Regions corresponding with each pattern type are labeled with the objective classification. Propulsion condition is indicated as follows: free (○), fast (□) and graded (△). The across-subject mean values are indicated with a larger version of the same symbol.

Appendix C: Supplementary Material for Chapter 4

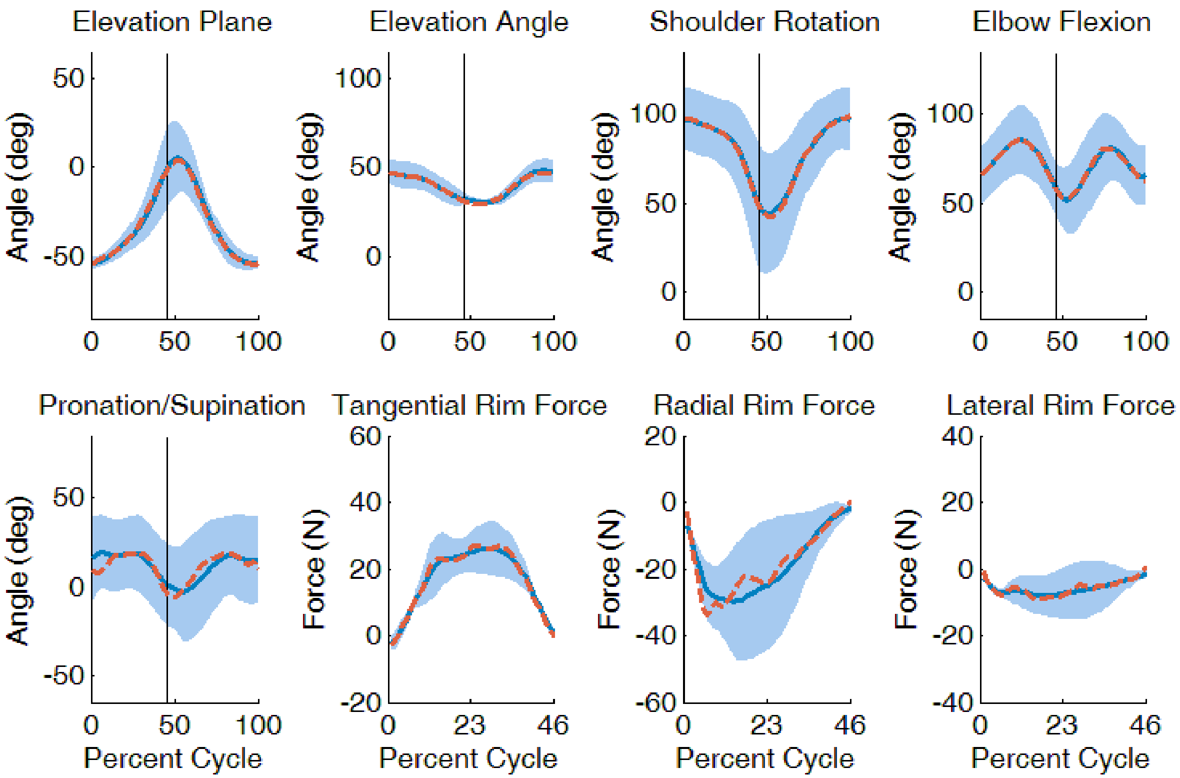

Figure C.1: Comparison between the simulation and group-averaged experimental mechanics for the arcing pattern (AR). Experimental and simulation values are represented by solid and dashed lines, respectively. Shaded regions represent ± 1 SD of the experimental data. The joint angle plots depict the full cycle, with the end of the contact phase indicated with a vertical line. The handrim force plots only depict the contact phase, as values are approximately zero throughout the recovery phase.

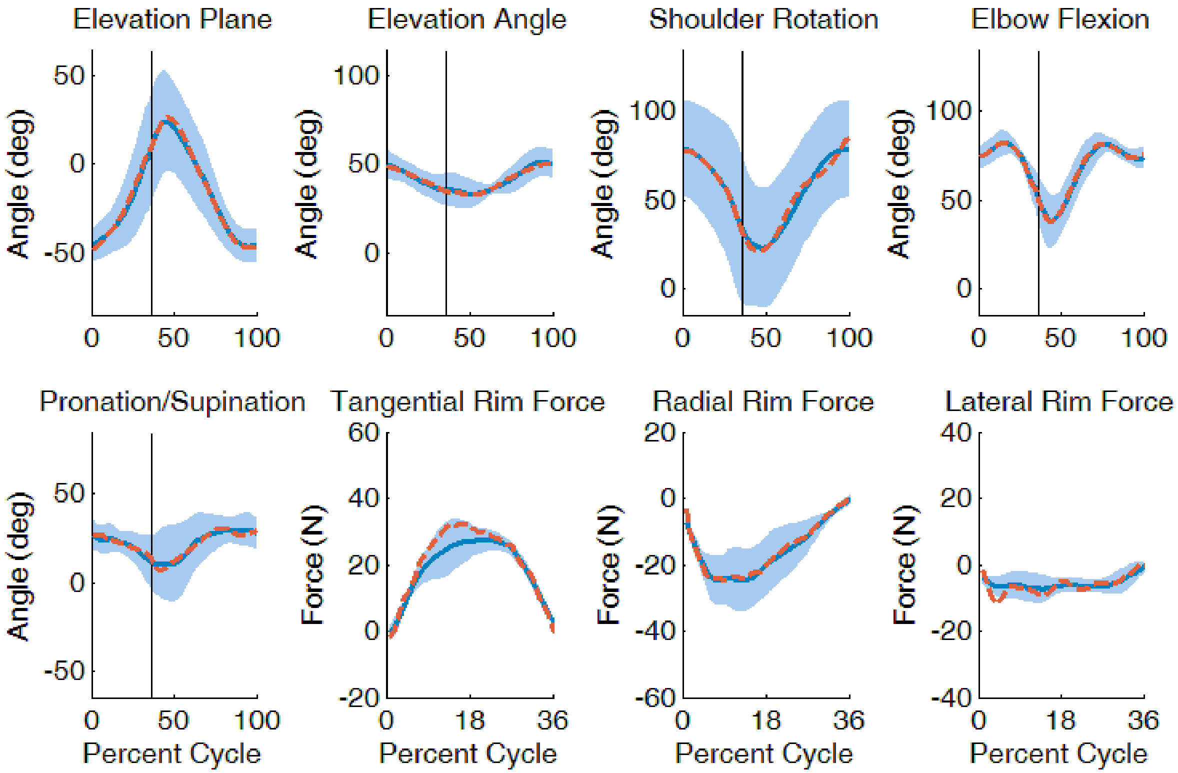

Figure C.2: Comparison between the simulation and group-averaged experimental mechanics for the single loop pattern (SL). Experimental and simulation values are represented by solid and dashed lines, respectively. Shaded regions represent ± 1 SD of the experimental data. The joint angle plots depict the full cycle, with the end of the contact phase indicated with a vertical line. The handrim force plots only depict the contact phase, as values are approximately zero throughout the recovery phase.

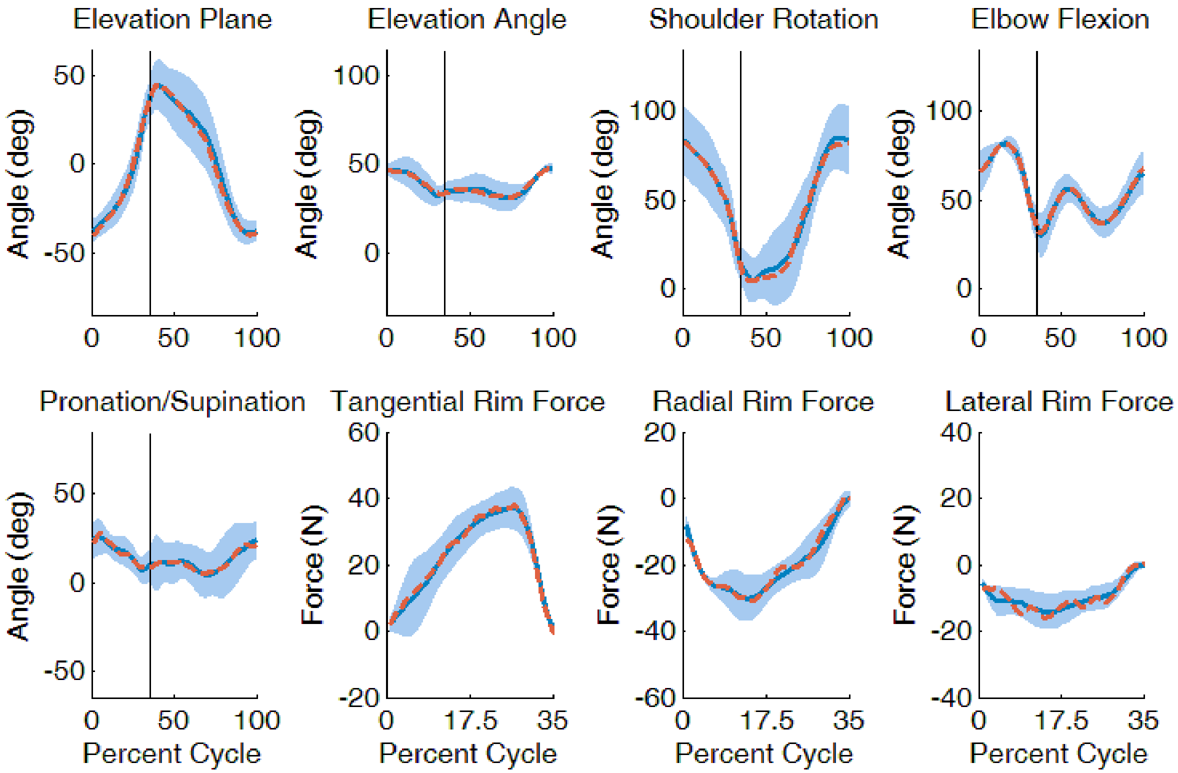

Figure C.3: Comparison between the simulation and group-averaged experimental mechanics for the double loop pattern (DL). Experimental and simulation values are represented by solid and dashed lines, respectively. Shaded regions represent ± 1 SD of the experimental data. The joint angle plots depict the full cycle, with the end of the contact phase indicated with a vertical line. The handrim force plots only depict the contact phase, as values are approximately zero throughout the recovery phase.

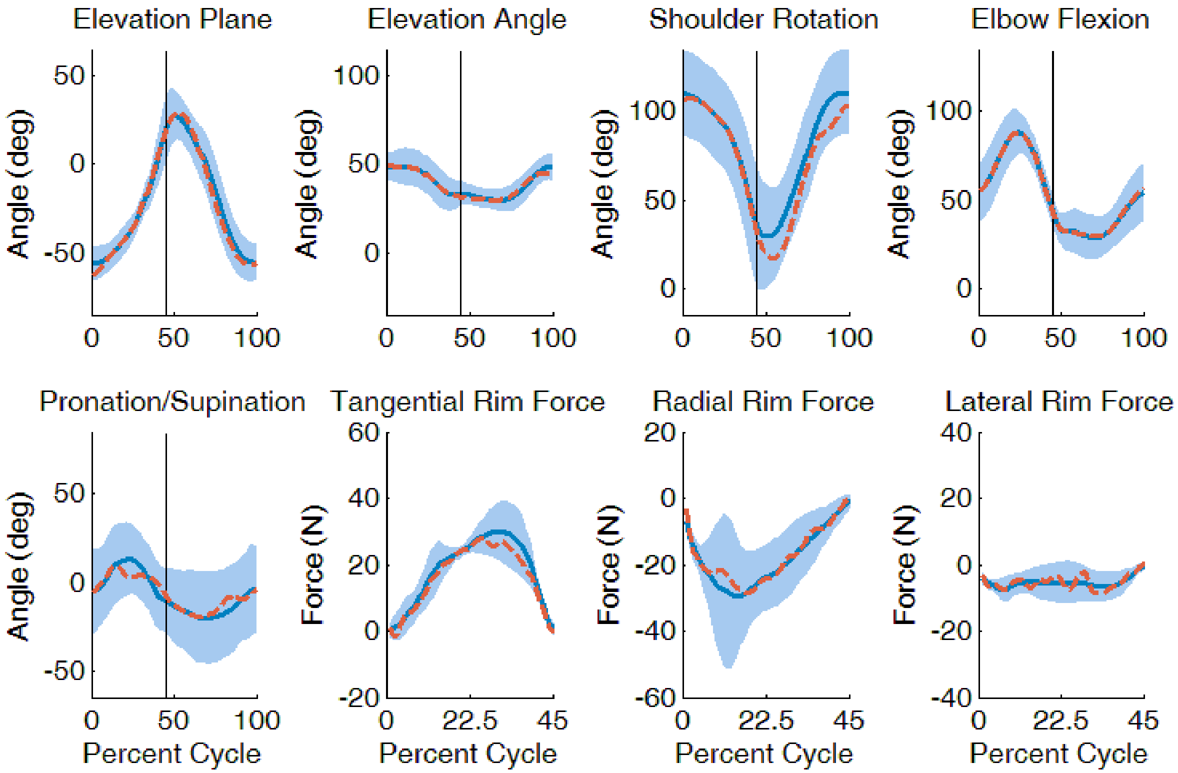

Figure C.4: Comparison between the simulation and group-averaged experimental mechanics for the semi-circular pattern (SC). Experimental and simulation values are represented by solid and dashed lines, respectively. Shaded regions represent ± 1 SD of the experimental data. The joint angle plots depict the full cycle, with the end of the contact phase indicated with a vertical line. The handrim force plots only depict the contact phase, as values are approximately zero throughout the recovery phase.

References

Aissaoui, R. and Desroches, G. (2008). Stroke pattern classification during manual wheelchair propulsion in the elderly using fuzzy clustering. *J. Biomech.* 41 (11), 2438-2445.

Boninger, M. L., Koontz, A. M., Sisto, S. A., Dyson-Hudson, T. A., Chang, M., Price, R., et al. (2005). Pushrim biomechanics and injury prevention in spinal cord injury: recommendations based on CULP-SCI investigations. *J. Rehabil. Res. Dev.* 42 (3 Suppl 1), 9-19.

Boninger, M. L., Souza, A. L., Cooper, R. A., Fitzgerald, S. G., Koontz, A. M. and Fay, B. T. (2002). Propulsion patterns and pushrim biomechanics in manual wheelchair propulsion. *Arch. Phys. Med. Rehabil.* 83 (5), 718-723.

Braden, B. (1986). The surveyor's area formula. *Coll. Math. J.* 17 (4), 326-337.

Brault, M. W. (2008). Americans with disabilities: 2005. Current Population Reports. US Department of Commerce, Economics and Statistics Administration, US Census Bureau.

Brault, M. W. (2012). Americans with disabilities: 2010. Current Population Reports. US Department of Commerce, Economics and Statistics Administration, US Census Bureau.

Burnham, R. S., May, L., Nelson, E., Steadward, R. and Reid, D. C. (1993). Shoulder pain in wheelchair athletes. The role of muscle imbalance. *Am. J. Sports Med.* 21 (2), 238-242.

Chow, J. W., Millikan, T. A., Carlton, L. G., Chae, W. S., Lim, Y. T. and Morse, M. I. (2009). Kinematic and electromyographic analysis of wheelchair propulsion on ramps of different slopes for young men with paraplegia. *Arch. Phys. Med. Rehabil.* 90 (2), 271-278.

Cooper, R. A., Cooper, R. and Boninger, M. L. (2008). Trends and issues in wheelchair technologies. *Assist. Technol.* 20 (2), 61-72.

Curtis, K. A., Drysdale, G. A., Lanza, R. D., Kolber, M., Vitolo, R. S. and West, R. (1999). Shoulder pain in wheelchair users with tetraplegia and paraplegia. *Arch. Phys. Med. Rehabil.* 80 (4), 453-457.

Davy, D. T. and Audu, M. L. (1987). A dynamic optimization technique for predicting muscle forces in the swing phase of gait. *J. Biomech.* 20 (2), 187-201.

de Groot, J. H. and Brand, R. (2001). A three-dimensional regression model of the shoulder rhythm. *Clin. Biomech.* 16 (9), 735-743.

de Groot, S., de Bruin, M., Noomen, S. P. and van der Woude, L. H. (2008). Mechanical efficiency and propulsion technique after 7 weeks of low-intensity wheelchair training. *Clin. Biomech.* 23 (4), 434-441.

de Groot, S., Veeger, H. E., Hollander, A. P. and van der Woude, L. H. (2004). Effect of wheelchair stroke pattern on mechanical efficiency. *Amer. J. Physical Med.* 83 (8), 640-649.

Dubowsky, S. R., Sisto, S. A. and Langrana, N. A. (2009). Comparison of kinematics, kinetics, and EMG throughout wheelchair propulsion in able-bodied and persons with paraplegia: an integrative approach. *Journal of Biomechanical Engineering* 131 (2), 021015.

Enoka, R. M. and Duchateau, J. (2008). Muscle fatigue: what, why and how it influences muscle function. *J. Physiol.* 586 (1), 11-23.

Erdemir, A., McLean, S., Herzog, W. and van den Bogert, A. J. (2007). Model-based estimation of muscle forces exerted during movements. *Clin. Biomech.* 22 (2), 131-154.

Escamilla, R. F., Yamashiro, K., Paulos, L. and Andrews, J. R. (2009). Shoulder muscle activity and function in common shoulder rehabilitation exercises. *Sports Med.* 39 (8), 663-685.

Finley, M. A. and Rodgers, M. M. (2004). Prevalence and identification of shoulder pathology in athletic and nonathletic wheelchair users with shoulder pain: A pilot study. *J. Rehabil. Res. Dev.* 41 (3B), 395-402.

Gagnon, D. H., Babineau, A. C., Champagne, A., Desroches, G. and Aissaoui, R. (2014). Pushrim biomechanical changes with progressive increases in slope during motorized treadmill manual wheelchair propulsion in individuals with spinal cord injury. *J. Rehabil. Res. Dev.* 51 (5), 789-802.

Gil-Agudo, A., Del Ama-Espinosa, A., Perez-Rizo, E., Perez-Nombela, S. and Crespo-Ruiz, B. (2010). Shoulder joint kinetics during wheelchair propulsion on a treadmill at two different speeds in spinal cord injury patients. *Spinal Cord* 48 (4), 290-296.

Goffe, W. L., Ferrier, G. D. and Rogers, J. (1994). Global Optimization of Statistical Functions With Simulated Annealing. *J. Econometrics* 60 (1), 65-99.

Goldberg, E. J. and Neptune, R. R. (2007). Compensatory strategies during normal walking in response to muscle weakness and increased hip joint stiffness. *Gait Posture* 25 (3), 360-367.

Gutierrez, D. D., Thompson, L., Kemp, B. and Mulroy, S. J. (2007). The relationship of shoulder pain intensity to quality of life, physical activity, and community participation in persons with paraplegia. *J. Spinal Cord Med.* 30 (3), 251-255.

Hakansson, N. A. and Hull, M. L. (2007). Influence of pedaling rate on muscle mechanical energy in low power recumbent pedaling using forward dynamic simulations. *IEEE T. Neur. Sys. Reh.* 15 (4), 509-516.

Hall, A. L., Peterson, C. L., Kautz, S. A. and Neptune, R. R. (2011). Relationships between muscle contributions to walking subtasks and functional walking status in persons with post-stroke hemiparesis. *Clin. Biomech.* 26 (5), 509-515.

Hamner, S. R., Seth, A. and Delp, S. L. (2010). Muscle contributions to propulsion and support during running. *J. Biomech.* 43 (14), 2709-2716.

Happee, R. and van der Helm, F. C. (1995). The control of shoulder muscles during goal directed movements, an inverse dynamic analysis. *J. Biomech.* 28 (10), 1179-1191.

Holzbaur, K. R., Murray, W. M. and Delp, S. L. (2005). A model of the upper extremity for simulating musculoskeletal surgery and analyzing neuromuscular control. *Ann. Biomed. Eng.* 33 (6), 829-840.

Jonkers, I., Stewart, C. and Spaepen, A. (2003). The complementary role of the plantarflexors, hamstrings and gluteus maximus in the control of stance limb stability during gait. *Gait Posture* 17 (3), 264-272.

Kaye, H. S., Kang, T. and LaPlante, M. (2000). Mobility Device Use in the United States. *Disability Statistics Report, (14)*. Washington, DC: U. S. Department of Education, National Institute on Disability and Rehabilitation Research.

Koontz, A. M., Cooper, R. A., Boninger, M. L., Souza, A. L. and Fay, B. T. (2002). Shoulder kinematics and kinetics during two speeds of wheelchair propulsion. *J. Rehabil. Res. Dev.* 39 (6), 635-649.

Koontz, A. M., Roche, B. M., Collinger, J. L., Cooper, R. A. and Boninger, M. L. (2009). Manual wheelchair propulsion patterns on natural surfaces during start-up propulsion. *Arch. Phys. Med. Rehabil.* 90 (11), 1916-1923.

Koontz, A. M., Worobey, L. A., Rice, I. M., Collinger, J. L. and Boninger, M. L. (2012). Comparison between overground and dynamometer manual wheelchair propulsion. *J. Appl. Biomech.* 28 (4), 412-419.

Koontz, A. M., Yang, Y. S., Boninger, T. D. S., Kanaly, J., Cooper, R. A., Boninger, M. L., et al. (2006). Investigation of the performance of an ergonomic handrim as a pain-relieving intervention for manual wheelchair users. *Assist. Technol.* 18 (2), 123-145.

Kulig, K., Newsam, C. J., Mulroy, S. J., Rao, S., Gronley, J. K., Bontrager, E. L., et al. (2001). The effect of level of spinal cord injury on shoulder joint kinetics during manual wheelchair propulsion. *Clin. Biomech.* 16 (9), 744-751.

Kulig, K., Rao, S. S., Mulroy, S. J., Newsam, C. J., Gronley, J. K., Bontrager, E. L., et al. (1998). Shoulder joint kinetics during the push phase of wheelchair propulsion. *Clin. Orthop. Relat. R.* 354 (1998), 132-143.

Kumar, S. (2001). Theories of musculoskeletal injury causation. *Ergonomics* 44 (1), 17-47.

Kwarciak, A. M., Sisto, S. A., Yarossi, M., Price, R., Komaroff, E. and Boninger, M. L. (2009). Redefining the Manual Wheelchair Stroke Cycle: Identification and Impact of Nonpropulsive Pushrim Contact. *Arch. Phys. Med. Rehabil.* 90 (1), 20-26.

Kwarciak, A. M., Turner, J. T., Guo, L. and Richter, W. M. (2012). The effects of four different stroke patterns on manual wheelchair propulsion and upper limb muscle strain. *Disabil. Rehabil. Assist. Technol.* 7 (6), 459-463.

Labriola, J. E., Lee, T. Q., Debski, R. E. and McMahon, P. J. (2005). Stability and instability of the glenohumeral joint: the role of shoulder muscles. *J. Shoulder Elbow Surg.* 14 (1 Suppl S), 32S-38S.

Lighthall-Haubert, L., Requejo, P. S., Mulroy, S. J., Newsam, C. J., Bontrager, E., Gronley, J. K., et al. (2009). Comparison of shoulder muscle electromyographic activity during standard manual wheelchair and push-rim activated power assisted wheelchair propulsion in persons with complete tetraplegia. *Arch. Phys. Med. Rehabil.* 90 (11), 1904-1915.

Lin, H. T., Su, F. C., Wu, H. W. and An, K. N. (2004). Muscle forces analysis in the shoulder mechanism during wheelchair propulsion. *P. I. Mech. Eng. H-J. Eng. Med.* 218 (H4), 213-221.

Liu, J., Hughes, R. E., Smutz, W. P., Niebur, G. and Nan-An, K. (1997). Roles of deltoid and rotator cuff muscles in shoulder elevation. *Clin. Biomech.* 12 (1), 32-38.

Liu, M. Q., Anderson, F. C., Pandy, M. G. and Delp, S. L. (2006). Muscles that support the body also modulate forward progression during walking. *J. Biomech.* 39 (14), 2623-2630.

McNeil, J. (2001). Americans with disabilities: 1997. Current Population Reports. US Department of Commerce, Economics and Statistics Administration, US Census Bureau.

Morrow, M. M., Van Straaten, M. G., Murthy, N. S., Braman, J. P., Zanella, E. and Zhao, K. D. (2014). Detailed shoulder MRI findings in manual wheelchair users with shoulder pain. *Biomed Research International* 2014 769649.

Mulroy, S. J., Farrokhi, S., Newsam, C. J. and Perry, J. (2004). Effects of spinal cord injury level on the activity of shoulder muscles during wheelchair propulsion: an electromyographic study. *Arch. Phys. Med. Rehabil.* 85 (6), 925-934.

Mulroy, S. J., Gronley, J. K., Newsam, C. J. and Perry, J. (1996). Electromyographic activity of shoulder muscles during wheelchair propulsion by paraplegic persons. *Arch. Phys. Med. Rehabil.* 77 (2), 187-193.

Neptune, R. R., Kautz, S. A. and Zajac, F. E. (2000). Muscle contributions to specific biomechanical functions do not change in forward versus backward pedaling. *J. Biomech.* 33 (2), 155-164.

Neptune, R. R., Kautz, S. A. and Zajac, F. E. (2001). Contributions of the individual ankle plantar flexors to support, forward progression and swing initiation during walking. *J. Biomech.* 34 (11), 1387-1398.

Newsam, C. J., Mulroy, S. and Perry, J. (2008). Use of power spectral analysis to document shoulder muscle fatigue during 15-minutes of continuous manual wheelchair propulsion. *J. Spinal Cord Med.* 31 (2), 231.

Newsam, C. J., Rao, S. S., Mulroy, S. J., Gronley, J. K., Bontrager, E. L. and Perry, J. (1999). Three dimensional upper extremity motion during manual wheelchair propulsion in men with different levels of spinal cord injury. *Gait Posture* 10 (3), 223-232.

Nho, S. J., Yadav, H., Shindle, M. K. and Macgillivray, J. D. (2008). Rotator cuff degeneration: etiology and pathogenesis. *Am. J. Sports Med.* 36 (5), 987-993.

Oh, J. H., Jun, B. J., McGarry, M. H. and Lee, T. Q. (2011). Does a critical rotator cuff tear stage exist?: a biomechanical study of rotator cuff tear progression in human cadaver shoulders. *J. Bone Joint Surg. Am.* 93 (22), 2100-2109.

Pandy, M. G. and Andriacchi, T. P. (2010). Muscle and joint function in human locomotion. *Annu. Rev. Biomed. Eng.* 12 401-433.

Paralyzed Veterans of America Consortium for Spinal Cord Medicine (2005). Preservation of upper limb function following spinal cord injury: a clinical practice guideline for health-care professionals. *J. Spinal Cord Med.* 28 (5), 434-470.

Qi, L., Wakeling, J., Grange, S. and Ferguson-Pell, M. (2012). Changes in surface electromyography signals and kinetics associated with progression of fatigue at two speeds during wheelchair propulsion. *J. Rehabil. Res. Dev.* 49 (1), 23-34.

Qi, L., Wakeling, J., Grange, S. and Ferguson-Pell, M. (2013). Coordination patterns of shoulder muscles during level-ground and incline wheelchair propulsion. *J Rehabil Res Dev* 50 (5), 651-62.

Qi, L., Wakeling, J., Grange, S. and Ferguson-Pell, M. (2014). Patterns of Shoulder Muscle Coordination Vary Between Wheelchair Propulsion Techniques. *IEEE T. Neur. Sys. Reh.* 22 (3), 559-566.

Raasch, C. C., Zajac, F. E., Ma, B. and Levine, W. S. (1997). Muscle coordination of maximum-speed pedaling. *J. Biomech.* 30 (6), 595-602.

Raina, S., McNitt-Gray, J., Mulroy, S. and Requejo, P. (2012). Effect of choice of recovery patterns on handrim kinetics in manual wheelchair users with paraplegia and tetraplegia. *J. Spinal Cord Med.* 35 (3), 148-155.

Rankin, J. W., Kwarciak, A. M., Mark Richter, W. and Neptune, R. R. (2010). The influence of altering push force effectiveness on upper extremity demand during wheelchair propulsion. *J. Biomech.* 43 (14), 2771-2779.

Rankin, J. W., Kwarciak, A. M., Richter, W. M. and Neptune, R. R. (2012). The influence of wheelchair propulsion technique on upper extremity muscle demand: A simulation study. *Clin. Biomech.* 27 (9), 879-886.

Rankin, J. W. and Neptune, R. R. (2012). Musculotendon lengths and moment arms for a three-dimensional upper-extremity model. *J. Biomech.* 45 (9), 1739-1744.

Rankin, J. W., Richter, W. M. and Neptune, R. R. (2011). Individual muscle contributions to push and recovery subtasks during wheelchair propulsion. *J. Biomech.* 44 (7), 1246-1252.

Rao, S. S., Bontrager, E. L., Gronley, J. K., Newsam, C. J. and Perry, J. (1996). Three-dimensional kinematics of wheelchair propulsion. *IEEE T. Rehab. Eng.* 4 (3), 152-160.

Requejo, P., Mulroy, S., Haubert, L. L., Newsam, C., Gronley, J. and Perry, J. (2008). Evidence-Based Strategies to Preserve Shoulder Function in Manual Wheelchair Users with Spinal Cord Injury. *Top. Spinal Cord Inj. Rehabil.* 13 (4), 86-119.

Rice, I., Impink, B., Niyonkuru, C. and Boninger, M. (2009). Manual wheelchair stroke characteristics during an extended period of propulsion. *Spinal Cord* 47 (5), 413-417.

Richter, W. M., Rodriguez, R., Woods, K. R. and Axelson, P. W. (2007). Stroke pattern and handrim biomechanics for level and uphill wheelchair propulsion at self-selected speeds. *Arch. Phys. Med. Rehabil.* 88 (1), 81-87.

Robertson, R. N., Boninger, M. L., Cooper, R. A. and Shimada, S. D. (1996). Pushrim forces and joint kinetics during wheelchair propulsion. *Arch. Phys. Med. Rehabil.* 77 (9), 856-864.

Rodgers, M. M., Gayle, G. W., Figoni, S. F., Kobayashi, M., Lieh, J. and Glaser, R. M. (1994). Biomechanics of wheelchair propulsion during fatigue. *Arch. Phys. Med. Rehabil.* 75 (1), 85-93.

Rodgers, M. M., McQuade, K. J., Rasch, E. K., Keyser, R. E. and Finley, M. A. (2003). Upper-limb fatigue-related joint power shifts in experienced wheelchair users and nonwheelchair users. *J. Rehabil. Res. Dev.* 40 (1), 27-37.

Sabick, M. B., Kotajarvi, B. R. and An, K. N. (2004). A new method to quantify demand on the upper extremity during manual wheelchair propulsion. *Arch. Phys. Med. Rehabil.* 85 (7), 1151-1159.

Sasaki, K. and Neptune, R. R. (2006). Differences in muscle function during walking and running at the same speed. *J. Biomech.* 39 (11), 2005-2013.

Seitz, A. L., McClure, P. W., Finucane, S., Boardman, N. D., 3rd and Michener, L. A. (2011). Mechanisms of rotator cuff tendinopathy: intrinsic, extrinsic, or both? *Clin. Biomech.* 26 (1), 1-12.

Sharkey, N. A. and Marder, R. A. (1995). The rotator cuff opposes superior translation of the humeral head. *Am. J. Sports Med.* 23 (3), 270-275.

Shimada, S. D., Robertson, R. N., Boninger, M. L. and Cooper, R. A. (1998). Kinematic characterization of wheelchair propulsion. *J. Rehabil. Res. Dev.* 35 (2), 210-218.

Silverstein, B., Fine, L. and Stetson, D. (1987). Hand-wrist disorders among investment casting plant workers. *J. Hand Surg. Am.* 12 (5 Pt 2), 838-844.

Slowik, J. S. and Neptune, R. R. (2013). A theoretical analysis of the influence of wheelchair seat position on upper extremity demand. *Clin. Biomech.* 28 (4), 378-385.

Steenbrink, F., de Groot, J. H., Veeger, H. E., van der Helm, F. C. and Rozing, P. M. (2009). Glenohumeral stability in simulated rotator cuff tears. *J. Biomech.* 42 (11), 1740-1745.

Steinmetz, E. (2006). Americans with disabilities: 2002. Current Population Reports. US Department of Commerce, Economics and Statistics Administration, US Census Bureau.

Stephens, C. L. and Engsberg, J. R. (2010). Comparison of overground and treadmill propulsion patterns of manual wheelchair users with tetraplegia. *Disabil. Rehabil. Assist. Technol.* 5 (6), 420-427.

Teyhen, D. S., Miller, J. M., Middag, T. R. and Kane, E. J. (2008). Rotator cuff fatigue and glenohumeral kinematics in participants without shoulder dysfunction. *J. Athl. Training* 43 (4), 352-358.

Thomas, C. K. and Zijdewind, I. (2006). Fatigue of muscles weakened by death of motoneurons. *Muscle Nerve* 33 (1), 21-41.

van der Helm, F. C. and Veeger, H. E. (1996). Quasi-static analysis of muscle forces in the shoulder mechanism during wheelchair propulsion. *J. Biomech.* 29 (1), 39-52.

van der Krogt, M. M., Delp, S. L. and Schwartz, M. H. (2012). How robust is human gait to muscle weakness? *Gait Posture* 36 (1), 113-119.

van der Woude, L. H., Hendrich, K. M., Veeger, H. E., van Ingen Schenau, G. J., Rozendal, R. H., de Groot, G., et al. (1988). Manual wheelchair propulsion:

effects of power output on physiology and technique. *Med. Sci. Sport. Exer.* 20 (1), 70-78.

van Drongelen, S., Schlussel, M., Arnet, U. and Veeger, D. (2013). The influence of simulated rotator cuff tears on the risk for impingement in handbike and handrim wheelchair propulsion. *Clin. Biomech.* 28 (5), 495-501.

van Drongelen, S., van der Woude, L. H., Janssen, T. W., Angenot, E. L., Chadwick, E. K. and Veeger, H. E. (2006). Glenohumeral joint loading in tetraplegia during weight relief lifting: a simulation study. *Clin. Biomech.* 21 (2), 128-137.

Veeger, H. E., Rozendaal, L. A. and van der Helm, F. C. (2002). Load on the shoulder in low intensity wheelchair propulsion. *Clin. Biomech.* 17 (3), 211-218.

Veeger, H. E., van der Woude, L. H. and Rozendal, R. H. (1991). Load on the upper extremity in manual wheelchair propulsion. *J. Electromyogr. Kines.* 1 (4), 270-280.

Vegter, R. J., Lamoth, C. J., de Groot, S., Veeger, D. H. and van der Woude, L. H. (2014). Inter-individual differences in the initial 80 minutes of motor learning of handrim wheelchair propulsion. *PLoS One* 9 (2), e89729.

Ward, S. R., Hentzen, E. R., Smallwood, L. H., Eastlack, R. K., Burns, K. A., Fithian, D. C., et al. (2006). Rotator cuff muscle architecture: implications for glenohumeral stability. *Clin. Orthop. Relat. R.* 448 157-163.

Winters, J. M. and Stark, L. (1988). Estimated mechanical properties of synergistic muscles involved in movements of a variety of human joints. *J. Biomech.* 21 (12), 1027-1041.

Zajac, F. E., Neptune, R. R. and Kautz, S. A. (2002). Biomechanics and muscle coordination of human walking. Part I: introduction to concepts, power transfer, dynamics and simulations. *Gait Posture* 16 (3), 215-232.

Vita

Jonathan Steven Slowik attended the Massachusetts Institute of Technology, where he received his Bachelor of Science in Mechanical Engineering in 2006. He subsequently joined Orbital Sciences Corporation and remained there until entering the Graduate School at The University of Texas at Austin in 2010, where he received his Master of Science in Engineering in 2012. The focus of his graduate research has been on the biomechanics of manual wheelchair propulsion with an emphasis on identifying the relationships between wheelchair configuration, propulsion technique, muscle weakness and upper extremity demand. The overarching goal of this research is to reduce the risk of upper extremity pain and injury in individuals who use manual wheelchairs.

Permanent email address: jsslowik@alum.mit.edu

This dissertation was typed by the author.